Water and Environmental Research Center
Annual Technical Report
FY 2017

Introduction

The University of Alaska Fairbanks (UAF) Water & Research Center (WERC) provides the State of Alaska with water resource solutions for the challenging Arctic and Subarctic regions. WERC, along with a team of civil and environmental engineers, hydrologists, limnologists, ecologists, chemists, social scientists, permafrost scientists, and an array of other faculty, staff and student researchers, strive to understand the changing environment to improve the quality of life for all Alaskan's, while protecting the bountiful natural resources in a fragile ecosystem. UAF is America's Arctic University and continues to be one of our nation's foremost centers of expertise in field-based, cold regions water research.

Research Program Introduction

The FY2017 104(b) grants continue to reflect the diverse nature of our current research. The 104(b) grants we received for the funding period were instrumental in allowing a group of WERC-affiliated students to pursue research projects important to the State of Alaska. FY17 topics included characterization of groundwater hydrology in two thermokarst lake systems, assessment of climate and land-use change impacts on surface water runoff and connectivity in a continuous permafrost watershed in the National Petroleum Reserve-Alaska, a laboratory investigation of the rheology of non-Newtonian fluids for effective remediation of persistent contaminants from porous media under non-isothermal flow regimes, and a study of variable lapse rates and mass balance of the Eklutna Glacier in south-central Alaska. Each topic examines an area of concern to the State of Alaska and is reflective of the broad nature of research WERC actively pursues. In addition, one 2016 project, which was continued into 2017, is included in this report.

Removal of Toxic Heavy Metals from Contaminated Water Using a Metal-Organic Framework (MOF)-Graphene Oxide (GO) Hybrid Material

Basic Information

Title:	Removal of Toxic Heavy Metals from Contaminated Water Using a Metal-Organic Framework (MOF)-Graphene Oxide (GO) Hybrid Material
Project Number:	2016AK132B
Start Date:	3/1/2017
End Date:	12/22/2017
Funding Source:	104B
Congressional District:	AK-001
Research Category:	Water Quality
Focus Categories:	Water Quality, Treatment, Toxic Substances
Descriptors:	None
Principal Investigators:	Lei Zhang

Publication

1. Tonoy Chowdhury, 2017. Removal of Toxic Heavy Metals from Contaminated Water Using a Metal-Organic Framework (MOF)-Graphene Oxide (GO) Hybrid Material Composite (Master thesis, University of Alaska Fairbanks). Three manuscripts are in preparation.

1. Project Title: Removal of Toxic Heavy Metals from Contaminated Water Using a Metal-Organic Framework (MOF)-Graphene Oxide (GO) Hybrid Material

2. Principal Investigator(s): Lei Zhang

3. Abstract

MIL-53(Al)-graphene oxide (GO) nanocomposites of different GO to MIL-53(Al) mass ratios were synthesized. The properties of MIL-53(Al)-GO nanocomposites were characterized using X-ray Diffraction (XRD), Fourier Transform Infrared Spectroscopy (FT-IR), Brunauer-Emmett-Teller (BET) surface area measurement and Scanning Electron Microscopy (SEM). Batch experiments were performed on MIL-53(Al)-GO nanocomposites for As(III), Ni(II) and Pb(II) adsorption from aqueous solution. MIL-53(Al)-GO nanocomposites showed higher adsorption of As(III) than pristine MIL-53(Al) and GO. Kinetic and thermodynamic studies were carried out to examine the adsorption mechanism.

4. Problem/Motivation and Research Objectives

Mining in Alaska affects many fresh water sources through heavy use of water in processing ore, and water pollution from discharged mine effluent and seepage from tailings and waste rock impoundments. Heavy metal pollution is caused when metals, such as arsenic, nickel, lead, cadmium, cobalt, copper, silver and zinc, contained in excavated rock or exposed in an underground mine come in contact with water. These heavy metals could be harmful to those who drink the water, as they are not biodegradable and can accumulate in living tissues, posing great threat to both human health and the ecological environment. While there have been improvements to mining practices in recent years, significant environmental risks remain that can affect the availability of clean drinking water resources in rural and remote Alaskan communities. Thus, it is imperative to develop efficient methods to remove heavy metals from contaminated waters.

Major objectives of the research are to:

(1) Synthesize MIL-53(Al)-GO and characterize its crystal structure and surface area.

(2) Test the efficacy of MIL-53(Al)-GO for the removal of As(III), Ni(II), and Pb(II) ions and explore the relationship of the adsorption capacity of heavy metal ions as a function of the mass ratio of MIL-53(Al) in MIL-53(Al)-GO.

(3) Develop adsorption isotherm models and measure the kinetics of heavy metal removal on MIL-53(Al)-GO.

5. Methodology

Methods and materials

Materials: Aluminum(III) nitrate nonahydrate ($Al(NO_3)_3 \cdot 9H_2O$), terephthalic acid (H_2BDC), and N,N-dimethylformamide (DMF) were used to prepare MIL-53(Al). Graphene oxide (GO) was synthesized using 99% sulfuric acid (H_2SO_4), graphite, potassium permanganate ($KMnO_4$) and 30% hydrogen peroxide (H_2O_2). Stock solutions of heavy metals were made using lead(II) nitrate ($Pb(NO_3)_2$), nickel(II) nitrate hexahydrate ($Ni(NO_3)_2 \cdot 6H_2O$), and arsenic ICP standard (10,000 ppm As in 5% HNO_3), respectively. Arsenic ICP standard was purchased from Ricca Chemical Company (Arlington, TX) and the other chemicals were purchased from Sigma-Aldrich (St. Louis, MO). Methanol used for washing MIL-53(Al) was purchased from VWR scientific (West

Chester, PA). All reagents and solvents were analytic grade and used as received. Deionized water (DI) was produced using a Thermo Scientific Barnstead NANOpure purifying system (18.2 MΩ). Micro porous (4-7 µm) filter papers were used to separate heavy metal solutions from the adsorbent prior to atomic spectroscopy analysis.

Synthesis of GO: Graphene oxide was prepared according to the Hummers method (1) using 0.5 g of graphite powder, 0.5 g of $NaNO_3$ and 23 ml of H_2SO_4 (99%). The reagents were mixed by stirring in a glass beaker placed in an ice bath for 4 h and kept below 20 ˚C to avoid overheating and explosion. $KMnO_4$ (3 g) was then slowly added to the mixture. The ice bath was then removed and the temperature of the mixture was increased to 35 ˚C under continuous stirring for 1 hour. DI water (100 ml) was slowly added to the mixture, the beaker was covered with aluminum foil to avoid the mixture boiling off, and the temperature was elevated to 95 ˚C. After 2 h of heating, the mixture was cooled to room temperature and 100 ml of DI water was added and stirred, followed by the addition of 10 ml of 30% H_2O_2 and about another 30 minutes of stirring. Finally the brownish product was washed three times with deionized water, centrifuged (8000 rpm, 10 minutes) and freeze dried for 48 hours to obtain GO powder.

Synthesis of MIL-53(Al)-GO nanocomposite with different MIL-53(Al) mass ratios: MIL-53(Al) was synthesized according to the method reported in reference (2) using 0.788 g of $Al(NO_3)_3{\cdot}9H_2O$ (2.1 mmol) and 0.518 g of H_2BDC (3.12 mmol) mixed in 30 ml of DMF. The mixture was put in a 100-ml stainless steel autoclave with a Teflon inset at 130 ˚C for 72 hours in an oven. The resulting white gel was separated by centrifugation (8000 rpm, 10 minutes), washed three times with 30 ml of methanol, centrifuged again in the same manner, and air dried overnight at 100 ˚C. The white product was immersed in methanol (30 ml) for 24 hours, and washed and centrifuged three times with methanol following the procedures described above. Finally, the sample was dried overnight under vacuum at 110 ˚C.

MIL-53(Al)-GO nanocomposite was then synthesized by dispersing a certain amount of GO powder in 30 ml of DMF solution, along with $Al(NO_3)_3{\cdot}9H_2O$ and H_2BDC. The solution was sonicated for 10 minutes to obtain a homogeneous suspension and then subjected to the same synthesis procedure followed for MIL-53(Al). Each MIL-53(Al)-GO composite was denoted as n% MIL-53(Al)-GO, with n being the weight percentage of GO used in the reaction mixture, compared to the total weight of the precursors of MIL-53(Al)-GO.

Characterization: The crystal structures of MIL-53(Al)-GO, bare MIL-53(Al), and GO were examined using a PANalytical X'Pert MRD X-ray diffractometer in the Advanced Instrumentation Laboratory (AIL) at the University of Alaska Fairbanks (UAF). A Scientific Nicolet 6700 Fourier Transform Infrared Spectrometer in the UAF Chemistry Department was used to characterize the functional groups in MIL-53(Al)-GO, bare MIL-53(Al), and GO, to determine if MIL-53(Al)-GO was synthesized successfully. A JEOL JXA-8530F Electron Microprobe at the AIL was used to examine the morphologies of MIL-53(Al)-GO, bare MIL-53(Al), and GO. The surface areas of MIL-53(Al)-GO, MIL-53(Al), and GO were measured by nitrogen adsorption at 77 K in the UAF Mechanical Engineering materials laboratory. Samples were degassed at 120 °C for 12 h before measurement. Surface areas were calculated using the BET model.

Adsorption experiments: Batch experiments of As(III), Ni(II), and Pb(II) adsorption were conducted by mixing known quantities of MIL-53(Al)-GO having different MIL-53(Al) loadings

(0.4 to 3 g/L) with As(III), Ni(II), and Pb(II) ion aqueous solutions ranging from 10 to 150 ppm (10 to 450 ppm for Pb) in polyethylene test tubes. Before adsorption, adsorbents were vacuumed to dry at 120 °C for 24 h. The mixtures of adsorbent suspension and metal ion solution were well oscillated at room temperature until achieving equilibrium. The solid phase was centrifuged to separate from the solution. Concentrations of As(III), Ni(II), or Pb(II) in the filtrate were determined using an atomic absorption spectroscopy in the Water and Environmental Research Center (WERC) at UAF.

Adsorption kinetics: Ion solutions consisting of 50 ppm of As(III) and Ni(II) and 150 ppm of Pb(II) were added to 0.4 g/L MIL-53(Al)-GO nanocomposite suspensions (3% MIL-53(Al)-GO was used for As(III) adsorption and 5% MIL-53(Al)-GO was used for Pb(II) and Ni(II) adsorption). Supernatant was collected at different time intervals and the adsorptive uptake was measured as a function of reaction time until reaching equilibrium. Pseudo-first-order and pseudo-second-order equations were used to explain the diffusion mechanism of heavy metal ions on MIL-53(Al)-GO. The pseudo-first-order equation is defined as:

$$\log(q_e - q_t) = \log q_e - \frac{tk_1}{2.303} \qquad (1)$$

where q_e and q_t are the amounts of heavy metal ions adsorbed (mg/g) at equilibrium and time t (min), respectively, and k_1 (min^{-1}) is the adsorption rate constant. Values of k_1 will be calculated from plots of $\log(q_e - q_t)$ *vs.* t for As(III), Ni(II), and Pb(II) adsorption on the sorbents tested. The pseudo-second-order equation is expressed as:

$$\frac{t}{q_t} = \frac{1}{k_2 q_e^2} + \frac{t}{q_e} \qquad (2)$$

where k_2 (g/mg min^{-1}) is the rate constant of the pseudo-second-order adsorption, and q_t is the amount of heavy metal ion adsorbed at time t (mg/g). Values of k_2 were calculated from plots of t/q_t *vs.* t for As(III), Ni(II), and Pb(II) adsorption on the sorbents tested. All experiments were conducted in triplicate.

6. Principal Findings and Significance

(1) *Synthesis and characterization of MIL-53(Al)-GO:*

X–ray diffraction (XRD) patterns of MIL-53(Al), GO and MIL-53(Al)-GO composites are shown in Figure 1. The characteristic peaks of MIL-53(Al) at 8.8˚, 15.25˚, 17.75˚ and 11˚ for GO confirmed their crystal structures, which were in agreement with the previous work (3, 4). MIL-53(Al)-GO composites showed diffraction patterns similar to pure MIL-53(Al). Interestingly, there was no diffraction peak for GO in the composite, as the low content of GO was shielded by the attached MIL-53(Al) particles (5). It was also observed that crystallinity was reduced when GO content in MIL-53(Al) increased, which is probably due to the MIL-53(Al) cage separation and completely separated GO sheets (6).

In Figure 2, the FT-IR spectra of GO, MIL-53(Al) and their composites are presented. The spectra of MIL-53(Al) and those of the composites looked rather similar. Characteristic peaks of GO were observed at 3417 cm^{-1} for O–H stretching, 1623 cm^{-1} for C=C stretching, 1722 and 1407 cm^{-1} for carboxyl group stretching and 1230 and 983 cm^{-1} for C–O stretching (4). All of the characteristic peaks were also observed in the spectra of MIL-53(Al) and its composites. Apart from this, MIL-53(Al) and MIL-53(Al)-GO composites showed other peaks associated

with the benzene ring in terephthalic acid ligand (C–H at 1095 cm^{-1}) and –OH stretching at around 3500 cm^{-1}.

BET surface areas of MIL-53(Al), GO and MIL-53(Al)-GO composites are listed in Table 1. Surface areas of composites increased as the ratio of GO increased. Additional porosity of the developed MIL-53(Al)-GO composites might be the reason for (a) separation of cages of MIL-53(Al) due to the intersection of GO layers and (b) attachment of epoxy and hydroxyl functional groups of GO layers with MIL-53(Al) (6). The highest surface area, which was recorded for 2% MIL-53(Al)-GO, is around 18% and 500% higher than pure MIL-53(Al) and GO, respectively. A reduction in surface area is observed when the weight percent of GO added is higher than 3%. A high content of GO was not suitable for composite formation due to limited capability of the GO sheets to attach with MIL-53(Al) in some orientations, which is why n MIL-53(Al)-GO composite with low GO content showed higher surface area.

SEM images of the materials are provided in Figure 3, and show the morphology of GO, MIL-53(Al) and MIL-53(Al)-GO composites.

(2) *Test the efficacy of MIL-53(Al)-GO for the removal of As(III), Ni(II), and Pb(II) ions and explore the relationship of the adsorption capacity of heavy metal ions as a function of the mass ratio of MIL-53(Al) in MIL-53(Al)-GO.*

The equilibrium adsorption capacities of GO, MIL-53(Al) and MIL-53(Al)-GO composites are shown in Table 2. It is clear that the adsorption of heavy metal ions tested increased as the GO content in the MIL-53(Al) increased, but only up to a certain level. As(III) ion adsorption was found to be the maximum in 3% MIL-53(Al)-GO composite, and was 58% and 766% higher than that in MIL-53(Al) and GO, respectively. In contrast, 5% MIL-53(Al)-GO composite exhibited maximum adsorption of Ni(II) and Pb(II) ions, which were 1308% and 61% higher than MIL-53(Al) and 108% and 45% higher than GO, respectively. Adsorption is primarily dependent on the porosity of an adsorbent. In our study, the maximum surface area was found for 2% MIL-53(Al)-GO composite, while the maximum heavy metal adsorption was obtained in 3% and 5% MIL-53(Al)-GO composites. Similar results have been reported in previous works on MOF-GO composites (6). We assume that the pore diameters of 3% and 5% MIL-53(Al)-GO composites were suitable (smaller than the molecular size of As(III), Ni(II) and Pb(II) ions) for heavy metal adsorption, though further research is required to establish our assumption.

(3) *Develop adsorption isotherm models and measure the kinetics of heavy metal removal on MIL-53(Al)-GO.*

Adsorption data were analyzed according to the Langmuir adsorption isotherm model, Equations (3), which assumes that adsorption takes place at specific homogeneous sites within the adsorbent.

$$\frac{C_e}{q_e} = \frac{C_e}{q_{max}} + \frac{1}{q_{max} K_L} \quad (3)$$

where C_e is the equilibrium concentration of heavy metal ions (mg/L), q_e and q_{max} are the equilibrium adsorption capacity and the maximum adsorption capacity (mg/g), respectively, and K_L is the Langmuir constant (L/mg). Langmuir isotherm parameters for As(III), Ni(II) and Pb(II) adsorption are listed in Table 3. The high values of R^2 indicate that the adsorption of all of the heavy metal ions fit well with the Langmuir model, and the adsorptions were directed by

monolayer adsorption on a homogenous surface. Langmuir isotherms for the As(III), Ni(II) and Pb(II) adsorption are shown in Figures 4a-c. The maximum adsorption capacities (q_{max}) of composites were much higher than that of the pure MIL-53(Al) and GO.

Very fast kinetics were observed for all of the heavy metal ions tested. The effect of time on As(III), Ni(II) and Pb(II) ions adsorption is presented in Figures 4d-f. The equilibrium adsorption times were 60, 30 and 180 minutes for As(III), Ni(II) and Pb(II) ions, respectively. The kinetics data were analyzed using pseudo first and second order models (Equations 1 and 2), and it was found that adsorption for all the heavy metal ions fit best with the pseudo second order model.

7. Products (i.e. publications, conference abstracts, patents etc.)

Tonoy Chowdhury, 2017. Removal of Toxic Heavy Metals from Contaminated Water Using a Metal-Organic Framework (MOF)-Graphene Oxide (GO) Hybrid Material Composite (Master's thesis, University of Alaska Fairbanks).

8. Student support

One M.Sc. student, Tonoy Chowdhury, was supported directly on this award.

9. Notable awards and achievements

Outreach activities included a Summer Water Camp in summer 2016 at the Fairbanks Children's Museum with about 12 children in attendance. The camp attendees were granted a wonderful opportunity to learn about water filtration through demonstration and a hands-on activity.

The research outcomes that resulted from this project were used as preliminary results in Dr. Lei Zhang's NSF CAREER proposal submitted in summer 2016.

10. Tables, figures and their captions

Table 1. BET surface area of GO, MIL-53(Al) and MIL-53(Al)-GO composites.

Adsorbent	BET Surface Area (m^2/g)
GO	213
MIL-53(Al)	1079
1% MIL-53(Al)-GO	1154
2% MIL-53(Al)-GO	1273
3% MIL-53(Al)-GO	1147
5% MIL-53(Al)-GO	1050
10% MIL-53(Al)-GO	817
15% MIL-53(Al)-GO	775
25% MIL-53(Al)-GO	365

Table 2. Adsorption of As(III), Ni(II), and Pb(II) ions with GO, MIL-53(Al) and MIL-53(Al)-GO composites (10 mg of adsorbent in 25 mL 100 ppm metal solution for 24 hours).

Adsorbent	q_e for As (mg/g)[a]	q_e for Ni(II) (mg/g)[a]	q_e for Pb(II) (mg/g)[a]
GO	5.98	14.18	141.48
MIL-53(Al)	32.65	2.10	127.61
1% MIL-53(Al)-GO	49.73	22.65	179.60
2% MIL-53(Al)-GO	51.43	24.38	183.60
3% MIL-53(Al)-GO	51.80	22.31	154.00
5% MIL-53(Al)-GO	44.45	29.58	205.40
10% MIL-53(Al)-GO	43.53	14.20	151.30
15% MIL-53(Al)-GO	32.45	27.58	133.10
25% MIL-53(Al)-GO	37.55	15.84	44.70

[a] q_e is the equilibrium adsorption capacity of heavy metal ions in the specimen.

Table 3. Langmuir isotherm parameters for As(III), Ni(II) and Pb(II) adsorption in GO, MIL-53(Al), and MIL-53(Al)-GO composites.

Heavy Metal	Temp (K)	Adsorbent	Langmuir Parameters		
			q_{max} (mg/g)	K_L (L/mg)	R^2
As(III)	296	GO	2.80	0.05	0.970
		MIL-53(Al)	53.19	0.06	0.981
		3% MIL-53(Al)-GO	64.97	0.24	0.999
Ni(II)	296	GO	2.86	0.09	0.929
		MIL-53(Al)	3.05	0.29	0.997
		5% MIL-53(Al)-GO	41.39	0.03	0.971
Pb(II)	296	GO	170.35	0.12	0.993
		MIL-53(Al)	154.79	0.10	0.998
		5% MIL-53(Al)-GO	221.72	0.43	0.996

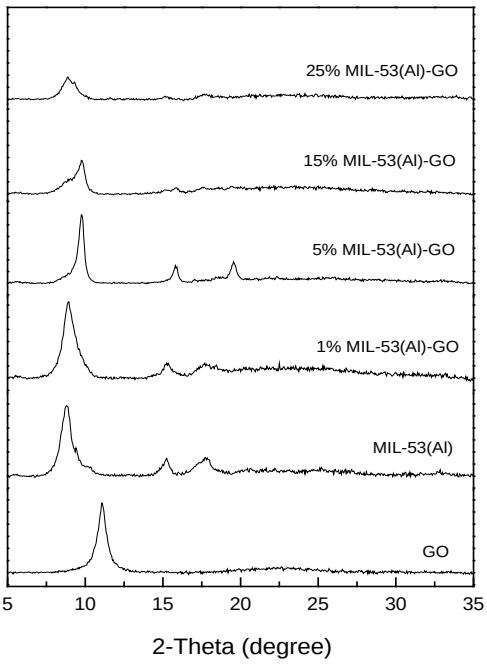

Figure 1. XRD patterns of MIL-53(Al), GO and MIL-53(Al)-GO composites.

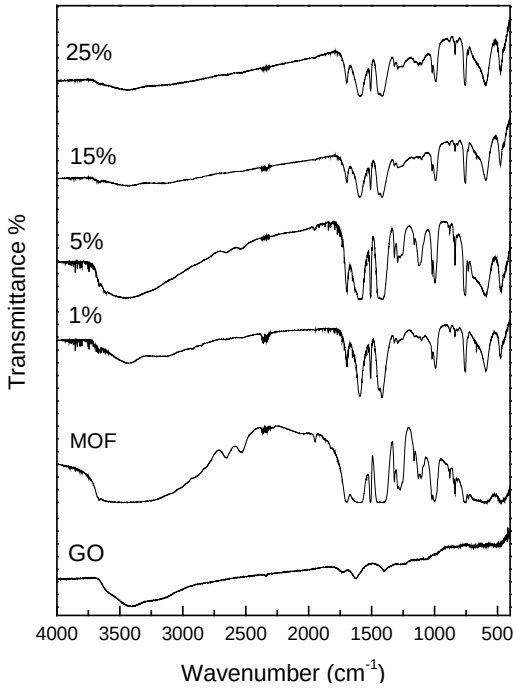

Figure 2. FTIR spectra of MIL-53(Al), GO and MIL-53(Al)-GO composites with different weight percentages of GO added (1 to 25%).

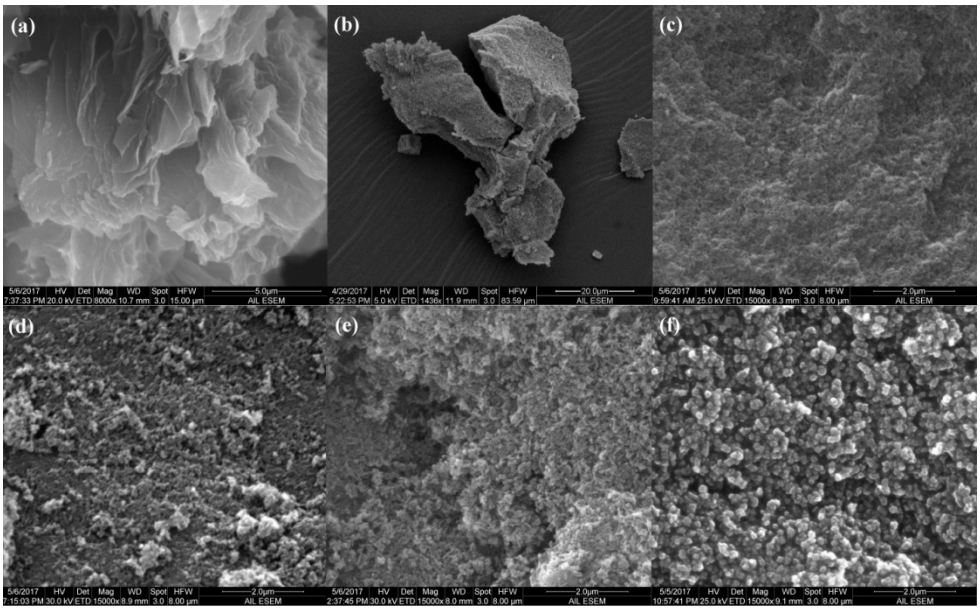

Figure 3. SEM images of (a) GO, (b) MIL-53(Al), (c) surface of MIL-53(Al), (d) 5% MIL-53(Al)-GO (e) 15% MIL-53(Al)-GO and (f) 25% MIL-53(Al)-GO.

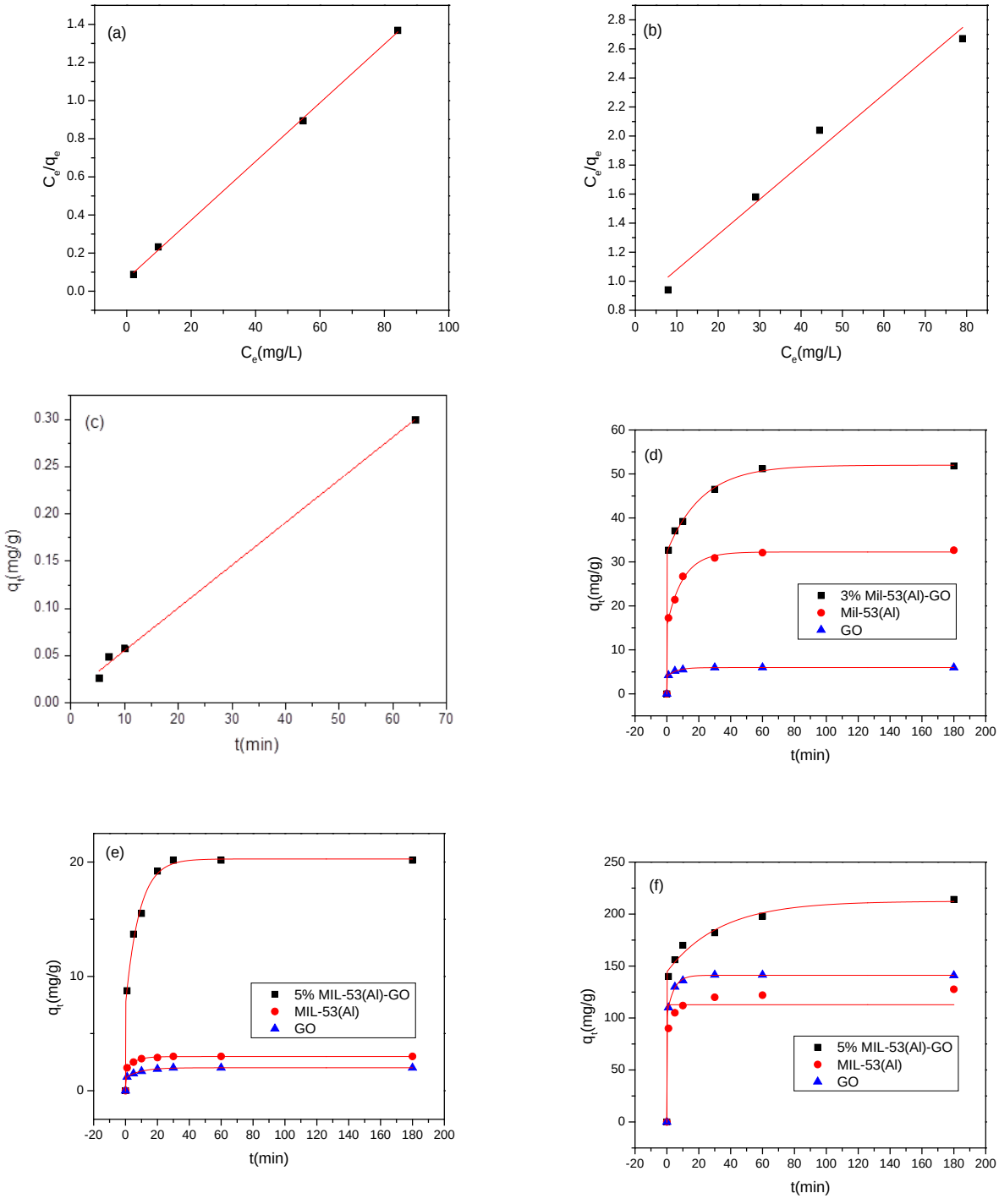

Figure 4. Langmuir isotherms of (a) As(III) adsorption in 3%MIL-53(Al)-GO, (b) Ni(II) adsorption in 5%MIL-53(Al)-GO, and (c) Pb(II) adsorption in 5%MIL-53(Al)-GO; the effect of time on (d) As(III), (e) Ni(II) and (f) Pb(II) ion adsorption in GO, MIL-53(Al), and MIL-53(Al)-GO composites.

References

1. Dey RS, Hajra S, Sahu RK, Raj CR, Panigrahi MK. A rapid room temperature chemical route for the synthesis of graphene: metal-mediated reduction of graphene oxide. Chem Commun. 2012;48(12):1787-9.
2. Ricco R, Konstas K, Styles MJ, Richardson JJ, Babarao R, Suzuki K, et al. Lead(ii) uptake by aluminium based magnetic framework composites (MFCs) in water. J Mater Chem A. 2015;3(39):19822-31.
3. Tien-Binh N, Vinh-Thang H, Chen XY, Rodrigue D, Kaliaguine S. Polymer functionalization to enhance interface quality of mixed matrix membranes for high CO2/CH4 gas separation. J Mater Chem A. 2015;3(29):15202-13.
4. Kyzas GZ, Deliyanni EA, Matis KA. Graphene oxide and its application as an adsorbent for wastewater treatment. Journal of Chemical Technology & Biotechnology. 2014;89(2):196-205.
5. Zhibin Wu XY, Hua Zhong, Hou Wang, Guangming Zeng, Xiaohong Chen, Hui Wang, Lei Zhang & Jianguang Shao. Enhanced adsorptive removal of p-nitrophenol from water by aluminum metal-organic framework/reduced graphene oxide composite. Sci Rep. 2016;6(25638).
6. Ahmed I, Jhung SH. Remarkable adsorptive removal of nitrogen-containing compounds from a model fuel by a graphene oxide/MIL-101 composite through a combined effect of improved porosity and hydrogen bonding. J Hazard Mater. 2016;314:318-25.

Characterization of Groundwater Hydrology in Two Thermokarst Lake Systems

Basic Information

Title:	Characterization of Groundwater Hydrology in Two Thermokarst Lake Systems
Project Number:	2017AK134B
Start Date:	3/1/2017
End Date:	2/28/2018
Funding Source:	104B
Congressional District:	AK-001
Research Category:	Ground-water Flow and Transport
Focus Categories:	Groundwater, Solute Transport, Hydrogeochemistry
Descriptors:	None
Principal Investigators:	David L. Barnes

Publications

1. Eckhardt, B.A., D.L. Barnes, R.P. Daanen, K.P. Walter Anthony, 2017, Transport of CH4 in Thermokarst Lakes in Discontinuous Permafrost. Poster presentation at Week of the Arctic 2017. 10 May 2017, Fairbanks, AK.
2. Eckhardt, B.A., D.L. Barnes, R.P. Daanen, K.P. Walter Anthony, 2016, Transport of CH4 in Open-Talik Lakes in Discontinuous Permafrost Aquifers. Poster presentation at American Geophysical Union Annual Fall Meeting. 15 December 2016, San Francisco, CA.

PROJECT TITLE: Characterization of Groundwater Hydrology in Two Thermokarst Lake Systems

PRINCIPAL INVESTIGATOR: David L. Barnes (graduate student: Bridget Eckhardt

ABSTRACT
Groundwater systems and flow dynamics in cold regions are dictated by the presence of permafrost and seasonal freeze-thaw dynamics. The complexity of groundwater flow in these systems increases in the discontinuous permafrost region where perennially thawed zones (open taliks) allow for connections between supra (above)- and sub (below)- permafrost groundwater which differ in quality and composition. This complexity poses difficulties in estimating groundwater quantity and quality and developing solutions for contaminant remediation. This study sought to characterize seasonal groundwater flow dynamics of supra- and sub-permafrost groundwater in two thermokarst lake systems in Interior Alaska. We utilized chemical and physical tracers to show distinct differences in the flow patterns in each lake and show the complexity of the flow dynamics in and around open taliks. This project provided a tested conceptual model for the flow of groundwater within thermokarst lakes which can be used as a baseline for future groundwater models.

MOTIVATION AND RESEARCH OBJECTIVES
Changing climate and the thawing of permafrost in the Arctic and sub-Arctic have the potential to impact water quality in both the supra- and sub- permafrost. This could have large impacts on drinking water facilities in rural Alaska and pose large health and infrastructural risks in highly underfunded communities.

Not only is understanding the quality of periglacial water resources important, but understanding flow dynamics is also imperative in understanding climate change in cold regions. In a previously funded NIWR project, we investigated how methane (CH_4), a potent greenhouse gas, could be transported to the atmosphere through vertical flow of groundwater in thermokarst lakes. The present project sought to further investigate the flow dynamics that could impact gas transport.

Objectives
- Collect and analyze geochemical data, including dissolved anion and cation concentrations as well as stable isotope signatures from the chosen thermokarst lakes and possible lake water sources.
- Collect and analyze physical tracer data, including hydrostatic pressure and temperature within the lakes' water columns and taliks.
- Determine possible contributions to the lakes and seasonal variations.
- Determine flow patterns around and within the lakes.

METHODOLOGY
During the spring of 2016, vibrating wire piezometers and Rhizon soil solution samplers (RSSS) were installed in both lakes below the sediment surface within the sub-lake taliks to monitor the direction of groundwater flow. Three (3) vibrating wire piezometers attached to a single metal pole were installed within the sub-lake taliks of each lake to gather both pressure and temperature data (Kane and Slaughter 1973). Five (5) RSSS were installed on a single metal pole

that was installed in two locations within the sub-lake taliks of each lake using methods adapted from Alberto et al. (2000). Four (4) TidBit temperature loggers were installed in the water column of each lake. Drive point wells outfitted with water level loggers were installed in the summer of 2016 in four (4) locations around each lake to monitor supra-permafrost groundwater flow and to obtain supra-permafrost groundwater samples.

Monthly sampling of surface lake water, benthic lake water, sub-lake talik porewater, supra-permafrost groundwater, and residential well groundwater provided water samples for analysis of stable water isotopes, deuterium and oxygen-18, dissolved anion and cation concentrations, and alkalinity. Stable isotopes, cations, and anions were used to help distinguish the primary sources of water in the lake (Barnes 2014; Hinkel et al. 2016; Mackay and Lavkulich 1974).

Finally, three (3) hammer cores were taken in each lake. These were used primarily to analyze dissolved methane concentrations and will not be discussed as part of this project.

PRINCIPAL FINDINGS AND SIGNIFICANCE

Results

Data collected from the vibrating wire piezometers indicate that there is downward flow through taliks in both lakes throughout the majority of the time period shown. This result may reflect the relatively high amount of precipitation this watershed received in the preceding winter (Winter 2015) and the summer of 2016. However, both lakes show unexpected patterns of alternating higher and lower pressures with depth. This may be indicative of soil layers with highly contrasting hydraulic conductivities. It may also indicate complex flow patterns, including the presence of and input from lateral taliks. A lateral talik in Doughnut Lake may be correlated with a connection to O'Connor Creek to the east of the lake (Figure 1). In Goldstream Lake (Figure 4), the piezometers primarily indicate downward flow, however, it is still very complex. This flow pattern may be correlated with a deep suprapermafrost talik at the thermokarst margin on the northeast side of the lake (possibly a result of thaw due to the presence of the road seen in Figure 4) and possibly an open talik beneath the lake. Extreme short-term variability in Goldstream Lake may also be the result of CH_4 bubble formation and release from the subsurface. These data highlight the complexity of groundwater flow in thermokarst lake systems.

Temperature is also an important indicator for flow direction. In the event of upward flow through a talik, higher temperatures from groundwater should be seen at depth while lower temperatures should be observed in more shallow parts of the talik. Review of the temperature data shows that this is not the case in either lake, indicating that there is either downward flow or no flow during the time period displayed. If the months of April and May 2016 had been included in temperature measurements, higher temperatures at depth may have been observed, indicating upward flow, however these data were not able to be captured and cannot be confirmed.

Stable isotope signatures of the various sources demonstrate distinct differences in composition. All data clusters around the local meteoric water line. A second line is evident and represents the local evaporation line. Doughnut Lake, as a result of its clearer water and warmer water temperatures during the summer, appears to experience larger amounts of evaporation. Goldstream Lake has a very depleted signature compared to Doughnut Lake. The depleted nature of the stable isotopes is likely a result of thawing permafrost contributions which are evident in

core samples as well as in-situ pore-water samples. Evidence of permafrost degradation and thermokarst on the northeast end of Goldstream Lake suggests there is likely a deep suprapermafrost talik here. The lake may receive deeper groundwater contributions through this conduit under the road and through the thermokarst margin, exacerbating thaw and collapse of the northeast shoreline.

Doughnut Lake tends to be very enriched in heavy water isotopes. This could be a result of two different processes: (1) evaporation and (2) microbial activity. While it seems very unlikely that microbial activity alone could have such a large effect on the lake's isotopic signature, we can see that the pore water beneath the lake is typically more enriched than the water column. The water column should theoretically be much more susceptible to evaporation than the pore water beneath the lake. This indicates that another process is causing the enrichment of the pore water.

When comparing the concentrations of sulfate in both lakes, we see large indications of upward flow of groundwater in Doughnut Lake during April. The large contrast between top and bottom water concentrations is evidence of possible upward flow through the talik. Goldstream Lake, however, maintains very low concentrations of sulfate, indicating a lack of groundwater input. This contradicts the stable isotope signature seen in this lake, which is typically closer to groundwater than Doughnut Lake. It is possible that the low concentration of sulfate may be explained by microbial consumption of the sulfate.

Figure 7 shows the chloride and deuterium data for the lake water column samples, active layer samples, and groundwater samples. This figure shows two points which occur in April and May 2016 where chloride and deuterium values trend towards groundwater in the top of Goldstream Lake. Doughnut Lake is observed in April and May of 2016 with a relatively high sulfate concentration. This trend, in conjunction with noticeably more depleted water isotope signatures, indicates that the lake received groundwater during this time of year. In particular, in Figure 7, Doughnut Lake bottom water trends towards groundwater signatures in chloride and deuterium. This contrasts with Goldstream Lake during the same period of time; while Goldstream Lake top water is influenced by groundwater, Doughnut Lake bottom water is influenced by groundwater.

Overall, each lake appears to have very different chemical compositions. Goldstream Lake tends to have high concentrations of chloride and cations such as magnesium and calcium. Doughnut Lake, on the other hand appears to have low concentrations of both chloride and cations. While by magnitude, Goldstream is rich in dissolved ions, when compared on a Piper diagram which displays the proportions of certain ions, the two lakes are not significantly different (Figure 8). A small difference between the two lakes can be seen as a result of the sulfate concentrations in the lower right trilinear diagram.

The geological and cryological structures around each lake greatly affect the flow dynamics within each lake. While Goldstream Lake is likely an open talik lake, the lack of observed contributions from groundwater to the bottom of the lake indicate that it has low hydraulic communication with the subpermafrost. This lack of flow direction is likely a result of its fine-grained sediment bottom (Hinkel et al. 2016; Wellman et al. 2013). In contrast, Doughnut Lake's coarse-grained lake bottom composition allows for connection and flow between the lake and the subpermafrost.

It is also very likely that elevation of the lakes with respect to the recharge zone has a large impact on the lake’s ability to act as a groundwater discharge exhibiting upward flow through the

lake talik. Bosson et al. (2010, 2013) noted that open talik lakes at a relatively higher elevation may exhibit downward flow while lakes at a relatively lower elevation may exhibit upward flow. Goldstream and Doughnut Lakes may exhibit this trend, where upward flow is more likely to occur in Doughnut Lake due to its lower elevation within the valley.

Overall, from our study, we have found that the flow patterns around open-talik lakes are extremely complex. More data will eventually be needed to confirm the trends that we have identified in our data. However, we have also shown the importance of approaching flow dynamics with a multi-faceted analysis. Each physical and chemical tracer aids in elucidating a different part of the story.

PRODUCTS

Eckhardt, B.A., Barnes, D.L., Barnes, M. L., Daanen, R.P. (2017). Application of Environmental Tracers in the Analysis of Flow in Discontinuous Permafrost Aquifers. Oral presentation at National Ground Water Association Summit. 4 December 2017, Nashville, TN.

Eckhardt, B.A., Barnes, D.L., Daanen, R.P., Walter Anthony, K.P. (2017). Transport of CH_4 in Thermokarst Lakes in Discontinuous Permafrost. Poster presentation at Week of the Arctic 2017. 10 May 2017, Fairbanks, AK.

Eckhardt, B.A., Barnes, D.L., Daanen, R.P., Walter Anthony, K.P. (2017). Transport of CH_4in Open-Talik Lakes in Discontinuous Permafrost Aquifers. Oral presentation at UAF Environmental Chemistry Symposium. 21 April 2017, Fairbanks, AK.

Eckhardt, B.A., Barnes, D.L., Daanen, R.P., Walter Anthony, K.P. (2017). Transport of CH_4 in Open-Talik Lakes in Discontinuous Permafrost Aquifers. Oral presentation at Alaska Fisheries Society/American Water Resources Association Annual Conference. 22 March 2017, Fairbanks, AK.

Eckhardt, B.A., Barnes, D.L., Daanen, R.P., Walter Anthony, K.P. (2017). Transport of $CH_4$from Subpermafrost Aquifers into Open-Talik Lakes in Goldstream Valley. Oral presentation at UAF Water and Environmental Research Center Seminar. 20 February 2017, Fairbanks, AK.

Eckhardt, B.A., Barnes, D.L., Daanen, R.P., Walter Anthony, K.P. (2016). Transport of CH_4 in Open-Talik Lakes in Discontinuous Permafrost Aquifers. Poster presentation at American Geophysical Union Annual Fall Meeting. 15 December 2016, San Francisco, CA.

Eckhardt, B.A., Barnes, D.L., Daanen, R.P., Walter Anthony, K.P. (2016). Contribution of Groundwater Flow through Open Taliks to Groundwater Resources. Oral presentation at UAF Air and Waste Management Association Chapter Meeting. 13 September 2016, Fairbanks, AK.

Eckhardt, B.A., Barnes, D.L., Daanen, R.P., Walter Anthony, K.P. (2016). Transport of CH_4 in Open-Talik Lakes in Discontinuous Permafrost Aquifers. Oral presentation at UAF Environmental Chemistry Symposium. 22 April 2016, Fairbanks, AK.

Eckhardt, B.A., Barnes, D.L., Daanen, R.P., Walter Anthony, K.P. (2016). Transport of CH_4 in Open-Talik Lakes in Discontinuous Permafrost Aquifers. Oral presentation at UAF Midnight Sun Science Symposium. 8 April 2016, Fairbanks, AK.

Eckhardt, B.A., Barnes, D.L., Daanen, R.P., Walter Anthony, K.P. (2016). Transport of CH_4 in Open-Talik Lakes in Discontinuous Permafrost Aquifers. Oral presentation at UAF Water and Environmental Research Center Seminar. 22 April 2016, Fairbanks, AK.

Liljedahl, A.K., Walter Anthony, K.M., Romanovsky, V.E., Barnes, D.L., Daanen, R.P., Gaedeke, A., Eckhardt, B.E. (2015). Methane release from thermokarst lakes: Thresholds and

feedbacks in the lake to watershed hydrology-permafrost system. Oral presentation at UAF Geosciences Seminar. 6 November 2015, Fairbanks, AK.

STUDENT SUPPORT

One M.Sc. student, Bridget Eckhardt, was supported directly on this award.

NOTABLE ACHIEVEMENTS/AWARDS

National Ground Water Association Summit. Farvolden Award, Outstanding Student Presentation. Nashville, TN. December 4, 2017.

UAF Environmental Chemistry Symposium. Outstanding Graduate Presentation. Fairbanks, AK. April 21, 2017.

USPA Student Travel Grant: Travel to American Geophysical Union Conference to present Transport of CH_4 in Open-Talik Lakes in Discontinuous Permafrost Aquifers, poster presentation. San Francisco, CA. December 12-16, 2016.

AWRA-AK Grad Student Scholarship Competition Award. Proposal for research of Transport of Methane in Open-Talik Lakes in Discontinuous Permafrost Aquifers. April 26, 2016.

FIGURES

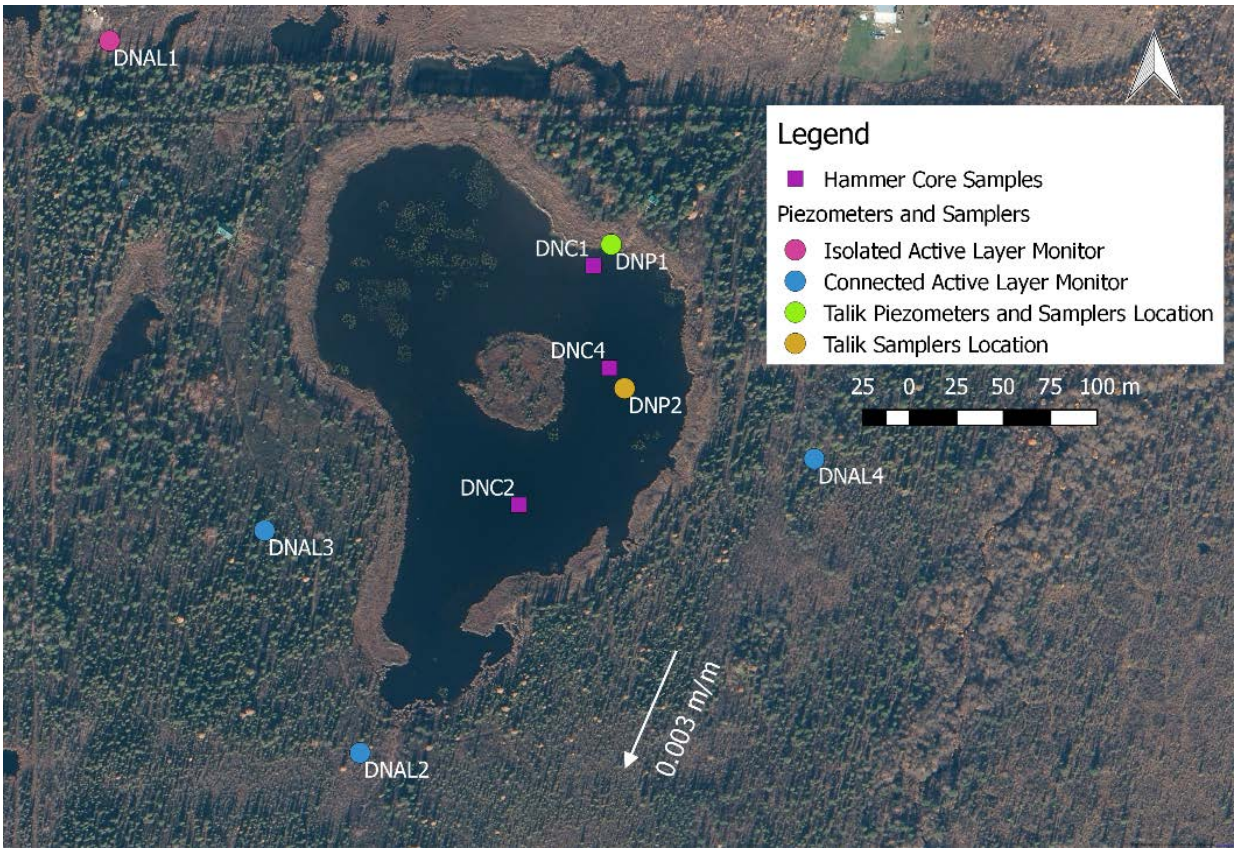

Figure 1. Doughnut Lake Sampling Sites

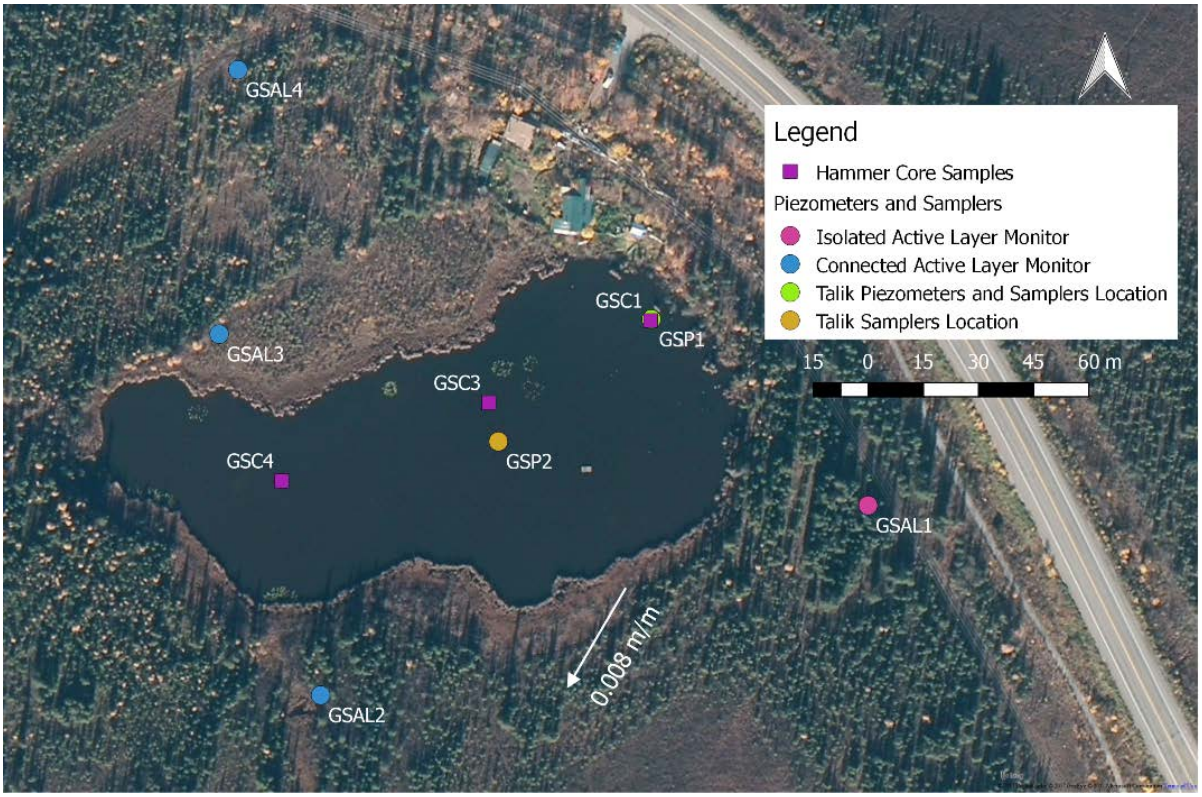

Figure 2. Goldstream Lake Sampling Sites

Figure 3. Hydrostatic pressure at depth within Doughnut Lake. Depths below sediment surface are as follows: DNP11 - 112.6 cm, DNP12 - 212.6 cm, DNP13 - 312.6 cm

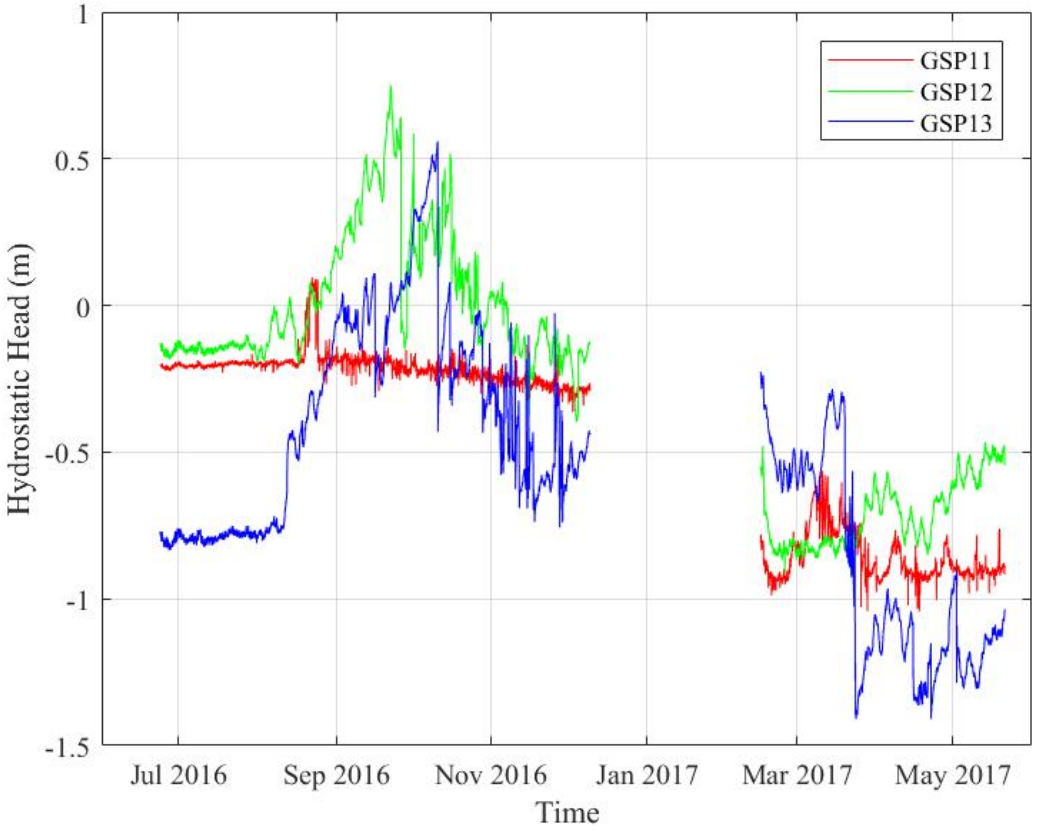

Figure 4. Hydrostatic pressure at depth within Goldstream Lake. Depths below sediment surface are as follows: GSP11 – 91.0 cm, GSP12 – 191.2 cm, GSP13 – 291.9 cm

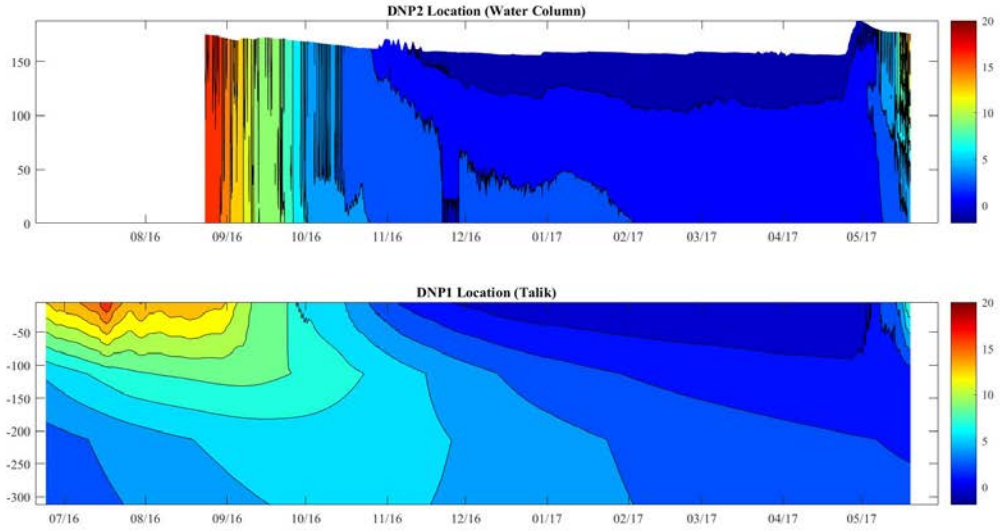

Figure 5. Doughnut Lake temperature contours in the water column (top) and talik (bottom).

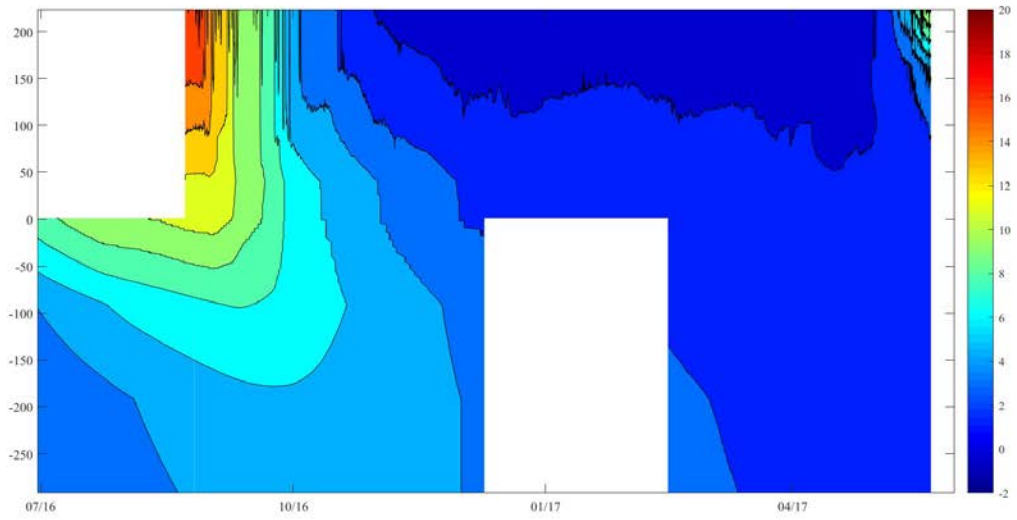

Figure 6. Goldstream Lake temperature contours in the water column and the talik. The sediment water interface is portrayed by a depth of 0 cm. All positive depths are in the water column, while all negative depths are in the talik.

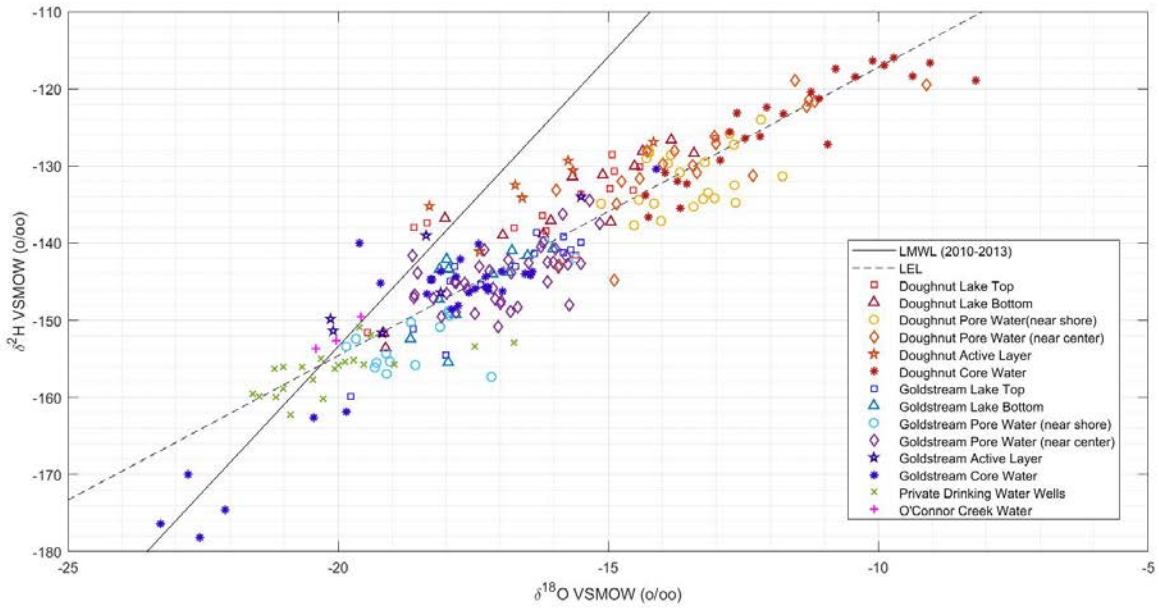

Figure 7. Stable water isotopes for all locations and dates of sampling

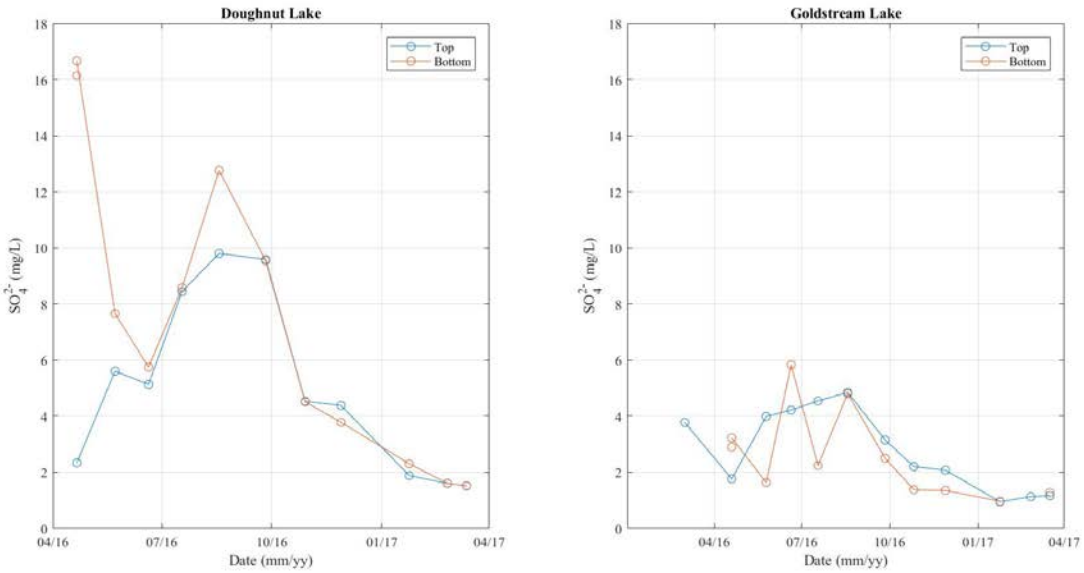

Figure 8. Sulfate Concentrations in Doughnut and Goldstream Lakes

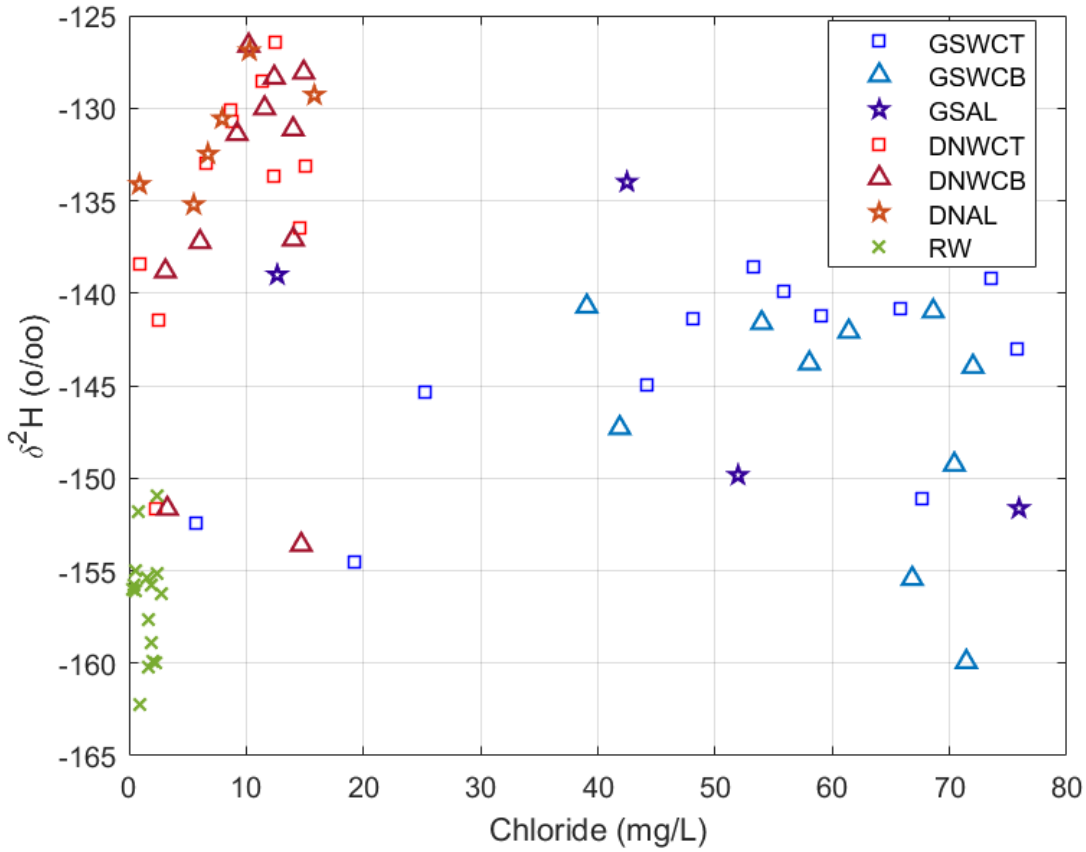

Figure 9. Deuterium and chloride correlations

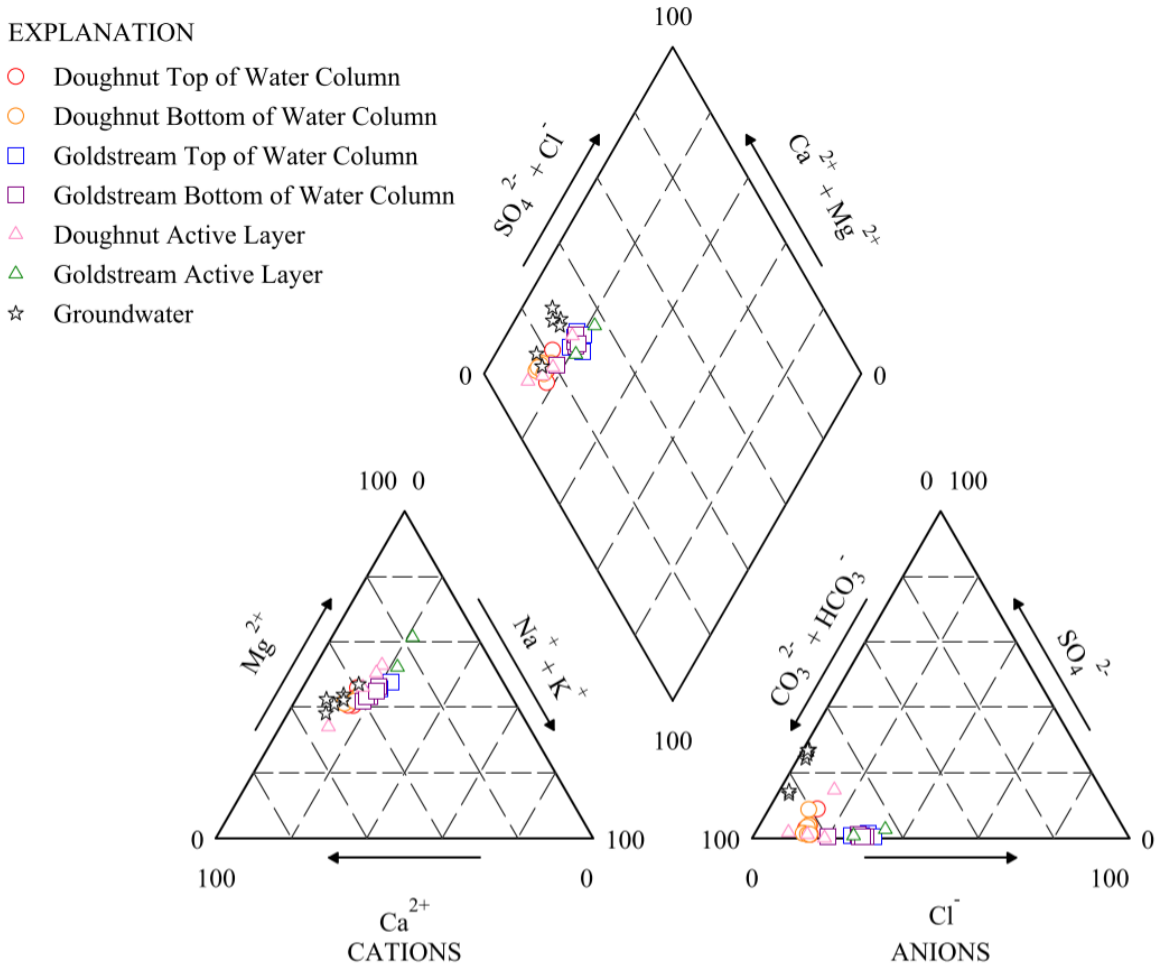

Figure 10. Piper Diagram displaying the relative proportions of dissolved ions

REFERENCES

Alberto, M. C. ., Arah, J. R. ., Neue, H. ., Wassmann, R., Lantin, R. ., Aduna, J. ., and Bronson, K. . (2000). “A sampling technique for the determination of dissolved methane in soil solution.” *Chemosphere - Global Change Science*, 2(1), 57–63.

Barnes, M. L. (2014). “Groundwater dynamics in degrading, discontinuous permafrost.” University of Alaska Fairbanks. M.S. Thesis.

Hinkel, K. M., Arp, C. D., Townsend-Small, A., and Frey, K. E. (2016). “Can Deep Groundwater Influx be Detected from the Geochemistry of Thermokarst Lakes in Arctic Alaska?” *Permafrost and Periglacial Processes*.

Kane, D. L., and Slaughter, C. W. (1973). “Recharge of a central Alaskan lake by subpermafrost groundwater.” *The North American Contribution to the Second International Conference on Permafrost, Yakutsk*, 458–462.

Klute, A. (1986). “Water Retention: Laboratory Methods.” *Methods of Soil Analysis, Part 1: Physical and Mineralogical Methods*, Madison.

Mackay, J. R., and Lavkulich, L. M. (1974). “Ionic and oxygen isotopic fractionation in permafrost growth.” *Geological Survey of Canada, Paper 74-1B*, 1, 255–266.

Assessment of climate and land-use change impacts on surface water runoff and connectivity in a continuous permafrost watershed in the National Petroleum Reserve - Alaska

Basic Information

Title:	Assessment of climate and land-use change impacts on surface water runoff and connectivity in a continuous permafrost watershed in the National Petroleum Reserve - Alaska
Project Number:	2017AK135B
Start Date:	3/1/2017
End Date:	2/28/2018
Funding Source:	104B
Congressional District:	AK-001
Research Category:	Climate and Hydrologic Processes
Focus Categories:	Hydrology, Models, Climatological Processes
Descriptors:	None
Principal Investigators:	Anne Gaedeke, Christopher Douglas Arp

Publications

1. Gädeke A., C. Arp, A. Liljedahl, R. Daanen, M. Whitman, L. Cai, V. Alexeev, B. Jones, M. Wipfli, J. Schulla, 2018, The impact of climate extremes and lake water-use on stream flows and connectivity in an Arctic Coastal Plain watershed in northern Alaska (in preparation, submission planned for late summer/fall 2018 to Water Resources Research).
2. Cai, L., V.A. Alexeev, C.D. Arp, B.M. Jones, A.K. Liljedahl, and A. Gädeke, 2018, The Polar WRF Downscaled Historical and Projected Twenty-First Century Climate for the Coast and Foothills of Arctic Alaska, Frontiers in Earth Science, 5(111), doi:10.3389/feart.2017.00111.
3. Jones, B.M., C.D. Arp, M.S. Whitman, D.A. Nigro, I. Nitze, J. Beaver, A. Gädeke, C. Zuck, A.K. Liljedahl, R.P. Daanen, E. Torvinen, S. Fritz, and G. Grosse, 2017, A lake-centric geospatial database to guide research and inform management decisions in an Arctic watershed in northern Alaska experiencing climate and land-use changes, Ambio, doi:10.1007/s13280-017-0915-9.

Title: Assessment of climate and land-use change impacts on surface water runoff and connectivity in a continuous permafrost watershed in the National Petroleum Reserve – Alaska

Principal Investigators:
Anne Gaedeke, Postdoctoral Fellow, University of Alaska Fairbanks, agaedeke@alaska.edu
Christopher Arp, Research Associate Professor, University of Alaska Fairbanks

Abstract
Permafrost, abundant surface-water storage, and extreme seasonality define watershed processes of Alaska's Arctic Coastal Plain (ACP), which are increasingly subject to changes both in climate and land use. To predict the responses to these changing conditions, we apply the process-based, spatially distributed hydrological and thermal model WaSiM to a 30 km^2 ACP watershed. Water balance simulations were used to evaluate the impact of climate extremes and lake water extraction based on the annual minimum 7-day mean flow (AMQ7), fish passage disconnectivity duration (DCD) and recovery time after disturbance. Scenarios of precipitation extremes, based on historic data, and winter lake water extraction, based on maximum permitted levels, were simulated over a 10-year period. Single and 3-year drought conditions caused a 56 and 69% reduction, respectively, in AMQ7 relative to the control with each taking 2 years to recover and up to 60 days of DCD (July-August). AMQ7 reductions of 44, 53, and 58% were caused by winter lake water extraction for one, two, and three consecutive years, respectively, with 2 to 3 years for recovery and DCD of 15 days (late July-beginning August). The maximum hydrologic impact of 91% AMQ7 reduction, 64 days of DCD (end of June-August), and 4 years of recovery was caused by a combination of 3 years of drought and lake water extraction. While our results show that ACP watersheds are immediately responsive to climate and water extraction, these systems appear resilient to long-term changes in processes impacting habitat connectivity. Our application of a hydrological model to analyze real-world change scenarios may serve as an important process-benchmark for other ACP watersheds in the future.

Problem/Motivation and Research Objectives
Watersheds on the Arctic Coastal Plain (ACP) are constrained near or at the surface due to the presence of deep (100's of m) permafrost (frozen ground material for more than two consecutive years) and a shallow (< 1 m) active layer (the seasonally thawed surface layer above permafrost) [*Woo*, 1986]. During short Arctic summers, expansive complex and intermittently connected surface drainage networks, mosaics of lakes, ponds, and wetlands set in the polygonized tundra characterize the landscape. The connectivity among these water bodies controls freshwater habitat availability and movement of locally migrating fish [*Heim et al.*, 2016; *Laske et al.*, 2016], and is governed by seasonal patterns of snowmelt and the balance between summer rainfall and evapotranspiration [*Bowling et al.*, 2003; *Lesack and Marsh*, 2010]. During snowmelt, surface water connectivity among lakes, ponds and wetlands is maximized, which allows fish to move into different habitats. Surface water runoff gradually declines through the summer, leading to a general drying and fragmentation of drainage networks within the watershed [*Bowling et al.*, 2003]. Lowest flows typically occur in early fall (September to October) before freeze-up when fish migrate to their overwintering habitats. Recent studies suggest, however, that this hydrologic regime can vary greatly from year to year [*Arp et al.*, 2012a; *Stuefer et al.*, 2017b], which can

impact connectivity [*Betts and Kane*, 2015; *Lesack and Marsh*, 2010] and alter patterns of migration [*Heim et al.*, 2016].

The ACP is currently experiencing high rates of environmental change which are expected to modify watershed processes from local to regional scales. The Arctic has experienced amplified climate warming since the 1970s [*Serreze and Francis*, 2006], which directly and indirectly affects hydrologic systems. Degrading permafrost [*Jorgenson et al.*, 2006; *Lantz and Kokelj*, 2008], deepening of the active layer [*Oelke et al.*, 2004], and thermokarst erosion [*Jones et al.*, 2011] can alter hydrologic storage and flowpaths, resulting in new runoff regimes [*Lawrence and Slater*, 2005; *Liljedahl et al.*, 2016]. Climate warming has also been associated with increasing rates and variability of precipitation, evapotranspiration, and runoff [*Déry et al.*, 2009; *Stuefer et al.*, 2017a], often referred to as hydrological intensification [*Rawlins et al.*, 2010]. Changes in lake ice thickness and ice-out timing has also been linked to altered rates of evaporation [*Arp et al.*, 2015a], which can impact late summer low flows in lake-dominated watersheds [*Arp et al.*, 2012b; *Bowling et al.*, 2003]. Perhaps the most pronounced hydrologic event in recent history on Alaska's North Slope was the 2007 drought, which contributed to a large tundra fire [*Jones et al.*, 2015] and extreme low flow conditions in ACP rivers [*Arp et al.*, 2012a; *Stuefer et al.*, 2017b].

Arctic land use changes are primarily associated with natural resource and infrastructure development, specifically oil and gas exploration. Industrial and infrastructural development, e.g. road construction for transportation and access to industrial sites, requires a reliable well-distributed water source whose availability is often limited during winter months and periods of drought [*Instanes et al.*, 2016]. Water from deeper lakes, which can provide overwintering habitat for fish if they do not freeze to the bed (floating ice lakes), are often the only locally available water source for ice-road construction. Currently, management of lake water use is based primarily on consideration of overwintering habitat, where it is assumed that lakes fully recharge during snowmelt runoff. The impact lake water extraction has on downstream flows in the following summer is only recently being considered, despite understanding that lakes provide the primary source of late summer flows in ACP streams [*Arp et al.*, 2015a; *Arp et al.*, 2012b].

Understanding how hydrologic systems are responding to climate and land use change, which are occurring simultaneously and rapidly in many regions of the Arctic, is of increasing relevance to developing comprehensive adaptive management plans to guide conservation, subsistence, and industry needs. The development of suitable adaptive management strategies, however, is challenging, as there is still much uncertainty in the climate projections [*Hodson et al.*, 2013] and as to how the systems will respond to future changes in climate and land use at a local and watershed scale.

Increasing data availability and computational capabilities have led to the development of fully spatially distributed physically-based hydrological models that include cold region processes and represent land surface characteristics explicitly. Applying a process-based hydrological model to an Arctic watershed experiencing major land-use changes provides a perfect test case to see if the hydrologic responses can be accurately predicted at the watershed scale. Here, we applied the Water Balance simulation model (WaSiM) to a watershed underlain by continuous permafrost on the Arctic Coastal Plain (ACP) of northern Alaska to address how climate and land use induced changes affect surface water storage, runoff and connectivity, and habitat access.

More specifically, we completed the following tasks:

a) set up, calibrate and validate WaSiM based on field measurements for a mesoscale low-gradient Arctic tundra watershed
b) set up of climate change scenarios that represent extreme climatic conditions experienced in the past and a real-world land use change scenario in the form of sustained winter lake water extration
c) force WaSiM with the climate change and winter lake water extraction scenarios and evaluate results

Through this study we gained a deeper understanding of how climate extremes (i.e., drier and wetter than normal summers) and lake water use impact hydrologic responses (surface water storage, runoff, and aquatic habitat connectivity), both in terms of magnitude and recovery time (to return to pre-disturbance conditions) following extreme years. Our modeling results can offer opportunities to support land managers with project design in future development projects and to guide the development of comprehensive adaptive management plans considering conservation, subsistence, and industry needs.

Methodology

Study Area

Our study focused on the Crea Creek Watershed (30 km^2), a sub-watershed of the Fish Creek drainage system (4600 km^2) located approximately halfway between Prudhoe Bay and Utqiagvik (formerly Barrow) on the ACP of northern Alaska. Both Crea Creek and the entire Fish Creek watershed are located in the northeast portion of the National Petroleum Reserve – Alaska (NPR-A). Crea Creek flows into the Ublutuoch River and is representative of many low-gradient beaded stream systems fed by thermokarst lakes on the ACP. Lakes cover approximately 16% of Crea Creek watershed's land surface [*Jones et al.*, 2017], many deep enough to support overwintering habitat in most years (i.e. floating ice above liquid water), while the rest freeze solid by the end of winter. The watershed is underlain by continuous permafrost, reaching depths of 270 m according to local borehole data [*Clow*, 2014]. Taliks (unfrozen soils within permafrost) occur under lakes and river courses [*Jorgenson et al.*, 2008] and the active layer is shallow with thaw depth ranging between 30-60 cm by late summer [*Arp et al.*, 2012b]. Marine sand and silt represent the dominant surficial geology. Vegetation consists primarily of sedges (*Carex* spp.) in drained thermokarst lake basins (DTLBs) and low-centered polygons, cotton grasses (*Eriopherum* spp.) form tussock tundra of high-centered polygons, and mosaics of sedges, willows (Salix spp.), and drawf birch (*Betula nana*) occur in riparian zones. Long, cold winters and short, cool summers with low precipitation, characterize of much of the ACP. At Fish Creek station (Table 1), mean annual air temperature is -10.7 °C, ranging from 8.8°C in July to -27.2°C in January (1998-2014) and total summer rainfall is 56 mm (no correction for undercatch, 2008-2014). Crea Creek provides habitat to many species of fish [*McFarland et al.*, 2017] and also functions as migration corridors between summer foraging habitat in lakes and overwinter habitat in alluvial rivers and nearby coastal estuaries [*Heim et al.*, 2016].

The Crea Creek Watershed has been a focal study area because of planned oil development as part of the Greater Moose's Tooth 1 (GMT 1) administrative unit [*BLM*, 2014] which has fueled the collection of baseline datasets to assess pre- and post-development impacts. In 2017, a permanent gravel road was constructed that bisects the Crea Creek catchment, with a bridge that crosses the

lower part of the creek below Lake L9819. Within this watershed, the two largest lakes L9819 and L9820 (Figure 1), which in most years have ephemeral and perennial connectivity to Crea Creek, respectively, have historically supplied liquid water and ice chips for ice road construction during the exploration and construction phases. Due to the proximity of these lakes to the gravel road, they will likely be utilized for further water supply during the production phase.

Field Observations for Model Forcing and Evaluation

The primary data and field measurements utilized in this study consisted of meteorological (primary model forcing), hydrological (runoff, end of winter SWE) and soil temperature time series (Table 1). Spatial data sets include a digital elevation model (DEM) [*EPSCoR-ACE*, 2013], land cover [*Payne et al.*, 2013], permafrost and surficial geology distribution [*Jorgenson et al.*, 2014], which are used to characterize the landscape and parameterize the model. Hourly snowfall records were derived from snow depth records collected by sonic sensors at Fish Creek and Inigok. Measured end-of-winter SWE was available at multiple sites within Crea Creek Watershed representing different land cover types (tundra, beaded stream, lakes). Deep permafrost temperatures were measured at the West Fish Creek deep borehole adjacent to the Fish Creek station [*Clow*, 2014]. Active layer and shallow permafrost temperatures were recorded at the Crea Creek station (Table 1). Stream discharge has been gauged close to its confluence with the Ublutouch River (Figure 1) beginning in 2009, as described in *Whitman et al.* [2011] and *Arp et al.* [2015b].

The hydrological model WaSiM

We used the physically-based spatially distributed (regular grid cells) **Wa**ter Balance **Si**mulation **M**odel (WaSiM), version 9.10.02.c, to simulate water flux and storage as well as soil temperatures, heat transfer and active layer dynamics at the watershed scale. WaSiM mass transfer modules include, but are not limited to, overland flow, ponding, moss and open water evaporation, evapotranspiration, snow accumulation and snow melt, snow distribution by wind, groundwater flow (2D lateral flow based on Darcy law) and soil water movement (1D vertical flow based on Richards equation).

A WaSiM model for Crea Creek Watershed was set up with a spatial resolution of 10 m to effectively represent topographic features, such as drained lake basins that are characteristic within the low-gradient ACP (Alaska). Simulations are carried out in an hourly time step for the period 2009 – 2014. Table 2 details the chosen modules and algorithms. We ran the WaSiM Crea application on a supercomputer (Comet), to which we have access as part of the Extreme Science and Engineering Discovery Environment (XSEDE https://portal.xsede.org/). The model was thoroughly calibrated and validated based on field measurements for the waters years 2009-2011 and 2012-2014, respectively. The statistical performance criteria include the Coefficient of Determination (r^2), Index of Agreement (IoA) [*Willmott*, 1981], Root Mean Square Error (RMSE) and Nash-Sutcliffe efficiency (NSE) [*Nash and Sutcliffe*, 1970].

Extreme climate and lake water-use scenarios

We developed three climate scenarios, one water-use scenario, and combinations thereof, 26 scenarios in total (Table 5), which were compared to a control scenario; each based on recently observed climate conditions and actual permitted water use amounts. The climate scenarios are based on the bias-corrected simulated meteorological output from the Polar version of the Weather

Research and Forecasting Model (WRF), which was forced by ERA-interim reanalysis data (1980-2014, ERA-WRF) [*Uppala et al.*, 2005], as detailed in *Cai et al.* [2018].

We selected the water years (October to September) with average precipitation (control, P_{JJAS} = 81 mm, $P_{Oct\text{-}May}$ = 106 mm) and the driest (DS, P_{JJAS} = 17 mm) and wettest (WS, P_{JJAS} = 117 mm) summers and driest (DW, $P_{Oct\text{-}May}$ = 64 mm) and wettest (WW, $P_{Oct\text{-}May}$ = 144 mm) winters (October-May) from the ERA-WRF downscaled output for our study area (Table 6). In our study's context, "dry" and "wet" only relates to precipitation, rather than combined precipitation and evapotranspiration. Scenarios extended for 10-year periods such that year 1 had the control climate, year 2 had the extreme climate, and years 3-10 control climate. To evaluate multi-year extreme climate conditions, we stacked extreme years after years 2, 3 and 4 to also look at cumulative responses and corresponding recovery compared to control scenario runs.

The winter lake water-use scenario (LWE) takes the same approach, but instead we removed water (about 30%) from the major lake in Crea Creek Watershed (Lake L9819), whose water has historically been used to support oil and gas development, during year 2 in one scenario (LWE-1) and in years 2 and 3 (LWE-2), years 2, 3 and 4 (LWE-3) and in all years (LWE-10). L9819 supports Arctic grayling and ninespine stickleback during summer and is deep enough to potentially provide overwintering habitat. Water-use scenarios were run using the control scenario climatology. The additional, and perhaps most important set of scenarios, used combined drought climate and water-use scenarios in order to understand the combined hydrologic responses. For example, lake water extraction for year 2 with a 3-year drought (years 2-4) is scenario DS-3 + LWE-1.

We primarily evaluated hydrologic responses to extreme climate and winter lake water extraction in terms of annual mean flow, annual minimum 7-day mean flow (AMQ7), and surface water connectivity. Additionally, we calculated the disconnectivity duration (DCD) and timing and the number of years for the system to return to control conditions after disturbance.

Principal Findings and Significance

WaSiM's simulated hydrological fluxes compare satisfactorily to the field measurements, which is reflected in the statistical performance criteria during calibration and validation (Table 7). The model is therefore regarded as suitable for the scenario analysis.

Climate scenarios

Forcing WaSiM with the DS and DW climate scenario results in a decrease of AMQ7, while forcing with the WS and WW scenarios produces an increase compared to the control (Figure 2). The hydrological system immediately (in the same year) responds to changes in the meteorological drivers. The response to multi-year disturbance is non-linear with the effect being strongest in the first year, after which it reduces or stays constant in magnitude. In all scenarios, the maximum impact occurs when 3 consecutive years of disturbance are simulated. In the DS-3 and DW-3 scenario, AMQ7 decreases by 69% (1.7 L s^{-1}) and 32% (3.7 L s^{-1}), respectively, while it increases by +42% (7.8 L s^{-1}) and +13% (6.2 L s^{-1}) in the WS-3 and WW-3 scenarios, respectively (Table 8). It takes one to three years after the disturbance to return to pre-disturbance conditions. Flow in Crea Creek falls below 6.5 L s^{-1} for 60 days (July 3rd to August 31st) for the DS-3 and 13 days (July 27th to August 8th) for the DW-3 scenario compared to the control scenario (11 days, July 28th to

August 8th). On the contrary, flow always exceeds 6.5 L s^{-1} WS-3 scenario. For the WW-3 scenario, discontinuity is reduced by 2 days (Table 8).

Lake extraction and combination of lake extraction and dry summer

The LWE scenarios result in a decrease of simulated AMQ7 and mean runoff at the watershed outlet in the summer immediately after water levels are lowered in lake L9819 (Table 8). The maximum AMQ7 reduction occurs in the LWE-3 scenario by -58% (Figure 3). The post-disturbance recovery is 3 years, except for LWE-1 where it is 2 years (Table 8). The combined impact of DS and LWE leads to a maximum reduction of AMQ7 of up to 91% (DS-3 + LWE-3) and a recovery time of 4 years after disturbance. In the DS-3 + LWE-3, AMQ7 reaches a value of 0.5 L s^{-1}. The lake water extraction entirely disconnects (throughout the whole summer) L9819 from the drainage network after three consecutive years of disturbance (Figure 3) The lake water extraction in the following years do not affect the AMQ7 as well as the mean flow, suggesting that the upstream area (16.2 km^2) of L9819 contributes about 60% of the flow to AMQ7 and 45% (180 mm) to the mean flow.

There are distinct differences in surface water connectivity between the control and the scenarios (WS-3, DS-3, DS-3 + LWE-3) at the outflow of the two larger lakes (Figure 4 a and b) and from the drained lake basin (DTLB, Figure 1) to Crea Creek (Figure 4 c). While surface water fluxes increase in the WS scenario at all locations, there is considerable decrease in the DS-3 and DS-3 + LWE-3. The maximum impact is simulated for the scenario DS-3 + LWE-3, where surface water fluxes entirely cease out of L9820 and L9819 in the third and the second year of disturbance, respectively. Lake L9819 only contributes to surface water drainage after three years of disconnection (=zero outflow). Surface water fluxes out of the DTLB nearly ceases entirely (only 1% of flow compared to control) in the third year of disturbance.

Discussion

Extreme climatic variability and human winter lake water extraction impact surface water connectivity and subsequently habitat for aquatic food webs. Our dynamic WaSiM simulations show a direct response and a large sensitivity of mean and low flows and consequently surface water connectivity to climate scenarios and increased winter lake water extraction. Cumulative effects, which we evaluated in the form of consecutive years of disturbance, are not sustained for magnitude to pre-disturbance conditions, suggesting a high non-linearity in hydrological processes and responses to external drivers/disturbances.

WaSiM simulations forced by DS, DW, LWE and the combined scenarios of DS and LWE lead to extreme low flows and general drying of Crea Creek watershed. The impact of DS on summer low flows would likely be even greater if summer air temperatures and radiation would exceed those of the control scenario. Although the drought conditions affect the surface water distribution in the entire watershed, low summer rainfall particularly impacts the lower part of the watershed that primarily feeds Crea Creek. Surface water connectivity to the two larger lakes (L9820 and L9819) becomes fragmented, limiting fish migration into these lakes in spring for foraging and inhibits their return in late summer to overwintering habitat outside Crea Creek. A longer-term disconnection of lakes to streams, as simulated at lake L9819 for the scenario DS-3 + LWE-3, may affect species distribution [*Heim et al.*, 2016] as well as fish assemblage composition [*Laske et al.*, 2016] when fragementation is sustained over longer time periods. Lower lake water levels at the

end of summer combined with low fall/winter air temperatures can lead to lakes freezing to the bottom (bedfast ice lake) during winter. Bedfast ice lakes provide neither liquid water for industries nor overwintering aquatic habitat. Higher fall/winter air temperatures may, however, lead to later freeze-up and thinner lake ice (floating ice lake) and therefore counterbalance lower lake water levels by still providing water and overwintering habitat. If there is sufficient snowfall, lake water levels may even be recharged during spring snowmelt, thereby counterbalancing potential storage deficits of the previous summer. Changing lake ice regimes, however, do not only affect freshwater habitat and water supply, but also lake ice-out timing, evapotranspiration and the thermal regime [*Arp et al.*, 2015a], which higlights the complexity and linkages/feedbacks of the processes occurring at the lanscape scale in Arctic tundra environments.

WaSiM simulations forced by the WS and WW scenarios, on the other hand, show increased AMQ7, increased freshwater fluxes and wetting of Crea Creek watershed relative to the control. The increase in AMQ7 is higher for the WS compared to WW scenario. WW mostly affects snowmelt runoff, which primarily recharges lakes/storages, while its effect is lower on late-summer low flows. The recovery time to pre-disturbance conditions is longer under the WW compared to WS scenario, as filled up storages release water generally more slowly and over longer time periods. Increasing precipitation in the Arctic, which is projected by regional to global climate models [*Cai et al.*, 2018], may in the long-term counterbalance the secondary effects of air temperature increases in the form of increased evapotranspiration and potentially subsurface drainage (as a result of permafrost thaw), and therefore support sustaining the large portion of lakes and wetlands characteristic for low-gradient Arctic tundra environments.

The presence and stability of permafrost close to the surface, which limits the water storage capacity of the subsurface, will play a major role in sustaining freshwater systems under continued and/or increased climate warming. The overall resilience of the hydrological system may be at risk if changes in climate and land use (as well as secondary changes such as permafrost/ice-wedge degradation) become even more extreme (in terms of climate variability) and changes pass certain thresholds/tipping points.

Products

Gädeke A., Arp C., Liljedahl A., Daanen R., Whitman M., Cai L., Alexeev V., Jones B., Wipfli M., Schulla J. (2018), The impact of climate extremes and lake water-use on stream flows and connectivity in an Arctic Coastal Plain watershed in northern Alaska (in preparation, submission planned for late summer/fall 2018 to Water Resources Research).

Cai, L., V. A. Alexeev, C. D. Arp, B. M. Jones, A. K. Liljedahl, and **A. Gädeke** (2018), The Polar WRF Downscaled Historical and Projected Twenty-First Century Climate for the Coast and Foothills of Arctic Alaska, *Frontiers in Earth Science*, 5(111), doi:10.3389/feart.2017.00111.

Jones, B. M., C. D. Arp, M. S. Whitman, D. A. Nigro, I. Nitze, J. Beaver, **A. Gädeke**, C. Zuck, A. K. Liljedahl, R. P. Daanen, E. Torvinen, S. Fritz, and G. Grosse (2017), A lake-centric geospatial database to guide research and inform management decisions in an Arctic watershed in northern Alaska experiencing climate and land-use changes, *Ambio*, doi:10.1007/s13280-017-0915-9.

Previous work (non-NIWR supported, however, essential to achieving final outcome)

Gädeke A., Liljedahl A., Arp, C. D., Daanen R., Jones B., Alexeev V., Cai L., Whitman M., Wipfli M. (2016) Water-fish-climate nexus in the Arctic Coastal Plain, Alaska: Processed based hydrological modeling to assess changes in surface water connectivity. American Water Resources Association Spring Specialty Conference (Water-Energy-Environment), April 25 to 28, Anchorage, Alaska, USA.

Gädeke A., Liljedahl A., Arp, C. D., Daanen R., Jones B., Alexeev V., Cai L (2016) Processed-based hydrological modeling of a continuous permafrost catchment on the Arctic Coastal Plain, Alaska to evaluate how climate change will affect surface water runoff and connectivity. XI. International Conference on Permafrost, 20 - 24 June 2016, Potsdam, Germany.

Student Support

The postdoctoral fellow Anne Gaedeke was trained under the guidance of Research Associate Professor Dr. Christropher Arp (UAF).

Notable Awards and Achievements

Not applicable.

Tables and Figures

Tables

Table 1: Overview of meteorological and hydrological data base (T=air temperature, RH=air humidity, WS=wind speed, SR=solar radiation, R=rain, SN=snow depth, USGS=U.S. Geological Survey GTN-P Active-Layer Monitoring Site, Alaska)

Name/ID	**Location (Lat, Lon, Elevation)**	**Variables**	**Record length**	**Data source/ Agency**
Meteorology				
Crea	(70.3°N, -151.3°W, 5 m)	T, RH, SR, WS, R	7/2011-present	Fish Creek Watershed Observatory [1]
Fish Creek	(70.4°N, -152.1°W, 31 m)	T, SR, WS, R, SN	8/1998-2014	USGS [2]
Inigok	(70.1°N, -153.3°W, 53 m)	T, SR, WS, R, SN	8/1998-2014	USGS [2]
Nuiqsut (USAF WBAN ID 703644 27515)	(70.2°N, -151.0°W, 17 m)	T, RH, WS	2006-2014	Global Surface Hourly database [3]
Hydrology				
Crea	(70.3°N, -151.3°W, 5 m)	Runoff	2011-present	Fish Creek Watershed Observatory*
Tundra Lake L9819 Lake L9820	(70.3°N, -151.3°W, 5 m)	End of winter snow accumulation	2010, 2011, 2012	Fish Creek Watershed Observatory*
Crea	(70.3°N, -151.3°W, 5 m)	Soil temperature	5/2013-present	Fish Creek Watershed Observatory*

Table 2: WaSiM modules and algorithms used for modeling of Crea Creek watershed

Hydrological process/Module	**Algorithm**
Precipitation correction	Temperature and wind dependent correction after *Sevruk* [1986]; Correction is done separately for rain and snow
Interpolation of meteorological input data	Inverse Distance Weighting approach
Evapotranspiration	Penman-Monteith approach [*Monteith and Unsworth*, 1990]
Snow accumulation and melt	Snow accumulation by threshold temperature, snow-melt by energy balance approach as detailed in Warscher et al. (REFERENCE)
Interception	Linear bucket approach
Runoff generation	Implicit runoff generation using *Richards* [1931] approach
Soil water dynamic	Vertical water movement in the unsaturated zone of the soil based on the Richards Equation [*Richards*, 1931] with parameterization after *van Genuchten* [1980]
Heat transfer	Implicit solution of the heat transport equation in the soil (Fourier law), 1D-vertical (finite difference method) Heat advection/convection based on method presented in *Daanen and Nieber* [2009] Consideration of the soil hydraulic properties during freezing and thawing of the soil
Groundwater dynamic	Iterative solution of flow and transport equation (finite difference method)
Surface Water Routing	2D flow equation solved by implicit Gauss-Seidel approach

Table 3: Ranges of WaSiM land cover parameters. Land cover parameters are set on monthly to semi-monthly temporal resolution. Values include leaf area index (LAI), root depths, snow-free albedo (α) , Z0 roughness lengths, r_{sc} leaf surface resistance, r_{si} interception surface resistance, r_{se} evaporation surface resistance, vegetation covered fraction (VCF), n-factor to estimate surface temperatures based on [*Kade et al.*, 2006] and [*Lunardini*, 1978]. Water shallow and deep differ regarding their n-factors during winter (from October to May) as well as the timing of reduction of r_{se} and r_{sc} after during summer. Deeper lakes (floating ice lakes) are assumed to ice-out on average 17 days later compared to shallower bedfast ice lakes (Arp et al., 2015).

	LAI [-]	**Root Depth [m]**	**α [-]**	**r_{se} [s m^{-1}]**	**r_{sc} [s m^{-1}]**	**r_{si} [s m^{-1}]**	**Z0 [m]**	**VCF [-]**	**n-factor**
Wet sedge	0-0.35	0.05-0.2	0.15	80-500	40-100	0.5	0.02-0.03	0.3-0.7	0.6-0.7
Tussocks	0-0.53	0.1-0.3	0.15	200-500	10-500	0.5	0.02-0.03	0.6-0.8	0.5-0.55
Shrub	0-0.5	0.1-0.4	0.17	200-500	100-500	0.5	0.01-0.02	0.6-0.8	0.4-0.8
$Water_{shallow}$	1	1	0.15	25-90	25-90	0.5	0.1	1	-0.025-0.5
$Water_{deep}$	1	1	0.15	25-90	25-90	0.5	0.1	1	-0.1-0.5

Table 4: WaSiM parameters for unsaturated zone, including parameters for the heat transfer module.

	Organic	**Silt**	**Sand**	**Mineral**
Dry heat capacity [J (kg*K) $^{-1}$]	2500	2500	2500	810
Dry density [kg (m^3) $^{-1}$]	40	1500	1300	1450
Dry thermal conductivity [W (m*K) $^{-1}$]	0.5	0.6	0.85	0.97
Hydraulic conductivity of frozen soil [m/s]	1.0e-10	1.0e-10	1.0e-10	1.0e-10
Hydraulic conductivity of unfrozen soil [m s^{-1}]	1.0e-04	2.05e-05	2.1e-05	1.0e-05
Saturated water content (fillable porosity [-])	0.8	0.48	0.35	0.4
Residual water content [-]	0.02	0.07	0.057	0.05
Van Genuchten parameter α	5.0	2.0	4.0	2.34
Van Genuchten parameter n	2.0	2.5	3.0	1.23
Thickness of layer [m]*	0.1	0.1	0.1	2
Number of layers *	1	10	9	13

Table 5: Set-up of the climate change and winter lake water extraction scenarios. The climate change scenarios are based on bias-corrected WRF simulations forced by reanalysis data for the domain of Crea Creek watershed (six grid cells, 10 km spatial resolution, 3 hourly temporal resolution). The control scenario (C) represents the climate of the water year 1996 (October 1995-September 1996). The dry (DS) and wet (WS) summer year are made up of the meteorological variables of the control scenario (October 1995 – May 1996) and the months JJAS (June – September) of 2007 and 2006, respectively. The dry and wet winter years are made up of October – May of 2014 and 1987, respectively, and JJAS of the control year 1996. The meteorological variables of the control scenario force the lake extraction (LWE).

Name		**Water Year**				
		1	2	3	4	5-10
Control (C)		C	C	C	C	C
Dry Summer (DS)	DS-1	C	DS	C	C	C
	DS-2	C	DS	DS	C	C
	DS-3	C	DS	DS	DS	C
Wet Summer (WS)	WS-1	C	WS	C	C	C
	WS-2	C	WS	WS	C	C
	WS-3	C	WS	WS	WS	C
Wet Winter (WW)	WW-1	C	WW	C	C	C
	WW-2	C	WW	WW	C	C
	WW-3	C	WW	WW	WW	C
Dry Winter (DW)	DW-1	C	DW	C	C	C
	DW-2	C	DW	DW	C	C
	DW-3	C	DW	DW	DW	C
Lake Water Extraction (LWE)	LWE-1	C	LWE	C	C	C
	LWE-2	C	LWE	LWE	C	C
	LWE-3	C	LWE	LWE	LWE	C
	LWE-10	C	LWE	LWE	LWE	LWE
DS-1 + LWE	DS-1 + LWE-1	C	DS+LWE	C	C	C
	DS-1 + LWE-2	C	DS+LWE	LWE	C	C
	DS-1 + LWE-3	C	DS+LWE	LWE	LWE	C
	DS-1 + LWE-10	C	DS+LWE	LWE	LWE	LWE
DS-2 + LWE	DS-2 + LWE-1	C	DS+LWE	DS	C	C
	DS-2 + LWE-2	C	DS+LWE	LWE+DS	C	C
	DS-2 + LWE-3	C	DS+LWE	LWE+DS	LWE	C
DS-3 + LWE	DS-3 + LWE-1	C	DS+LWE	DS	DS	C
	DS-3 + LWE-2	C	DS+LWE	LWE+DS	DS	C
	DS-3 + LWE-3	C	DS+LWE	LWE+DS	LWE+DS	C

Table 6: Overview of meteorological characteristics of climate change scenarios. The measured meteorological variables air temperature and precipitation (Nuiqsut Airport (USAF WBAN ID 703644 27515, 70.212° N, -151.002° W)) are compared to the simulated bias-corrected WRF output forced by reanalysis data [*Cai et al.*, 2018]. The simulated values represent the average of 6 grid cells covering Crea Creek watershed. Air temperature and precipitation are analyzed annually (mean annual air temperature (MAAT)), summer months June – September (JJAS) and winter months October – May (Oct-May). The year 1996 presents the control year, 2007 the low rainfall summer, 2006 the high rainfall summer and 2014 the warmer and high snowfall scenario. The climate scenario years were selected solely based on precipitation (summer (JJAS) for dry summer (DS), wet summer (WS) and winter (Oct-May) for wet winter (WW), dry winter (DW)). The climate input for the lake water-use scenario (LWE) is identical to the control (C).

	Year(s)	**MAAT [°C]**	**$P_{(JJAS)}$ [mm]**	**$P_{(Oct-May)}$ [mm]**
Measurements				
Average measurements at Nuiqsut	2000-2016	-10.2	57* 68**	71-105***
Simulated output from bias-corrected WRF forced by reanalysis data				
C (and LWE)	1996	-9.6	81	106
DS	2007	-9.4	17	72
WS	2006	-9.8	117	103
DW	1987	-11.5	59	64
WW	2014	-7.7	55	144
Average RA	1981-2014	-10.2	70	101

* without correction for rainfall undercatch
** corrected for rainfall undercatch (correction factor of 1.2)
*** average end-of-winter SWE from Crea Creek watershed (2012-2014), range results from applying a snow density of 0.21 g $(cm^3)^{-1}$ to 0.31 g $(cm^3)^{-1}$

Table 7: Statistical performance indicators to evaluate agreement between daily measured and simulated discharge during calibration (2009-2011) and validation (2011-2014). Model performance is evaluated based on the Nash Sutcliffe efficiency (NSE), Root Mean Square Error (RMSE), Coefficient of Determination (r^2), Index of Agreement (IoA) and mass balance error (MBE) [%])

Year	**NSE**	**RMSE**	**r^2**	**IoA**	**MBE**
2009	0.67	0.04	0.74	0.9	+0.8
2010	0.78	0.04	0.83	0.93	-50
2011	-0.86	0.06	0.18	0.59	+13
2012	0.63	0.06	0.74	0.85	-5.0
2013	0.60	0.08	0.88	0.82	-37
2014	0.39	0.05	0.59	0.76	-10

Table 8: Mean runoff, annual minimum 7-day mean flow (AMQ7), Disconnectivity Duration (DCD) and the time period of the DCD of the simulated extreme scenarios. AMQ7 represents, DCD Disconnectivity Duration (when mean daily discharge is below 6.5 L s^{-1}). The mean annual runoff is calculated for the thawed season (May-August). Values are reported for the years of (last) disturbance (scenario-1: year 2, scenario-2: year 3, scenario-3: year 4, scenario-10: year 10). The recovery time assumes that the AMQ7 returns to the control value ±2%.

Scenario		**Mean runoff [L s^{-1}]**	**AMQ7 [L s^{-1}]**	**DCD [days]**	**Timing [month/day]**	**Duration [years]**
Control	C	325	5.5	11	7/28-8/8	-
Dry Summer (DS)	DS-1	214	2.4	33	7/4-8/5	3
	DS-2	163	1.9	60	7/3-8/31	3
	DS-3	160	1.7	60	7/3-8/31	3
Wet summer (WS)	WS-1	543	7.0	2	7/12-7/13	1
	WS-2	506	7.4	-	-	2
	WS-3	514	7.8	-	-	2
Dry winter (DW)	DW-1	234	4.1	13	7/27-8/8	2
	DW-2	233	3.8	13	7/27-8/8	2
	DW-3	232	3.7	13	7/27-8/8	2
Wet Winter (WW)	WW-1	495	5.8	10	7/29-8/8	2
	WW-2	499	6.1	7	7/29-8/5	3
	WW-3	501	6.2	3	7/31-8/2	3
Lake Water Extraction (LWE)	LWE-1	151	3.1	15	7/26-8/9	2
	LWE-2	146	2.6	15	7/26-8/9	3
	LWE-3	145	2.3	15	7/26-8/14	3
	LWE-10	145	2.3	20	7/26-8/14	-
DS-1 + LWE 1,2,3,10	DS-1 + LWE-1	49	1.0	64	6/29-8/31	3
	DS-1 + LWE-2	138	2.1	20	7/26-8/14	3
	DS-1 + LWE-3	145	2.3	15	7/26-8/9	3
	DS-1 + LWE-10	145	2.3	20	7/26-8/14	-
DS-2 + LWE 1,2,3	DS-2 + LWE-1	49	1.1	64	6/29-8/31	4
	DS-2 + LWE-2	39	0.7	64	6/29-8/31	3
	DS-2 + LWE-3	136	1.8	20	7/26-8/14	3
DS-3 + LWE 1,2,3	DS-3 + LWE-1	49	1.0	64	6/29-8/31	5
	DS-3 + LWE-2	39	0.7	64	6/29-8/31	4
	DS-3 + LWE-3	37	0.5	64	6/29-8/31	4

Figures

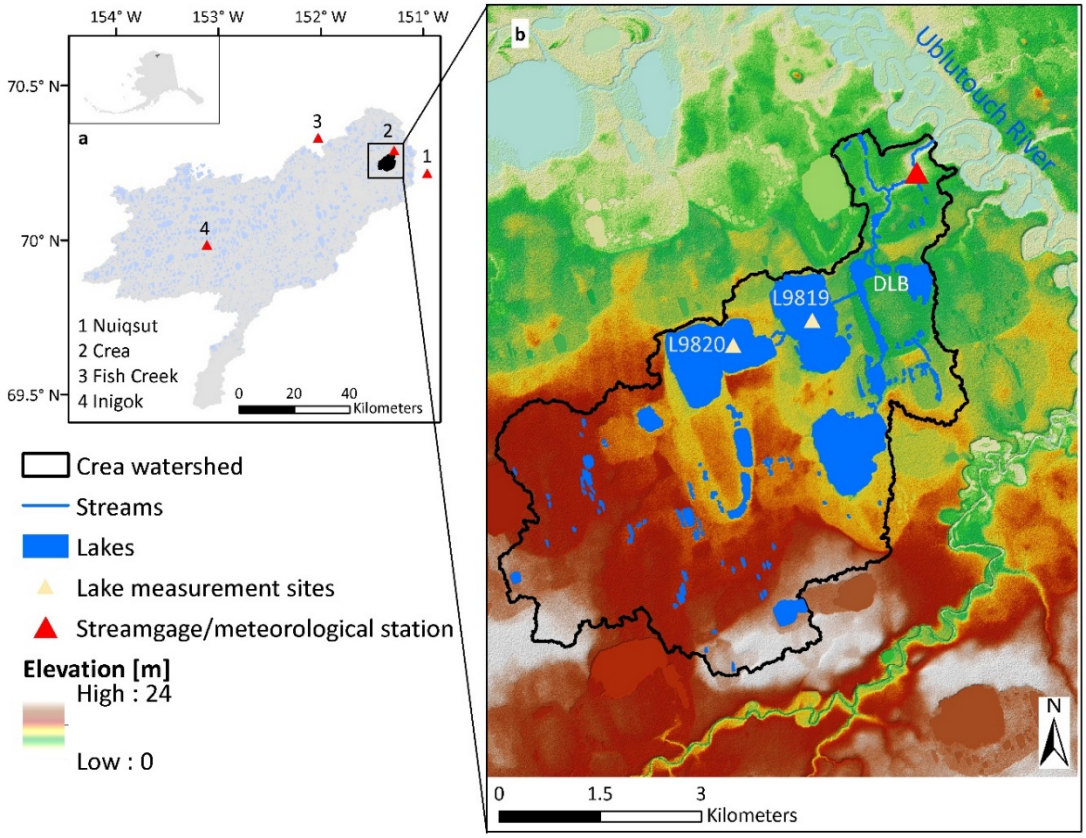

Figure 1: Location of Crea Creek watershed. Crea Creek watershed is a sub-watershed of Fish Creek (~4900 km^2). Four weather stations with (nearly) complete meteorological records for the water years 2008-2014 are used in this study (a). Crea Creek watershed is located in a low-gradient landscape and has been monitored since 2009 (b). The two larger lakes in Crea Creek watershed are referred to as L9830 (upper) and L9819 (lower). The drained lake basin (DTLB) in the lower part of the watershed is also indicated in the map.

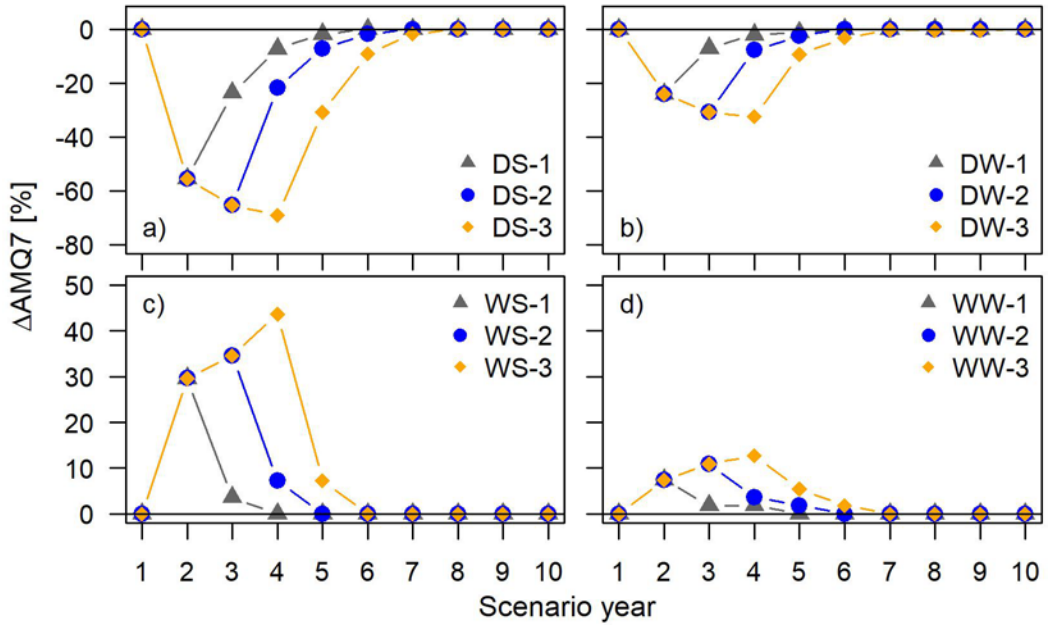

Figure 2: Impact of climate change scenarios on simulated annual minimum 7-day mean flow (AMQ7), presented as percent change between the control and the scenario simulations. The meteorological variables of the control scenario and the climate scenarios (all combinations), dry (DS-1, DS-2, DS-3) and wet (WS-1, WS-2, WS-3) summers as well as dry (DW-1, DW-2, DW-3) and wet (WW-1, WW-2, WW-3) winters, forced WaSiM.

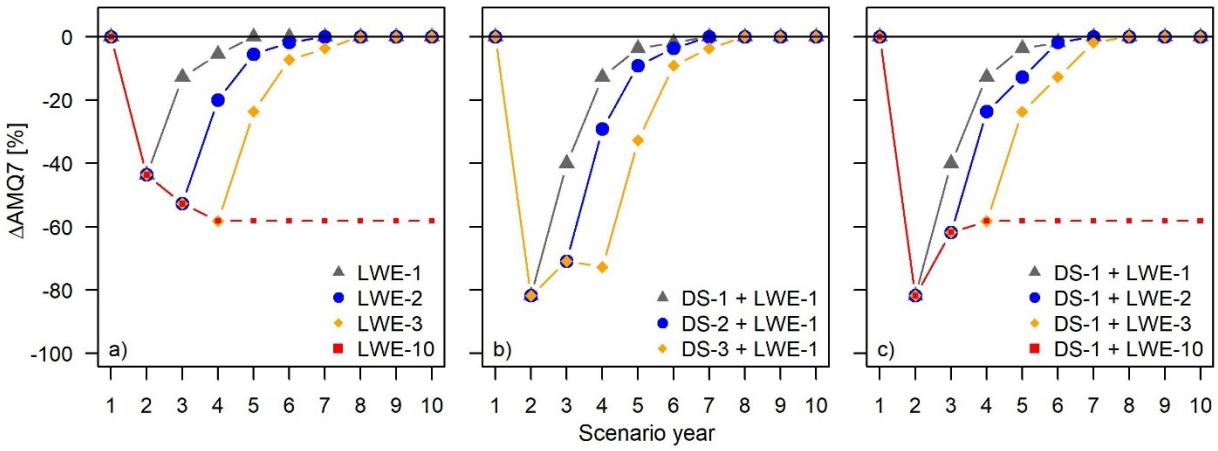

Figure 3: Impact of winter lake water extraction (LWE) and combined dry summer (DS) and LWE on simulated annual minimum 7-day mean flow (AMQ7). The single and multi-year LWE scenarios are forced by the meteorological variables of the control scenario (a). The DS-LWE scenarios combine one to three consecutive years of DS with LWE (b, c). The impact on the AMQ7 is presented as percent difference to the control.

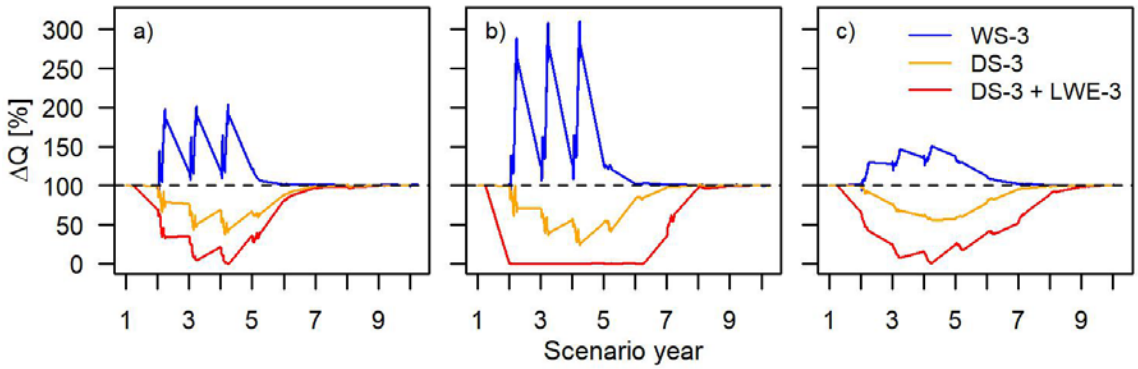

Figure 4: Simulated percent differences in summer (June-August) surface water fluxes between scenarios relative to control at lake/drained lake basin outlets. The surface water fluxes present the average of 111 grid cells downstream of L9820 (a), 117 grid cells downstream of L9819 (b) and 2 grid cells at the outlet lower drained lake basin (c). The black dashed line at 100% represents the control scenario.

References

Arp, C. D., B. M. Jones, Z. Lu, and M. S. Whitman (2012a), Shifting balance of thermokarst lake ice regimes across the Arctic Coastal Plain of northern Alaska, *Geophys. Res. Lett.*, *39*(16), L16503.

Arp, C. D., B. M. Jones, A. K. Liljedahl, K. M. Hinkel, and J. A. Welker (2015a), Depth, ice thickness, and ice-out timing cause divergent hydrologic responses among Arctic lakes, *Water Resour. Res.*, *51*(12), 9379-9401.

Arp, C. D., M. S. Whitman, B. M. Jones, R. Kemnitz, G. Grosse, and F. E. Urban (2012b), Drainage Network Structure and Hydrologic Behavior of Three Lake-Rich Watersheds on the Arctic Coastal Plain, Alaska, *Arct. Antarct. Alp. Res.*, *44*(4), 385-398.

Arp, C. D., M. S. Whitman, B. M. Jones, G. Grosse, B. V. Gaglioti, and K. C. Heim (2015b), Distribution and biophysical processes of beaded streams in Arctic permafrost landscapes, *BGeo*, *12*(1), 29-47.

Betts, E. D., and D. L. Kane (2015), Linking North Slope of Alaska climate, hydrology, and fish migration, *Hydrol. Res.*, *46*(4), 578-590.

BLM (2014), Supplemental Environmental Impact Statement for the Alpine Satellite Development Plan for the Greater Moose's Tooth One Development Project, US Department of the Interior, Bureau of Land Management, Anchorage, Alaska, USA.

Bowling, L. C., D. L. Kane, R. E. Gieck, L. D. Hinzman, and D. P. Lettenmaier (2003), The role of surface storage in a low-gradient Arctic watershed, *Water Resour. Res.*, *39*(4), 1087.

Cai, L., V. A. Alexeev, C. D. Arp, B. M. Jones, A. K. Liljedahl, and A. Gädeke (2018), The Polar WRF Downscaled Historical and Projected Twenty-First Century Climate for the Coast and Foothills of Arctic Alaska, *Frontiers in Earth Science*, *5*(111).

Clow, G. D. (2014), Temperature data acquired from the DOI/GTN-P Deep Borehole Array on the Arctic Slope of Alaska, 1973–2013, *Earth Syst. Sci. Data*, *6*(1), 201-218.

Daanen, R. P., and J. L. Nieber (2009), Model for Coupled Liquid Water Flow and Heat Transport with Phase Change in a Snowpack, *J. Cold Regions Eng.*, *23*(2), 43-68.

Déry, S. J., M. A. Hernández-Henríquez, J. E. Burford, and E. F. Wood (2009), Observational evidence of an intensifying hydrological cycle in northern Canada, *Geophys. Res. Lett.*, *36*(13), L13402.

EPSCoR-ACE (2013), Established Program to Stimulate Competitive Research - Alaska Adapting to Changing Environments, LiDAR Data: Crea Creek Watershed Area, http://alaska.portal.gina.alaska.edu/catalogs/11475-lidar-data-crea-creek-watershed-area.

Heim, K. C., M. S. Wipfli, M. S. Whitman, C. D. Arp, J. Adams, and J. A. Falke (2016), Seasonal cues of Arctic grayling movement in a small Arctic stream: the importance of surface water connectivity, *Environ. Biol. Fishes*, *99*(1), 49-65.

Hodson, D. L. R., S. P. E. Keeley, A. West, J. Ridley, Hawkins, and H. T. Hewitt (2013), Identifying uncertainties in Arctic climate change projections, *Clim. Dyn.*, *40*(11), 2849-2865.

Instanes, A., V. Kokorev, R. Janowicz, O. Bruland, K. Sand, and T. Prowse (2016), Changes to freshwater systems affecting Arctic infrastructure and natural resources, *J. Geophys. Res. Biogeosci.*, *121*(3), 567-585.

Jones, B. M., G. Grosse, C. D. Arp, M. C. Jones, K. M. Walter Anthony, and V. E. Romanovsky (2011), Modern thermokarst lake dynamics in the continuous permafrost zone, northern Seward Peninsula, Alaska, *J. Geophys. Res. Biogeosci.*, *116*(G2), G00M03.

Jones, B. M., G. Grosse, C. D. Arp, E. Miller, L. Liu, D. J. Hayes, and C. F. Larsen (2015), Recent Arctic tundra fire initiates widespread thermokarst development, *Sci. Rep.*, *5*, 15865.

Jones, B. M., et al. (2017), A lake-centric geospatial database to guide research and inform management decisions in an Arctic watershed in northern Alaska experiencing climate and land-use changes, *Ambio*.

Jorgenson, M. T., Y. L. Shur, and E. R. Pullman (2006), Abrupt increase in permafrost degradation in Arctic Alaska, *Geophys. Res. Lett.*, *33*(2), L02503.

Jorgenson, M. T., M. Kanevskiy, Y. Shur, J. Grunblatt, C. L. Ping, and G. J. Michaelson (2014), Permafrost database development, characterization, and mapping for Northern Alaska, http://file-sctc.gina.alaska.edu/public/NoAKPermafrost_Mapping.pdf.

Jorgenson, M. T., K. Yoshikawa, M. Kanevskiy, Y. L. Shur, V. Romanovsky, S. Marchenko, G. Grosse, J. Brown, and B. M. Jones (2008), Permafrost characteristics of Alaska, *Ninth International Conference on Permafrost (NICOP)*.

Kade, A., V. E. Romanovsky, and D. A. Walker (2006), The n-factor of nonsorted circles along a climate gradient in Arctic Alaska, *Permafr. Periglac. Proc.*, *17*(4), 279-289.

Lantz, T. C., and S. V. Kokelj (2008), Increasing rates of retrogressive thaw slump activity in the Mackenzie Delta region, N.W.T., Canada, *Geophys. Res. Lett.*, *35*(6), n/a-n/a.

Laske, S. M., T. B. Haynes, A. E. Rosenberger, J. C. Koch, M. S. Wipfli, M. S. Whitman, and C. E. Zimmerman (2016), Surface water connectivity drives richness and composition of Arctic lake fish assemblages, *Freshwat. Biol.*, *61*, 1090-1104.

Lawrence, D. M., and A. G. Slater (2005), A projection of severe near-surface permafrost degradation during the 21st century, *Geophys. Res. Lett.*, *32*(24), L24401.

Lesack, L. F. W., and P. Marsh (2010), River-to-lake connectivities, water renewal, and aquatic habitat diversity in the Mackenzie River Delta, *Water Resour. Res.*, *46*(12), n/a-n/a.

Liljedahl, A. K., et al. (2016), Pan-Arctic ice-wedge degradation in warming permafrost and its influence on tundra hydrology, *Nat. Geosci.*, *9*(4), 312-318.

Lunardini, V. J. (1978), Theory of N-factors and correlation of data, paper presented at Proceedings of the Third International Conference on Permafrost, National Counsel of Canada, Ottawa.

McFarland, J. J., M. S. Wipfli, and M. S. Whitman (2017), Trophic pathways supporting Arctic grayling in a small stream on the Arctic Coastal Plain, Alaska, *Ecol. Freshwat. Fish*, n/a-n/a.

Monteith, J. L., and M. H. Unsworth (1990), *Principles of Environmental Physics*, 422 pp., Second Edward Arnold, London.

Nash, J. E., and J. V. Sutcliffe (1970), River flow forecasting through conceptual models part I — A discussion of principles, *J. Hydrol.*, *10*(3), 282-290.

Oelke, C., T. Zhang, and M. C. Serreze (2004), Modeling evidence for recent warming of the Arctic soil thermal regime, *Geophys. Res. Lett.*, *31*(7), n/a-n/a.

Payne, J., S. Guyer, D. Fehringer, and K. Boggs (2013), North Slope Science Initiative Landcover Mapping Summary Report, http://catalog.northslope.org/catalog/entries/8309.

Rawlins, M. A., et al. (2010), Analysis of the Arctic system for freshwater cycle intensification: observations and expectations, *J. Clim.*, *23*(21), 5715-5737.

Richards, L. A. (1931), Capillary Conduction of liquids through porous mediums *JAP*, *1*(5), 318-333.

Serreze, M. C., and J. A. Francis (2006), The Arctic amplification debate, *Clim. Change*, *76*(3-4), 241-264.

Sevruk, B. (1986), Correction of precipitation measurements, *Geographische Schriften*, *23*, Zürich.

Stuefer, S. L., C. D. Arp, D. L. Kane, and A. K. Liljedahl (2017a), Recent Extreme Runoff Observations From Coastal Arctic Watersheds in Alaska, *Water Resour. Res.*, n/a-n/a.

Stuefer, S. L., C. D. Arp, D. L. Kane, and A. K. Liljedahl (2017b), Recent Extreme Runoff Observations From Coastal Arctic Watersheds in Alaska, *Water Resour. Res.*, *53*(11), 9145-9163.

Uppala, S. M., et al. (2005), The ERA-40 re-analysis, *Q. J. Roy. Meteorol. Soc.*, *131*(612), 2961-3012.

van Genuchten, M. T. (1980), A closed-form equation for predicting the hydraulic conductivity of unsaturated soils, *Soil Sci. Soc. Am. J.*, *44*(5), 892-898.

Whitman, M. S., C. D. Arp, B. M. Jones, W. Morris, G. Grosse, F. E. Urban, and R. Kemnitz (2011), Developing a long-term aquatic monitoring network in a complex watershed of the Alaskan Arctic Coastal Plain, paper presented at Fourth Interagency Conference on Research in Watersheds: Observing, Studying, and Managing for Change, USGS, Reston.

Willmott, C. J. (1981), On the validation of models, *PhGeo*, *2*, 184-194.

Woo, M. K. (1986), Permafrost hydrology in North America, *Atmos. Ocean*, *24*(3), 201-234.

Laboratory Investigation of Rheology and Infiltration Process of Non-Newtonian Fluids through Porous Media in a Non-Isothermal Flow Regime for Effective Remediation of Persistent Contaminants

Basic Information

Title:	Laboratory Investigation of Rheology and Infiltration Process of Non-Newtonian Fluids through Porous Media in a Non-Isothermal Flow Regime for Effective Remediation of Persistent Contaminants
Project Number:	2017AK136B
Start Date:	3/1/2017
End Date:	2/28/2018
Funding Source:	104B
Congressional District:	AK-001
Research Category:	Ground-water Flow and Transport
Focus Categories:	Groundwater, Hydrology, Methods
Descriptors:	None
Principal Investigators:	Debasmita Misra

Publication

1. Naseer, F., O. Awoleke, D. Misra and M. Abou Najm, 2017, Effect of Temperature on Guar Gum Rheology of Different Concentrations,Paper#H43I-1768 in Fall Meeting of the American Geophysical Union, December 11 – 15, New Orleans, LA.

Project Title: Laboratory Investigation of Rheology of Non-Newtonian Fluids for Effective Remediation of Persistent Contaminants from Porous Media under Non-isothermal Flow Regimes

Principal Investigator: Dr. Debasmita Misra, dmisra@alaska.edu, 907-474-5339

Abstract

The overarching objective of this research is to study a methodology for using non-Newtonian fluids for effective remediation of persistent (strongly adsorbed) contaminants in porous media under non-isothermal flow regimes. For effective remediation of persistent contaminants in non-isothermal flow conditions, it is critical to understand the change in rheology of non-Newtonian fluids under different temperature regimes. Non-Newtonian fluid rheology has not been well studied under cold temperature regimes. The goal was to expose different concentrations of non-Newtonian fluids (Guar gum and Xanthan gum solutions) to temperatures ranging from 30 ºC to -5 ºC to study the changes in viscosity and shear stress with change in shear strain of the fluid. Experiments at above zero temperatures were recorded, but the fluid froze completely at subzero temperatures, regardless of concentration. The understanding of the rheological changes in non-Newtonian fluids exposed to colder temperatures will help us in understanding the characteristics of flow in those regimes and effectiveness of remediation of persistent contaminants. The analysis of flow characteristics and remediation will be compared to those of Newtonian fluids at specific temperatures used to study the non-Newtonian fluids. Through these future experiments, the mobility and behavior of non-Newtonian fluids will be characterized under varying temperatures and their effectiveness in removing contaminants from soils will be understood. The impact of temperature change on the fluid and flow stability in the porous medium will be examined. The outcome of this research will provide critical knowledge for cost effective, environmentally benign and time efficient remediation of contaminated soils in Alaska and other cold regions.

Problem/Motivation and Research Objectives

Fluid flow and contaminant transport in porous media are significant to a wide range of fields, including hydrology, ecology, geomorphology, and agricultural science, as well as petroleum, chemical and environmental engineering. Non-Newtonian fluids are not uncommon to porous media applications, such as soil and groundwater remediation, propagation of blood in kidneys, hydraulic fracture and enhanced oil recovery and cement injection in soils (Abou Najm and Atallah, 2016).

Contamination of soil and groundwater by persistent contaminants, such as phosphates, carbon tetrachloride, chlorinated aliphatic hydrocarbons (CAH), certain emerging contaminants, and certain heavy metals have been of major concern (e.g., Jung, et al., 2016; Palaniappan et al., 2010; Barnes et al., 2007). Water quality is increasingly threatened as human populations grow, industrial and agricultural activities expand, and climate change threatens to cause major alterations in the hydrologic cycle. Inadequately treated sewage, industrial and agricultural or food wastes, dissolved metals and many emerging contaminants migrate through the soil to pollute the groundwater on a daily basis. Contamination is not limited to sewage or industrial and

agricultural wastes; mining, oil and gas exploration and production, and industrial and nuclear plants are adding to the problem.

A lack of understanding of fate and transport of contaminants within the soil matrix and groundwater makes the situation worse. Preferential flow of contaminants through soil to groundwater is defying the conceptual understanding of flow and transport through porous media. Adding to the complexity are the highly persistent contaminants that do not travel at a rate proportional to the flux rate of water in the porous media. Experimental and field observations show that the contaminants do not necessarily adhere to the flow pathway and velocity of water in porous media.

With climate change being experienced at a rapid rate in Alaska, soil and groundwater contamination is emerging as a great concern due to anticipated increase in precipitation, melting of permafrost, increased storm events and degradation of previously contaminated soils. Soil contamination in Alaska may be caused at industrial sites such as mining heaps, dumps, filled natural depressions, and quarries (Meuser, 2010). Mine drainage contains metals, salts, coal and other minerals that may be highly adsorbed to soils and within saturated porous media. According to Palaniappan et al. (2010), there are approximately 500,000 abandoned mines in the United States. The state of Colorado alone has 23,000 abandoned mines that have polluted 2,300 km of streams. Oil and gas industrial processes like hydraulic fracturing and oil purification, as well as oil and gas storage, pipelines, and oil spills are contributing to soil and water contamination (Jung et al., 2016). With the potential for increased prevalence of adsorbed contaminants in soils and aquifers in Alaska's rapidly changing climatic environment, it is critical that cost effective and time effective remediation measures be developed and tested.

Biopolymers such as polyacrylamide (PAM) and Xanthan gum have shown great promise for enhanced oil recovery (EOR) because they lead to an increase in the viscosity of water, decrease in the mobility of water, and contact with a larger volume of the reservoir (Blokker, 2014; Pollock et al., 1994; Hove et al., 1990). Guar gum is also an excellent candidate for remediation of contaminated soils (Velimirovic et al., 2014). It is a non-Newtonian, sheer thickening (viscosity decreases with increase in stress) fluid. Mixing Guar gum with water increases the viscosity and allows for better transportation and suspension of the fluid. Guar gum is naturally biodegradable and thus has almost no environmental impacts on the soil. Hence, both Xanthan gum and Guar gum will be used as non-Newtonian fluids to assess their effectiveness in remediation of persistent contaminants in porous media.

While laboratory- and field scale studies, including modeling of non-Newtonian fluids as remediation agents in porous media, have been conducted, such studies have been limited to porous media temperatures of approximately 30°C. According to Jung et al. (2016), previous work on biopolymers were limited to the evaluation of shear strength, stiffness, and erosion resistance properties of soils saturated with biopolymer solutions. Little is known about the flow characteristics of biopolymer solutions through a porous medium, especially in the range of low temperatures that are experienced in Alaska or other similar cold regions.

Complexities associated with pore structures hinder flow model development for a porous media. Proper understanding of complex pore structures and flow patterns in the media is most important. A knowledge of such complexity will provide an opportunity to study and compare the behavior of non-Newtonian and Newtonian fluids under different temperature regimes in soil. It is critical to understand the impact of temperature on the flow or rheology of Guar gum and Xanthan gum in soil because the adsorption kinetics of each persistent contaminant is different. Once the flow and rheology are well understood, the effectiveness of Guar gum or Xanthan gum in remediation of persistent contaminants can be studied. The outcome of this research will provide valuable input to the remediation of soil and saturated porous media in extremely cold regions, such as Alaska. This knowledge could be transferred for field-scale pilot studies of contaminated soils of Alaska.

Our original project objectives were to: 1) study the impact of temperature on the rheology of Guar gum as a non-Newtonian fluid, 2) study the flow characteristics of Newtonian, non-Newtonian or a combination of both, and 3) compare the effectiveness of Newtonian, non-Newtonian or a combination of both fluids for remediation of contaminants. Our experiments in researching the effects of temperature on rheology required more effort than originally anticipated, due to complete freezing of fluids at subzero temperatures, regardless of concentration. This increased focus resulted in a narrowing of our scope, hence the objective of this research is to study the impact of temperature on the rheology of Guar gum and Xanthan gum as a non-Newtonian fluid.

With an understanding of the changes in rheology with change in temperature, we will pursue funding for future study of the flow characteristics of Newtonian, non-Newtonian or a combination of both fluids under different thermal regimes, and to compare the effectiveness of those fluids for remediation of persistent contaminants.

Methodology

Impact of Temperature on the Rheology of Guar gum and Xanthan gum

Commercial food-grade Guar gum (derived from Cyamopsis Tetragonolobus) and Xanthan gum were used without further purification. Experimental aqueous solutions 0.5g/l, 1g/l, 3g/l, 6g/l and 7g/l concentrations were prepared by dispersing the defined amount (0.5g, 1g, 3g, 6g, and 7g) of Guar gum or Xanthan gum in one liter of distilled water, and stirred at 800 rpm at room temperature. The prepared solutions were blended for two minutes to avoid formation of clumps and kept in the cold chamber for 3 hours to the required temperature. A rheological test was conducted using an OFITE model 900 viscometer to record change in viscosity at different shear rates at a particular temperature. The sample container was wrapped with insulting material to maintain the temperature of solution. Sample temperature was recorded before and after each rheological test. A maximum of 1 °C change was observed during the rheological analysis. Each prepared solution was used within 5 hours to avoid the formation of molds. Figure 1 illustrates the setup of rheological tests.

Guar gum solutions of different concentrations were investigated for viscosity change with increase in shear rate. Figure 2 summarizes the variation of apparent viscosity of Guar gum solution at different temperatures. Moderate (i.e., 3g/l) to high concentrations (i.e., 6g/l and 7g/l)

of Guar gum solutions showed a decreasing trend in viscosity with increase in shear rate (Figures 2c, 2d and 2e). The low concentrations (i.e., 0.5g/l and 1g/l) of Guar gum solutions did not follow the decreasing trend in viscosity with increase in shear rate (Figure 2a and 2b). Rather, the changes in viscosity were very erratic in nature as seen in Figures 2a and 2b.

Low concentrations of Guar gum in water provide a high viscosity solution. When Guar gum is dispersed in water, the galactose side chain of the molecule interacts with water molecules, leading to inter-molecular chain entanglement of the Guar gum in aqueous solutions, rendering viscosity to the solution. With the increase in concentration of Guar gum, the degree of inter-molecular chain interaction or entanglement is enhanced, resulting in increased viscosity (Zhang et al., 2005). Higher concentrations of Guar gum resulted in higher viscosity and at these concentrations of Guar gum in solution, temperature effect on viscosity was found to be insignificant (Figures 2d and 2e).

Figure 3 summarizes the shear stress and shear rate relationship for different concentrations of Guar gum solutions at different temperatures. Linear and power law models were fitted to shear stress and shear rate relationship for Guar gum (Table 1). Moderate (i.e., 3g/l) to high concentrations of Guar gum solution showed the non-linear relationship between shear stress and shear rate (Figure 3 and Table 1), as expected, regardless of temperature. This type of non-linear relationship is associated with non-Newtonian fluids. Hence, moderate to high concentrations showed the expected non-Newtonian behavior at all temperatures.

Low concentration solutions of Guar gum resulted in a linear relationship between shear stress and shear rate (Figure 3 and Table 1). The slope of the linear relationship represents the viscosity of the solutions. This means the viscosity of these solutions would remain constant. Hence, viscosity is independent of the rate of shear. This type of behavior is associated with Newtonian fluids. Thus, 0.5g/l and 1g/l Guar gum solutions behaved as Newtonian fluids at all temperatures.

During the 2017 American Geophysical Union annual meeting, it was recommended to us that adding salt to low concentrations of Guar gum may resolve the issue of erratic changes in viscosity with change in shear rate, as observed in Figures 2a and 2b. Rheological experiments were conducted by adding NaCl (10g/l) or KCl (10g/l) separately to low concentration Guar gum solutions to investigate the effect of salt concentration on viscosity of the polymer solution. Example results of change in viscosity with change in shear rate at two different temperatures are presented in Figure 4. From the limited experiments completed so far, it has been observed that addition of salts to polymer solution decreases the viscosity of polymer solution, compared to the solution without the addition of salt. Reviewing the literature, we found that according to Srichamroen (2007), salts are hydrophilic molecules that strongly interact with water. The addition of higher concentration of salt reduces the availability of water in solution, preventing the expansion of the Guar networks and thereby decreasing the viscosity of the solution. Adding salt also restricts the hydration of Guar gum in solution. Hydration is a key factor to achieve maximum viscosity of the Guar gum solution. While more experiments are being conducted by adding salt to low concentration Guar gum solutions, it was not found to be an effective strategy.

Xanthan gum is a microbial polysaccharide discovered in the 1950s by the U.S. Department of Agriculture. Like Guar gum, low concentrations of Xanthan gum in water provide a high viscosity solution. Xanthan gum shows viscosity synergy with Guar gum. Xanthan gum is stable to acids and alkali and would potentially be effective in working with higher concentrations of contaminants. Figure 5 summarizes the variation in viscosity of different concentrations of Xanthan gum at different temperatures. The decreasing trend in viscosity with increase in shear rate was observed for all concentrations, regardless of temperature. This decreasing trend in viscosity was not observed for low concentrations of Guar gum (Figures 2a and 2b).

Figure 6 summarizes the shear stress and shear rate relationship for Xanthan gum solutions of different concentrations at different temperatures. Linear and power law models were fitted to shear stress and shear rate relationships for Xanthan gum (Table 2). Shear stress and shear rate relationships for low concentration (0.5g/l and 1g/l) Xanthan gum solutions were close to linear (with R^2 from 0.97 to 0.98 for 0.5g/l concentration and, R^2 from 0.96 to 0.98 for 1g/l concentration). For low concentrations, increase in temperature affected the linear fit to experimental data. The value of R^2 was highest (i.e., 0.989 and 0.985 for 0.5g/l and 1g/l, respectively) at 0.6°C and gradually decreased to its lowest value (i.e., 0.97 and 0.96 for 0.5g/l and 1g/l, respectively) at 30.6°C. Thus, linear model fit between shear stress and shear rate was observed to be temperature dependent. In other words, Newtonian behavior of low concentration Xanthan gum solution was observed to be temperature dependent.

Future Considerations

Flow characterization of Newtonian, Non-Newtonian or a combination of both fluids in porous media

Capillary tubes of different diameters and in different ratios will be placed between two perforated discs. Silicon will be filled in spaces between capillary tubes to affix the tubes. A metal holder will be attached to the disc for easy placement and removal. This small cylindrical shape having capillary tubes will be placed in the large cylinder. Fluid will be injected upstream and connection will be made for smooth flow of fluid. The downstream of the cylinder will be attached to the beaker for collection of effluent through the system. A measuring weight balance will be used to record the mass flowing out of the capillary tubes.

The experiment will be conducted for an individual Newtonian fluid, non–Newtonian fluid and a combination of Newtonian and non–Newtonian fluid. The non-Newtonian fluid (Xanthan gum) will be prepared using powder mixed with water and heated to the required temperature. It will then be placed in the insulation material on the upstream of the cylinder, at a higher head. The fluid will flow through the setup to the capillary tube while maintaining constant head in the large cylinder. Xanthan gum flow through the capillary tubes will be collected on the downstream side in the beaker. The mass flow rate will be calculated at input and output. A similar procedure will be deployed for all experiments with each fluid.

The data acquired from the experiment will explain the flow (infiltration) characteristics of non-Newtonian fluid and the mixture of Newtonian and non-Newtonian fluid at different temperatures in different radii pores.

Study of effectiveness of non-Newtonian fluids in soil remediation
A pore-volume of surrogate contaminant will be introduced into the porous media and the setup will be cooled to the desired temperature. Fluid will then be allowed to flow through the media and effluent will be collected. The mass balance of the surrogate contaminant collected as effluent will be used to study the efficiency of remediation using a particular fluid at a certain temperature.

Principal Findings and Significance

Complexities associated with pore structures hinder flow model development for a porous media. Proper understanding of complex pore structures and flow patterns in the media is important. A knowledge of such complexity will provide an opportunity to study and compare the behavior of non-Newtonian fluid and Newtonian fluid under different temperature regimes in the soil. It is critical to understand the impact of temperature on the rheology and flow of Xanthan gum in soil because the adsorption kinetics of each persistent contaminant is different. Once the rheology and flow is well understood, the effectiveness of Xanthan gum in remediation of persistent contaminants can be studied. Key findings from the rheological study experiments are as below.

- For low concentration Xanthan gum solutions, temperature affects the viscosity. At high concentrations, temperature does not affect variation of apparent viscosity with shear rate.
- In terms of viscosity change, Xanthan gum is more insensitive to temperature compared to Guar gum.
- Decreasing viscosity was observed with increase in temperature.
- Guar and Xanthan gum solutions demonstrate Newtonian behavior at low concentrations at all temperatures.
- Guar and Xanthan gum solutions demonstrate Non-Newtonian behavior at moderate to high concentrations, regardless of temperature. The non-Newtonian shear thinning behavior increases with concentration levels.

Products

Naseer, F., O. Awoleke, **D. Misra** and M. Abou Najm, 2017. *Effect of Temperature on Guar Gum Rheology of Different Concentrations*, Paper#H43I-1768, Fall Meeting of the American Geophysical Union, December 11 – 15, New Orleans, LA.

Student Support

Fawad Naseer, M.S graduate student was supported through this fund.

Notable Awards and Achievements

Not applicable.

Tables and Figures

Figures:

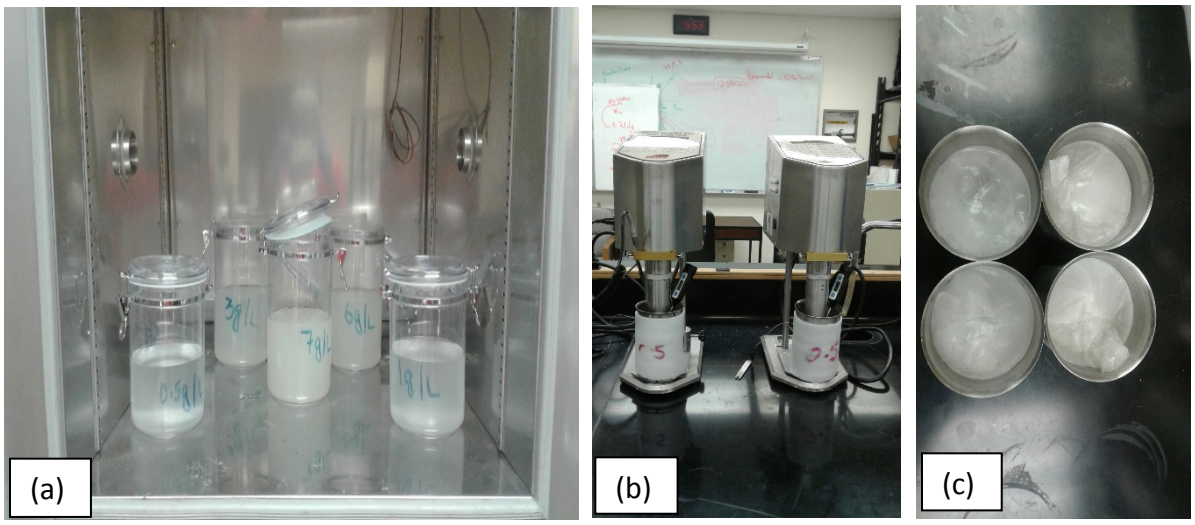

Figure 1. (a) Samples of different concentrations are in Thermotron temperature chamber to attain desired temperature. (b)OFITE Model 900 viscometer used to find the apparent viscosity of Guar gum and Xanthan gum samples. The thermometers are capable of measuring the temperature within 10 seconds. (c) Frozen samples below zero degree Celsius.

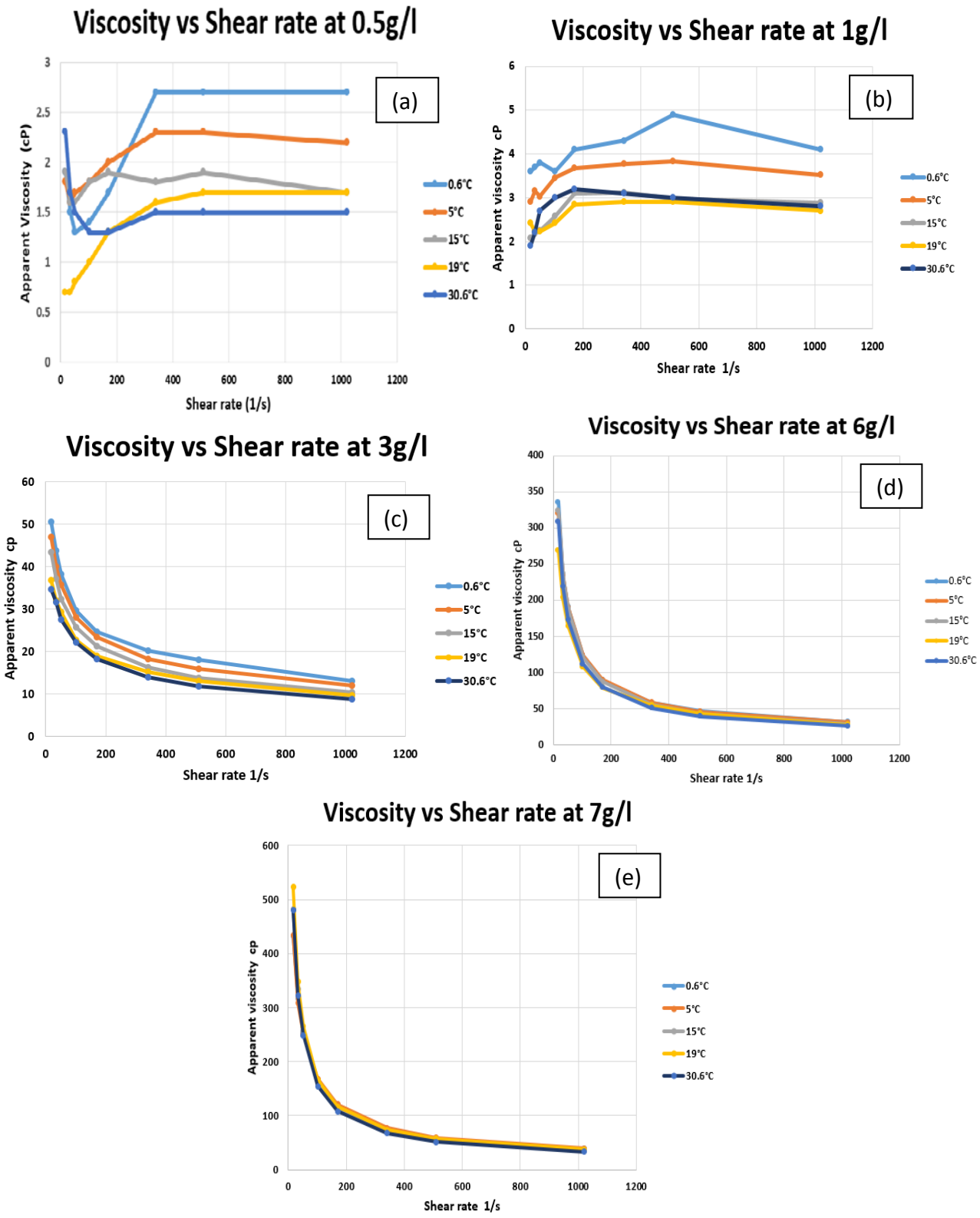

Figure 2. Variation of apparent viscosity of Guar gum solution at different temperatures

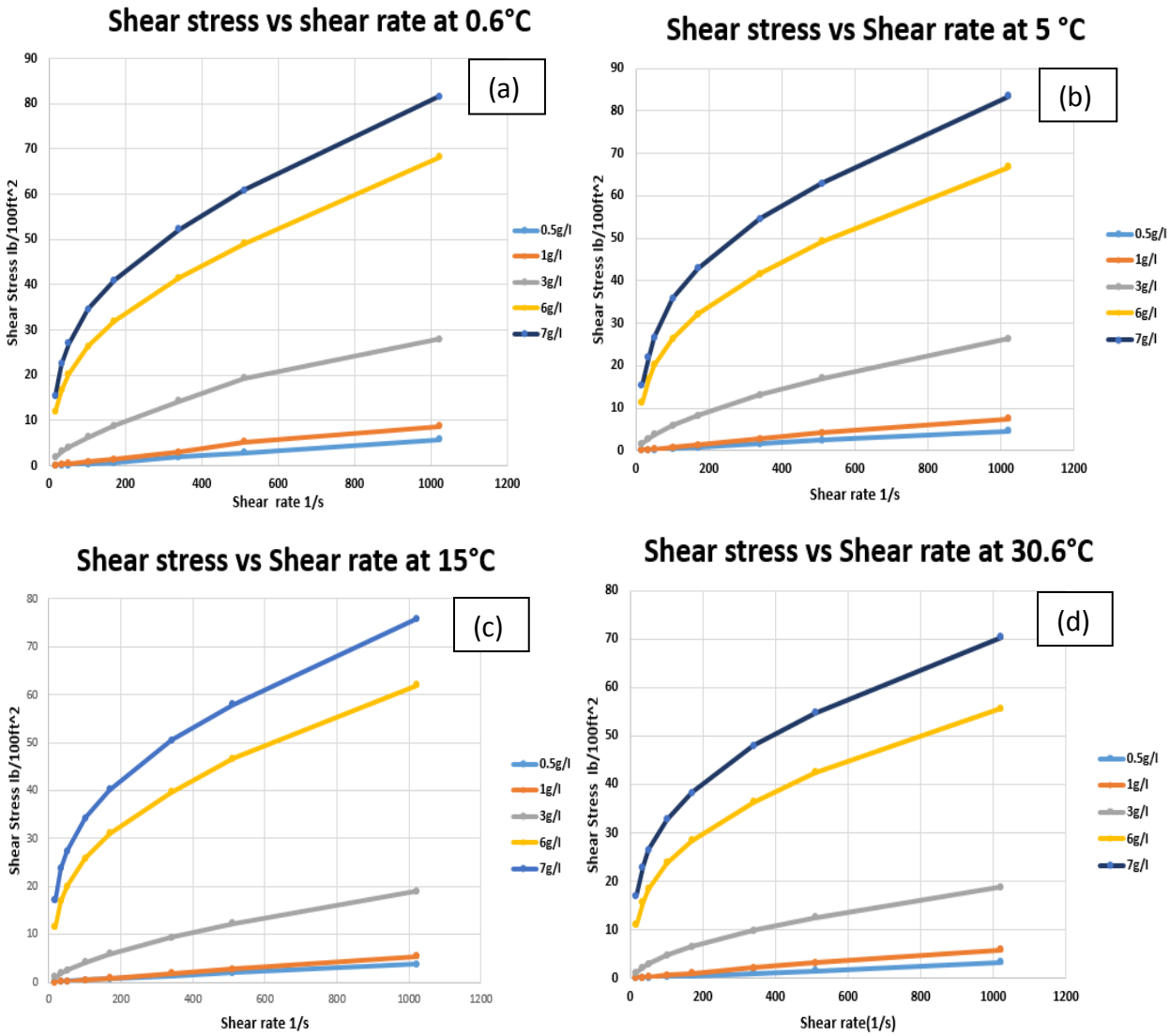

Figure 3. Moderate to high concentrations of Guar gum solution demonstrate shear thinning non-Newtonian behavior. Low concentrations of Guar gum solution demonstrate Newtonian behavior.

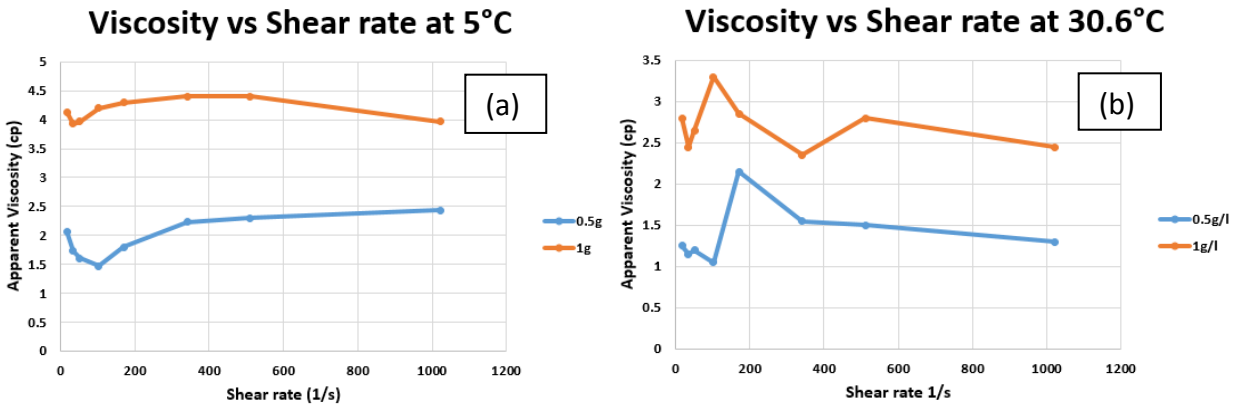

Figure 4. Effect of NaCl (10g/l) on apparent viscosity of low concentration Guar gum solutions.

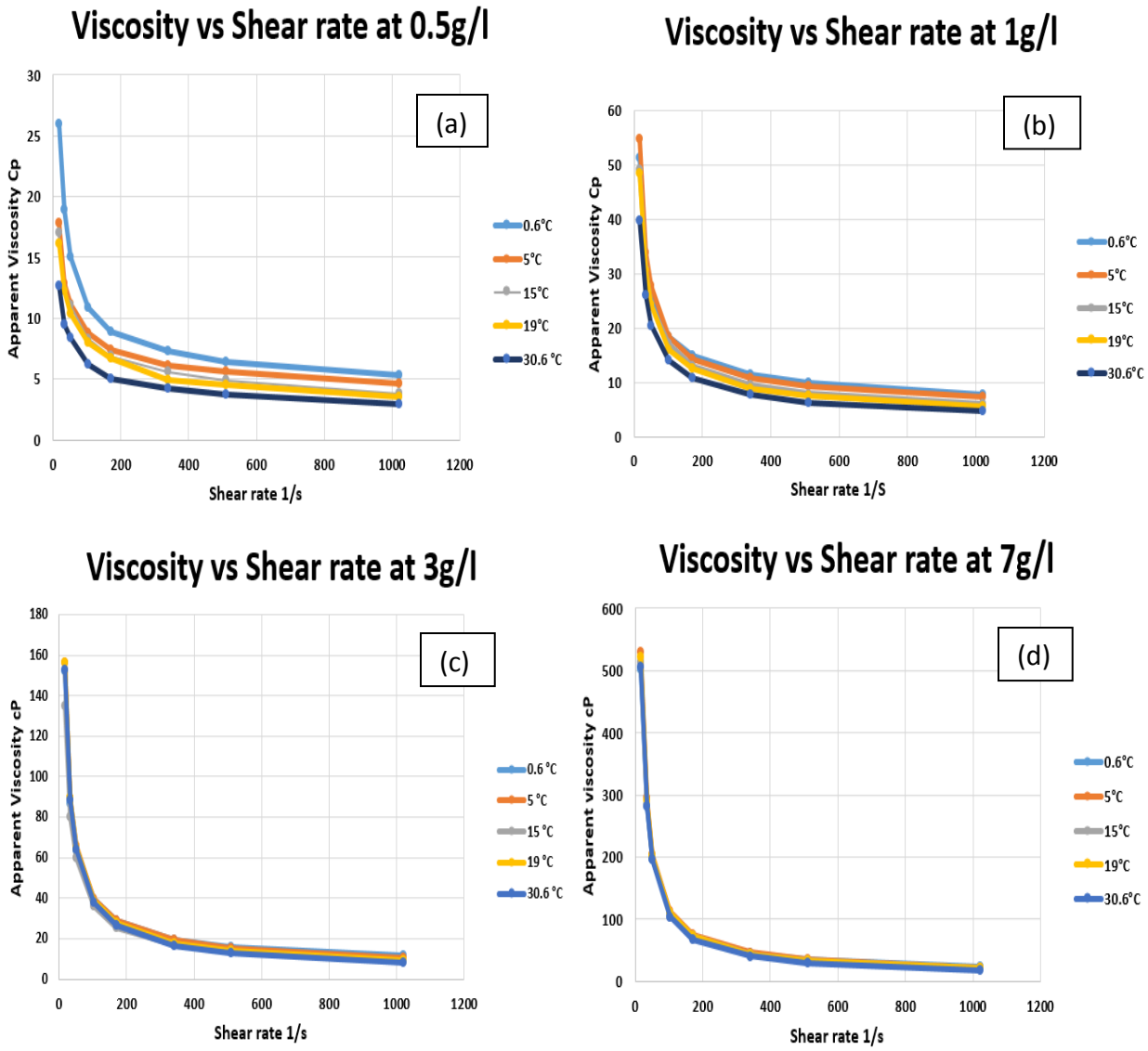

Figure 5. Effect of temperature on Xanthan gum viscosity of different concentration.

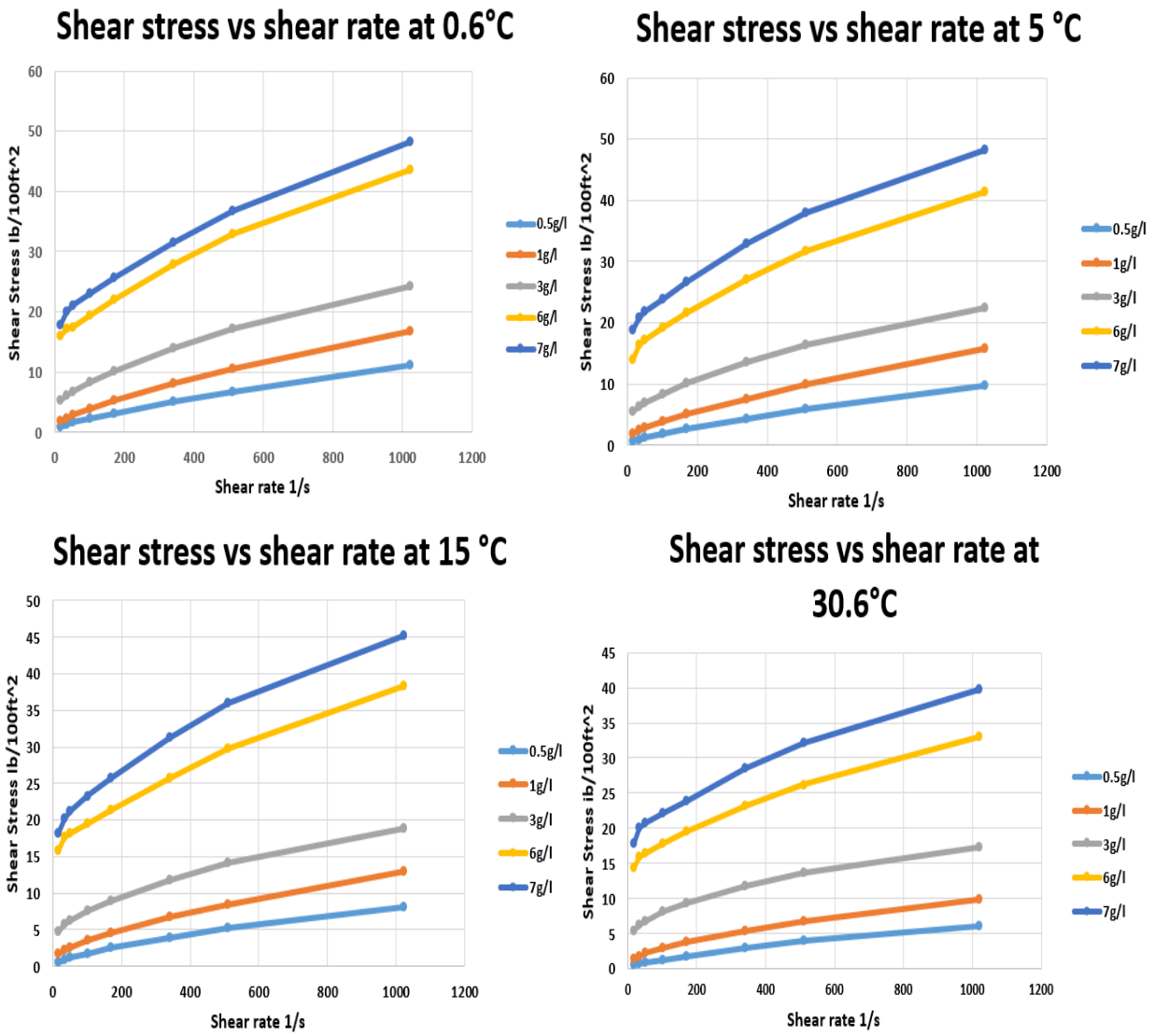

Figure 6. Shear stress and shear rate relationship for Xanthan gum solutions at different temperatures.

Table 1. Linear and Power model curve fitting for Guar gum solutions at different temperatures.

Temperature (Celsius)	Concentrations (g/l)	Equations	R^2
0.6°C	0.5	$y = 0.0059x - 0.1721$	0.996
	1	$y = 0.0088x + 0.0151$	0.9907
	3	$y = 0.2842x^{0.6699}$	0.9985
	6	$y = 3.8393x^{0.4125}$	0.9977
	7	$y = 5.5126x^{0.3893}$	0.9935
5°C	0.5	$y = 0.0047x - 0.0976$	0.9982
	1	$y = 0.0075x + 0.0193$	0.9975
	3	$y = 0.273x^{0.661}$	0.9986
	6	$y = 5.0011x^{0.3868}$	0.9977
	7	$y = 11.085x^{0.3054}$	0.9946
15°C	0.5	$y = 0.0061x - 0.0093$	0.9985
	1	$y = 0.0061x - 0.0093$	0.9985
	3	$y = 0.2659x^{0.6442}$	0.9979
	6	$y = 5.0088x^{0.3734}$	0.9978
	7	$y = 7.7237x^{0.3346}$	0.998
19°C	0.5	$y = 0.0036x - 0.0936$	0.9986
	1	$y = 0.0057x - 0.0085$	0.9978
	3	$y = 0.2135x^{0.6666}$	0.9976
	6	$y = 4.405x^{0.385}$	0.9977
	7	$y = 9.0458x^{0.3185}$	0.999
30.6°C	0.5	$y = 0.0032x - 0.0119$	0.9982
	1	$y = 0.0058x + 0.0592$	0.9972
	3	$y = 0.2068x^{0.6613}$	0.9954
	6	$y = 3.9294x^{0.3837}$	0.9969
	7	$y = 6.8665x^{0.3353}$	0.9976

Table 2. Linear and Power model curve fitting for Xanthan gum solutions at different temperatures.

Temperature (Celsius)	Concentrations (g/l)	Equations	R^2
0.6°C	0.5	$y = 0.0102x + 1.186$	0.9893
	1	$y = 0.0148x + 2.2764$	0.9858
	3	$y = 1.6625x^{0.3706}$	0.9743
	6	$y = 7.009x^{0.2443}$	0.9255
	7	$y = 8.4501x^{0.2346}$	0.9509
5°C	0.5	$y = 0.0072x + 0.8468$	0.9824
	1	$y = 0.0112x + 2.0457$	0.9808
	3	$y = 1.8792x^{0.3467}$	0.9756
	6	$y = 6.4653x^{0.2549}$	0.9535
	7	$y = 8.9138x^{0.2306}$	0.9474
15°C	0.5	$y = 0.0066x + 0.8252$	0.981
	1	$y = 0.009x + 1.9632$	0.9742
	3	$y = 1.9895x^{0.3258}$	0.9793
	6	$y = 7.5214x^{0.2233}$	0.9521
	7	$y = 9.3121x^{0.2151}$	0.9565
19°C	0.5	$y = 0.0058x + 0.8725$	0.9765
	1	$y = 0.0082x + 1.7383$	0.9712
	3	$y = 2.0528x^{0.3144}$	0.9818
	6	$y = 7.6034x^{0.2174}$	0.9516
	7	$y = 9.5639x^{0.2107}$	0.9659
30.6°C	0.5	$y = 0.0056x + 0.7107$	0.9776
	1	$y = 0.0083x + 1.9407$	0.9687
	3	$y = 2.2729x^{0.2852}$	0.9898
	6	$y = 7.7484x^{0.1949}$	0.951
	7	$y = 10.028x^{0.1855}$	0.95

References

Abou Najm M.R., and Atallah, N.M., 2016. Non-Newtonian Fluids in action: Revisiting the hydraulic conductivity and pore size distribution of Porous Media, Vadose Zone Journal, v.15, i.9, p. 1-15.

Balhoff, M.T., and K.E. Thompson. 2006. A macroscopic model for shear thinning flow in packed beds based on network modeling. Chem. Eng. Sci. 61(2):698-719. doi:10.1016/j.ces.2005.04.030.

Barnes, D.L., W. Rhodes, S. Frutiger, R. Ranft. 2007. Persistence of Herbicides in a Subarctic Environment. In proceedings of the 8th International Symposium on Cold Regions Development, Tampere, Finland, September 25-27.

Blokker, N., 2014. Analysis of Alginate-Like Exopolysaccharides for the Application in Enhanced Oil Recovery. Master Thesis, Delft University of Technology, Delft, The Netherlands, 18 September 2014.

Chhabra, R.P., and Richardson J.F., 1999. Non-Newtonian Flow in the Process Industries: Fundamentals and Engineering applications. Butterworth-Heinemann, MA, 421pp.

Cross, M.M., 1965. Rheology of non-Newtonian fluids- A new flow equation for pseudo plastic systems, J. Colloid. Sci., 20(5), p. 417-437.

Currie, I.G., 1993. Fundamental Mechanics of Fluids, Third Edition, Mercel Dekker, Inc. NY, USA, 525pp.

Di Federico, V., Pinelli, M., and Ugarelli, R., 2010. Estimates of Effective Permeability for non-Newtonian Fluid Flow in Randomly Heterogeneous Porous Media, Stoch Envirn Res Risk Assess, 24: 1067-1076.

Gittings, M.R.,Cipelletti, L.,Trappe,V.,Weitz,D.A.,In., and Lal,J., 2001.The effect of solvent and ions on the structure and rheological properties of guar solutions.

Hendrickx, J.M.H., and M. Flury. 2001. Uniform and preferential ñow, mechanisms in the vadose zone. In: Conceptual models of flow and transport in the fractured vadose zone. National Research Council, National Academy Press, Washington, DC. p. 149-187.

Hove, K.; Pedersen, O.; Garmo, T.H.; Hansen, H.S.; Staaland, H. Fungi, 1990. A major source of radiocesium contamination of grazing ruminants in Norway. Health Phys., 59, 189-192.

Jung, J, Jang, J, and Ahn, J, 2016. Characterization of a Polyacrylamide Solution Used for Remediation of Petroleum Contaminated Soils, Materials, 9, 16: 1-13.

Lake, P.S., 2008. Flow-Generated disturbances and Ecological Responses: Floods and Droughts. In Hydroecology and Ecohydrology: Past, Present and Future; Wiley Press: New York, NY, USA; pp. 75-92.

Pollock, T.J.; Thorne, L.; Yamazaki, M.; Mikolajczak, M.J.; Armentrout, R.W., 1994. Mechanism of bacitracin resistance in gram-negative bacteria that synthesize exopolysaccharides. J. Bacteriol., 176, 6229-6237.

Sorbie, K., 1991. Polymer-Improved Oil Recovery; Springer Science+Business Media: Berlin, Germany, 1991; Chapter 1; pp. 1-5.

Srichamroen, A., (2007).Influence of Temperature and salt on viscosity property of guar gum. Naresuan University Journal 15(2)55-62.

Meuser, H., 2010. Contaminated Urban Soils; Springer Science & Business Media: Berlin/Heidelberg, Germany; Volume 18.

Palaniappan, M., Gleick, P.H., Allen, L., Cohen, M.J., Christian-Smith, J., and Smith, C., 2010. Clearing the Waters: A Focus on Water Quality Solutions, United Nations Environmental Programme Publication, Nairobi, Kenya, pp. 89.

Robertson, A.M., 2005. Lecture Notes on Non-Newtonian Fluids Part I: Inelastic Fluids, Department of Mechanical Engineering, University of Pittsburgh. Accessed on November 8, 2016, http://numerik.iwr.uni-heidelberg.de/Oberwolfach-Seminar/Robertson_NonNewtonianNotes.pdf

Velimirovic, M., Tosco, T., Uyttebroek, M., Luna, M., Gastone, F., De Boer, C., Klaas, N., Sapion, H., Eisenmann, H., Lassson, P., Braun, J., Sethi, R., and Bastiaens, L., 2014. Field Assessment of Guar Gum Stabilized Microscale Zerovalent Iron Particles for In-situ Remediation of 1,1,1-Trichloroethane, Journal of Contaminant Hydrology, 164: 88-99.

Zhang, L. M., Zhou, J. F., & Hui, P. S. (2005). A comparative study on viscosity behavior of water-soluble chemically modified guar gum derivatives with different functional Lateral groups. *Journal of the Science of Food and Agriculture*, *85*, 2638-2644.

Variable lapse rates and the mass balance of a well-studied glacier in south-central Alaska: Confirmation and extension

Basic Information

Title:	Variable lapse rates and the mass balance of a well-studied glacier in south-central Alaska: Confirmation and extension
Project Number:	2017AK137B
Start Date:	3/1/2017
End Date:	2/28/2018
Funding Source:	104B
Congressional District:	AK-001
Research Category:	Climate and Hydrologic Processes
Focus Categories:	Water Quantity, Water Supply, Climatological Processes
Descriptors:	None
Principal Investigators:	Roman Dial, Jason Geck

Publication

1. Ganey, G.Q., M.G. Loso, A.B. Burgess, and R.J. Dial, R.J, 2017, The role of microbes in snowmelt and radiative forcing on a large Alaskan icefield. Nature Geoscience, 10:754-759.

1. Project Title

Variable lapse rates and the mass balance of a well-studied glacier in south-central Alaska: Confirmation and extension

2. Principal Investigators

(1) Roman J. Dial, Professor of Mathematics and Biology, Alaska Pacific University, roman@alaskapacific.edu, 907-564-8296. (2) Jason E. Geck, Assistant Professor of Earth Science, Alaska Pacific University, jgeck@alaskapacific.edu, 907-564-8309

3. Abstract

Modeling snowmelt is important for water management and resource planning in northern and mountainous regions. Distributed melt models apply variations on degree-day models that are spatially distributed, generally using constant environmental lapse rates (the relationship between elevation and temperature) to extend weather station data beyond the locale where it is collected. We show that on Eklutna Glacier, a source of drinking water and hydropower for Anchorage, Alaska, lapse rates are not only highly variable, but often inverted during the melt season. We installed three weather stations in the accumulation basin of Eklutna, from 1375 to 1500 meters above sea level, to collect temperatures and melt rates. Temperature sensors in so-called mechanically aspirated shields and naturally aspirated shields logged temperature data hourly while photographing ablation stakes four times daily. Melt rates and temperatures were regressed on elevation to estimate daily lapse rates. We found that temperatures were inverted well over half the melt season; melt rates were also inverted about one-third of the melt season, with equal or greater melt at higher elevations. There was no correlation between melt lapse and temperature lapse. We investigated local weather variables and HYSPLIT modeled air movement. While inversions were more likely during high temperatures and high pressure, they were less likely when windy. We found that the odds of melt inversions were not related to any weather or air movement variables we measured. Our results may explain, in part, why models of melt in Alaska, including WASIM and DTIMM applied to Eklutna and a recent basin-wide comparison of discharge into the Gulf of Alaska, consistently underestimate discharge: there is more melt observed than expected because the melt models apply a constant lapse rate that is never inverted.

4. Problem/Motivation and Research Objectives

Snow-covered landscapes provide freshwater through snowmelt to natural and human communities. Understanding and predicting the volume of discharge due to snow and ice run-off is important in a world of growing populations, dwindling resources, and warming temperatures. Ice and snow melt modelling with temperature-index models, such as variations of the degree-day model (DDM), are convenient and simple, often applied using as few as a single temperature station to estimate melt across a highly variable mountain landscape. DDMs sum daily temperatures above zero Celsius, or positive degree days, and apply a degree-day factor (melt per degree day) to estimate or predict snow or ice melt, an idea that is quite old and established (Martins, 1842). Spatially distributed melt models apply constant, negative temperature lapse, either environmental lapse rate or free-air moist adiabatic lapse rate. The moist adiabatic lapse

rate, a troposphere average of -6.5 °C km^{-1}, describes how much freely moving air cools as it rises (Barry & Chorley, 2009). Studies of surficial, or *environmental*, lapse rates that describe the cooling temperatures of non-rising air with topographic elevation, find that these lapse rates vary over time and space (Gardner et al., 2009; Gardner & Sharp, 2009; Minder et al., 2010; Petersen & Pellicciotti, 2011). The use of constant lapse rates will likely bias estimates of melt from DDMs, and will seriously underestimate melt if lapse rates are inverted—i.e., temperature increases with elevation–during the melt season (Minder et al., 2010). For example, Beamer et al. (2016) recently compared a suite of melt-based snow melt models that relied on lapse rates to mass balance estimates from NASA's Gravity Recovery and Climate Experiment (GRACE). While GRACE, too, has limitations affecting accuracy (Velicogna & Wahr, 2013), Beamer et al.'s best model underestimated discharge into the Gulf of Alaska. It is becoming increasingly clear that distributed models need accurate parameters to produce accurate discharge.

In this study we examine temperature and melt inversions at Eklutna Glacier in Southcentral Alaska (Figure 1). Previous work has documented both temperature inversions (Ganey, 2015) and melt inversions (Dethlefs, 2012; Ganey 2015), where melt is greater at higher elevations, on the Kenai Peninsula's Harding Icefield, a pattern consistent with long-term thinning on the Harding Icefield (VanLooy et al., 2006). Similarly, a report previous to this one (Dial, 2017) documented frequent, deep, and persistent temperature inversions on Eklutna Glacier in 2016, a pattern consistent with so-called "anomolous thinning" (Sass, 2012). Here, we examine both 2016 and 2017 melt season inversions, as well as possible weather variables related to the presence of inversions.

5. Methodology

We collected data for surface lowering, temperature, and weather variables from Eklutna Glacier's accumulation basin (> 1300 meters above sea level) during the 2016 and 2017 melt seasons. We used daily averaged temperature and melt data to calculate the relationship between these variables and elevation using three locations (Table 1) from 1375 to 1500 meters above sea level (m asl), and used the relationship to identify inverted and non-inverted lapse rate for both melt and temperature on a daily scale. Logistic regressions were performed to identify potential relationships of weather variables to inversions. We also performed graphical comparison of air movement during inversions and non-inverted days to investigate potential advection of warm and moist air from Gulf of Alaska air masses onto the glacier.

5.1 Study site

At the far western end of the extensive complex of glaciers in the Chugach Mountains of southcentral Alaska, Eklutna Glacier is located in a coastal climate division with a maritime seasonal temperature range (Bieniek et al., 2012). The glacier is roughly 50 km from Anchorage, covering 29.5 km^2 across an elevation range of 580 to 2100 m asl (Sass et al., 2017). Eklutna Glacier is a source for up to 90% of Anchorage's municipal water and 2 to 3% of its municipal electricity (Sass et al., 2017). Previous studies on Eklutna Glacier include mass balance and thinning (Sass et al., 2017), runoff (Brabets, 1993), flow dynamics (Sass et al., 2009), ice worms (Dial et al., 2012), and the role of snow algae in snowmelt (Ganey et al., 2017).

5.2 Weather Measurements

We established three weather stations (ELA, MID, and ACC; Figure 1) at varying elevations (Table 1) in the Eklutna Glacier accumulation zone to measure temperature and melt over the 2016 and 2017 melt seasons. One of these stations (ELA: elevation 1375 m asl) recorded weather variables, including precipitation, relative humidity, wind-speed, and wind direction in 2016 and 2017. Broadband albedo, as the ratio of outgoing to incoming radiation, was also measured in 2016. Weather sensors were installed on floating tripods of our own design on the glacial surface (Figure 2a). Helicopter and foot travel were used for access.

Temperatures -- Data loggers (Campbell scientific, model CS215) recorded mean hourly temperatures 2 m above the snow surface from 15 May to 11 September 2016 at each site. Each temperature sensor was equipped with a radiation shield (Apogee TS-100, naturally-aspirated). In 2017, additional data loggers recorded temperatures with Apogee TS-100 mechanically-aspirated radiation shields from 6 July to 8 September for comparison to naturally aspirated radiation shields, allowing a test of the two methods. Henceforth, temperatures will be specified as 'mechanically-aspirated' when referring to temperatures measured with a mechanically aspirated shield.

Melt rates -- We monitored surface lowering as a proxy for melt using ablation stakes and interval photography. Stakes were installed at sites MID (elevation: 1450 m asl) and ACC (elevation: 1505 m asl) and marked with black electrical tape every 10 cm (Figure 2b). Exposed heights of stakes were captured using Wingscapes Timelapse Cameras (SKU: WCT-00122) set to automatically record every 6 h (Figure 2b). Ablation stake heights during 2016 were estimated from photographs at a precision of 5 cm and during 2017 at a precision of 2 cm.

Automated weather station -- An automated weather station (AWS; Figure 2a) at ELA recorded relative humidity, broadband albedo, precipitation, and surface lowering measurements using a sonic ranger (SR50-L Ultrasonic Distance Sensor, accuracy ±1 cm). The ranger measured hourly snow surface lowering from 15 May to 11 September 2016 and 6 May to 8 September 2017. In 2017, the sonic ranger tipped towards the ground around 19 July until manually righted 31 August. This tipping likely affected albedo and radiation measurements, so they are not presented here. A time-lapse video captured the ELA using a Brinno TLC200 Time Lapse HD Video Camera. Site ELA also included an anemometer recording hourly wind speed and direction. Wind directions at ELA during 2016 were suspect beginning 15 June and are not presented here. A barometer (Onset, model U20L) was installed near the glacier at ground level along the West Fork of Eklutna River (Figure 1) and measured absolute pressure on an hourly basis.

Cloud Cover -- We visually evaluated cloud cover during 2017 with photographs from ELA, MID, and ACC using a simple 0–100% scale based on standard 0–1 classifications (Table 2) and adapted from NASA Earth Observer (www.globe.gov). The ELA site camera faced south, the MID camera faced northeast, and the ACC camera faced north (Figure 2b).

5.3 Statistical analysis

Statistics were performed in R (version 3.4.0). Ablation stake heights were converted to daily surface lowering (melt in cm d^{-1}). These melt values, as well as hourly temperature values, were averaged over day of year as daily means, resulting in cm day^{-1} and °C. Temperatures and melt are generally assumed to decrease with increasing elevation. The slopes of the relationships between melt and elevation (e.g., cm d^{-1} km^{-1}) and temperature and elevation (e.g., °C km^{-1}) are referred to as "surface lapse rates." An "inversion" in this assumed negative relationship means there is no relationship with elevation or an increase in melt and/or temperature with increasing elevation. That is, if L signifies surface lapse of either melt rate or temperature, then $L < 0$ is non-inverted (i.e., normal) and $L \geq 0$ is inverted. Surface lapses for both temperature and melt (here referred to as simply "lapse") were calculated from daily means over elevations (in meters) through simple linear regression: $Y = a + LE$, where Y is daily melt (in cm d^{-1}) or mean daily temperature (°C d^{-1}), L is lapse rate, and E is elevation (in km). Lapse rates are thus presented as cm km^{-1} for melt lapse and °C km^{-1} for temperature lapse. Regressions were calculated on a daily basis using all three sites: ELA, MID, and ACC. For 2016 this resulted in 76 days during the melt season (DOY 136–211 or 15 May–29 July) and 52 days for 2017 (DOY188–239 or 7 July–27 August). We used logistic regression to investigate the probability, P, that a day's lapse was inverted given available daily weather variables, x_i, where $i = 1,\ldots,n$ are the n available weather variables and $\text{logit}(P) = \ln(P/(1-P)) = \beta_0 + \beta_i x_i$, or $P = \exp(\beta_0 + \beta_i x_i)(1+ \exp(\beta_0 + \beta_i x_i))^{-1}$. We used the Wald-test significance (p-values < 0.05) of the regression coefficients, β_i, in these logistic regressions to identify variables that may have a relationship with inversions in melt or temperature. Each weather variable was first used in multiple logistic regression with year as an additional covariate, both as an addition and an interaction, and then used in simple logistic regression for a given year, if there was a significant year effect detected in the multiple regression. We applied the standard Bonferroni correction to the significance level of $p = 0.05$, given the large number of regressions.

5.4 HYSPLIT modelling

We evaluated the possibility of air mass advection being related to inversions by modelling air trajectories using the Hybrid Single-Particle Lagrangian Integrated Trajectory (HYSPLIT) model of the NOAA Air Resources Laboratory (Stein et al., 2015; Rolph et al., 2017). Single trajectories were run once each day of measured lapse rates in 2017, giving 52 total trajectories. Model parameters involved North American Regional Analysis (NARR) 32 km meteorology, single level at 1600 m asl. Trajectories were run backwards for 48 hours, ending 0300 UTC at the destination, that is, ELA, converted to UTM coordinates using ArcMap version 10.3.1 (ESRI), then calculated as mean trajectory using circular statistics. Mean HYSPLIT trajectories and ELA hourly wind-speed and direction were then classified into inverted or non-inverted days for both temperature and melt lapse, after adding 180° to HYSPLIT so HYSPLIT trajectory and wind direction shared a directional scheme.

6. Principal Findings and Significance

Melt and temperature recorded at three stations on the Eklutna Glacier above the equilibrium line altitude (ELA) showed that both temperature lapse and melt lapse rates were highly variable and often inverted, but uncorrelated with each other during the 2016 and 2017 melt seasons.

Temperature lapse rates measured with mechanically-aspirated radiation shields were inverted slightly more frequently than temperatures measured with naturally-aspirated radiation shields, but both were strongly correlated with each other. Using simple logistic regression we explored possible relationships between weather variables and the presence of lapse inversions, including modeled air movement using HYSPLIT.

6.1 Temperature inversions

Temperature lapse rates were more often inverted than not inverted during the 2016 and 2017 melt seasons (Figure 3). Mean temperature lapse rates were positive in both 2016 (naturally aspirated: $L = 4.0\ °C\ km^{-1}$) and 2017 (naturally aspirated: $L = 7.2\ °C\ km^{-1}$; mechanically aspirated $L = 5.6\ °C\ km^{-1}$). Temperature lapse was inverted during much of the melt season for both years (Figure 4), with both mechanically-aspirated and naturally-aspirated shielded temperature sensors. Of 76 consecutive days in 2016, temperature lapse rate was inverted well over half the time (58% or 44 days). Similar results held in 2017 when both mechanically-aspirated and naturally-aspirated radiation shields were installed. Of consecutive 52 days in 2017, daily temperature lapse calculated with naturally-aspirated shields were inverted over 70% of the time (71% or 37 days) and non-inverted nearly 30% of the time (29% or 15 days). Using mechanically-aspirated shields indicated even more frequent inversions. Out of a total of 52 days of consecutive data, mechanically-aspirated temperature results were inverted nearly 80% of the days (79% or 41 days) and non-inverted around 20% of the time (21% or 11 days). Even though naturally-aspirated and mechanically-aspirated temperatures in 2017 were very similar (Figure 5), mechanically-aspirated temperature lapse rates were inverted about 10% more often.

6.2 Melt Inversions

Melt lapse rates (calculated as the slope of daily melt regressed on elevation) were inverted over 30% of the melt season in both years (Figure 3), meaning that about one day out of three snow melted more at higher than lower elevations in the accumulation basin. Mean values of melt lapse (Figure 4) were negative in both years, but much more negative in 2016 ($-20\ cm\ km^{-1}$) than 2017 ($-6\ cm\ km^{-1}$). Percentage of melt season when daily melt rates were inverted was very similar between years. Out of 76 consecutive sample days in 2016, melt lapse rates were inverted 32% of the time (24 days). Of 52 consecutive sample days in 2017, melt lapse was inverted 35% of the time (18 days).

6.3 Independence of Melt and Temperature Lapse Rates

While both melt and temperature lapse rates were often inverted, we detected no correlation ($r \leq 0.02$) between daily melt lapse and temperature lapse rates in either year (Figure 6). Time series of temperature (including mechanically-aspirated) and melt for both years revealed that temperature and melt lapse rates were often out of phase (Figure 5), and melt lapse did not appear to lag temperature lapse, but instead to be independent of temperature. Temperature lapse was inverted almost 30% more often than melt lapse in 2016, and 40% more often in 2017. Temperature lapse using a mechanically-aspirated shield was inverted nearly 45% more often than melt lapse rate. The lack of correlation between daily temperature and melt lapse rates in both years is consistent with the independence of temperature and melt on a daily scale. The

correlation between daily temperature and melt lapse rates (Figure 6) was essentially zero in 2016 ($r = 0.01$, $p = 0.90$) and 2017 ($r = 0.02$, $p = 0.86$).

6.4 Covariates of Inversions

Logistic regression on combined 2016 and 2017 data with year as an interaction term added little support at a Bonferroni level of significance ($p < 0.004$) for any weather variables as causative for inversions, other than warm temperatures increased the probability of temperature inversions. For logistic regressions of the presence of temperature inversions on individual weather variables (Table 3) and their interaction with year, no interactions were significant, while three weather variables, all related to temperature, revealed year as an additive term and were also significant (Bonferroni corrected $p < 0.004$) covariates: ELA max temperature ($p = 0.001$), MID max temperature ($p < 0.001$), and ACC max temperature ($p < 0.001$). Each of these three covariates increased the odds of temperature inversions.

Other covariates significant at $0.004 < p < 0.05$ (Table 3) included increasing cloud cover, which reduced probability of temperature inversions; increasing ELA max windspeed in 2017, which also reduced probability of temperature inversions; and increasing absolute pressure, which increased the probability of temperature inversions.

Of seven qualitatively different measures of weather (temperature, precipitation, humidity, pressure, local wind, regional air movement, and solar radiation) only two (temperatures and wind speed) predicted temperature inversions in 2016 (Table 4) at the Bonferroni level of significance ($p < 0.004$). The significance of temperatures for predicting the probability of temperature inversions was higher ($p < 0.004$) than that of incoming radiation and albedo, which were significant at a less restrictive level ($0.004 < p < 0.05$).

Several weather variables significantly predicted temperature inversions in 2017, although we had no radiation data for that year. The presence of temperature inversions was significantly related to temperatures and max windspeed at the Bonferroni correction level of 0.004, while absolute pressure and cloud cover were significant at the 0.05 level (Table 5). A rise in all temperatures and a rise in absolute pressure increased the probability of inversion. A decrease in ELA max windspeed and mean total cloud cover also increased this probability. Using mechanically-aspirated temperatures, the same results held with the exception of cloud cover, which was not significant (Table 5).

At the Bonferroni corrected or uncorrected level of significance, no weather variable significantly predicted melt inversions in either 2016 or 2017 (Table 6). Only two variables demonstrated $p < 0.5$ in either year. In 2016, an increase in albedo (which was not measured in 2017) was positively associated with melt inversions ($p = 0.15$) and in 2017 relative humidity was nearly significant at the 0.05 level ($p = 0.06$).

Pairwise correlation among all available weather variables (Table 7) against each other revealed that correlations above $r = 0.50$ happened mostly between different summary statistics of daily temperatures at different stations. There were only four pairs of variables with $r > 0.50$ that were not between daily temperature summary statistics. These included ACC melt vs. melt lapse ($r =$

0.79), ELA daily melt vs. ELA mean daily temperature (r = 0.52), ELA daily melt vs. daily mean of all stations (r = 0.51), and ELA daily melt vs. MID mean daily temperature (r = 0.50).

6.5 HYSPLIT Trajectories and Wind Direction

Measured hourly ELA wind direction (Figure 7) and modeled HYSPLIT trajectories (Figure 8) were similar, showing no differences between inverted and non-inverted days for either daily temperature or melt lapse rates. Average trajectory and hourly wind directions on inverted days mostly kept to the southeast for both temperature and melt, with similar results on non-inverted days. Wind speeds on inverted and non-inverted days had nearly identical ranges, around 0 – 4.6 m sec-1 (Figure 7). HYSPLIT mean trajectory and ELA hourly wind directions were very similar overall (Figures 7 and 8) suggesting that southeast winds were generally dominant within this study period.

6.6 Significance

The daily estimated temperature and melt lapse rates reported here indicate that both vary substantially and are often inverted during the melt season in the accumulation zone of southcentral Alaska's Eklutna Glacier. Moreover, the two lapse rates are uncorrelated on a daily basis. Temperature-index models, like the degree-day-sum model (e.g., Beamer et al., 2016) use elevation and temperatures as input to model melt spatially. Temperature-index models are sensitive to choice of lapse rates, yet most apply a constant negative (– 6.5 °C km^{-1}) environmental lapse rate (the rate of cooling above a topographic surface for unmoving air), which is generally motivated by the moist adiabatic lapse rate, the rate of cooling for moist, free-rising air (Minder et al., 2010; Hodgkins et al., 2012). Our findings demonstrate highly variable temperature lapse rates that are often inverted in the accumulation zone of an Alaskan glacier, supporting other calls to incorporating this variability when modeling melt (Rolland, 2003; Gardner et al., 2009; Minder et al., 2010; Petersen et al., 2011; Hodgkins et al., 2012; Petersen et al., 2013). Because Eklutna Glacier loses most mass from above the ELA in its upper basin of its main branch (Sass et al., 2017), the inversions described here imply that any distributed melt models using constant and negative lapse rates will underestimate melt in the accumulation zone, underestimate downstream discharge, and overestimate glacier mass balance.

Naturally vs. Mechanically-Aspirated Shields. The close similarity of 2017 naturally-aspirated and mechanically-aspirated temperatures give confidence to the naturally-aspirated data from 2016, previously reported with additional accumulation basin temperatures on both the Eklutna and nearby Whiteout Glaciers. These additional sites showed similar results as shown here: frequent, deep and long lasting inversions (Dial and Geck, NWIR 2017 report). In addition, mechanically-aspirated shields demonstrated even more frequent temperature inversions than naturally-aspirated shields. This suggests that 2016 results may be even more inverted than documented here. These temperature results, which are mostly inverted overall, illustrate the potential value of including variable temperature lapse rates in melt modelling.

Possible Causes of Melt Season Temperature Inversions. Both 2016 and 2017 mean temperature lapse rates were positive, while mean melt lapse rates were negative (Figure 3). The 2016 mean lapse rate is roughly seasonal, from 15 May to 29 July, and equals 3.99 °C km^{-1}. This number is similar in magnitude *but opposite in sign* to previously found summer rates in the

Canadian Arctic of -4.1 °C km^{-1} (Marshall et al., 2006) and -4.9 °C km^{-1} (Gardner et al., 2009). Mean temperature lapse in 2017 on Eklutna Glacier was even higher (+7.2 °C km^{-1}), while the mechanically-aspirated 2017 lapse (+5.62 °C km^{-1}) was between the two. Conversely, mean melt lapse rates in both years were negative, and substantial in 2016 (-19.87 cm km^{-1}), which furthers the notion of de-coupling between temperature and melt on daily scales.

Few weather variables were significantly related to temperature inversions. Weather variables vary spatially in mountain climates and are important for glacial studies (Rolland, 2003). In 2016, probability of temperature inversion increased as temperatures and incoming radiation increased and albedo decreased (Table 4). Albedo is important in modelling glacial melt–lower albedo coincides with exposure of dark areas, which have less reflectivity and therefore melt more. Albedo depends on the nature of the glacial surface, for example, glacial ice has lower albedo than snow (Hock et al., 2005). Albedo links temperatures with incoming radiation; however, it is difficult to say how these are related to increased temperature inversions. In 2017, the probability of temperature inversion increased as temperatures and absolute pressure increased, and ELA max windspeed and mean total cloud cover decreased (Table 5). The idea that strongest daily lapse rate cycles happen when there is weak wind and lack of cloud cover has been documented previously (Lesins et al., 2010; Pike et al., 2013b). Increased cloud cover usually coincides with cooler temperatures, storms and strong winds, meaning a mechanical breakup of inversions. Gulf of Alaska glaciers are strongly linked to mean summer air temperatures (Arendt et al., 2013). Warm temperatures and higher humidity tend to be associated with coastal sea air, possibly passing over the ocean or bodies of water. However the HYSPLIT model trajectories and local wind directions failed to reveal differences between air movement on inverted and non-inverted days (Figure 7). Inversions may thus be related to local phenomenon rather than large air masses. According to both HYSPLIT and ELA wind directions, Eklutna winds generally came from roughly southeast during the study periods. Therefore, winds at this site most likely come from moist and warm air passing over the Gulf of Alaska overall. It is worth noting that HYSPLIT results matched field measured ELA wind direction, strengthening confidence in HYSPLIT and suggesting it may be useful in similar studies in the future where wind direction may be unavailable.

The Role of Temperature in Snowmelt. Lack of correlation between temperature and melt lapses and differences in amount of inversions between the two suggest independence of temperature and melt inversions. Conventionally, temperature is expected to cause melt at all temporal scales—as air temperature cools there is less melt, so if temperature cools with elevation increase, then melt rate too will lessen. Our results illustrate that neither lapse lags the other, contradicting the traditional concept of temperature driving melt. Instead, temperature and melt seem de-coupled.

Other explanations may include the lowering of albedo and exposure of low-albedo ice by glacial microbes and algae, which increase melt (Ganey et al., 2017). These may be contributing to melt at lower elevations and therefore causing more non-inverted melt days, even while temperature remains inverted. The fact that melt lapse rate does not relate to temperature lapse rate is surprising and suggests something decouples the two, possibly local-scale environmental or

weather variables. The scale of correlation is important. In the case of this study, lapse rates were daily and uncorrelated. When these are averaged over weekly and monthly scales, they become more correlated (Dial, unpublished).

Better understanding of melt season inversions and their controls is crucial for studies that use point samples of temperature, such as DDMs. Strengthening this family of models is vital for understanding mountain and glacial climates into the future, especially in the context of sea level rise and water resources.

7. Products (students in bold.)

Ganey, G.Q., Loso, M.G., Burgess, A.B., and Dial, R.J (2017), The role of microbes in snowmelt and radiative forcing on a large Alaskan icefield. *Nature Geoscience.* 10:754-759. (included funding from NIWR grant to Dial and Geck in 2016, unreported here).

Dial, R. J., **Ganey, G. Q.,** Skiles, M. (2017), What color should snow algae be? Oral presentation at 7th International Conference on Polar and Alpine Microbiology, 11 September 2017, Nuuk, Greenland.

Dial, R. J., **Ganey, G. Q.,** Loso, M., Burgess, A. B., Skiles, M. (2017), What color should snow algae be and what does it mean for glacier melt? Oral presentation at American Geophysical Union Annual Fall Meeting, 14 December 2017, New Orleans, LA.

Dial, R. J. What color should snow algae be and what does it mean for glacier melt? Oral presentation at USGS Science Center, 14 January 2018, Anchorage, AK.

Dial, R. J. Glacier algae and meltwater: A role for red carbon in the cryosphere? Oral presentation at American Water Resources Association Alaska Section Annual Conference, 10 April 2018, Anchorage, AK.

8. Student support

Three undergraduates, two graduate students and an MS thesis, all at Alaska Pacific University.

9. Notable awards and achievements

Not applicable

10. Tables, figures and their captions

Presented at end of document.

References

Arendt, A. A. (2002). Rapid Wastage of Alaska Glaciers and Their Contribution to Rising Sea Level. *Science*, *297*(5580), 382–386. https://doi.org/10.1126/science.1072497

Arendt, A., Luthcke, S., Gardner, A., O'neel, S., Hill, D., Moholdt, G., & Abdalati, W. (2013). Analysis of a GRACE global Mascon solution for Gulf of Alaska glaciers. *Journal of Glaciology*, *59*(217), 913–924. https://doi.org/10.3189/2013JoG12J197

Barry, R., & Chorley, R. (2009). *Atmosphere, weather and climate*. Retrieved from https://books.google.com/books?hl=en&lr=&id=NxaPAgAAQBAJ&oi=fnd&pg=PP1&dq=Atmosphere,+Weather+and+Climate.+9th+edition&ots=O4FmyJoDX5&sig=dx6NCSHAxKsxXY93fvazUr-uSuk

Beamer, J. P., Hill, D. F., Arendt, A., & Liston, G. E. (2016). High-resolution modeling of coastal freshwater discharge and glacier mass balance in the Gulf of Alaska watershed. *Water Resources Research*, *52*(5), 3888–3909. https://doi.org/10.1002/2015WR018457

Beamer, J. P., Hill, D. F., McGrath, D., Arendt, A., & Kienholz, C. (2017). Hydrologic impacts of changes in climate and glacier extent in the Gulf of Alaska watershed. *Water Resources Research*, *53*(9), 7502–7520. https://doi.org/10.1002/2016WR020033

Bieniek, P. A., Bhatt, U. S., Thoman, R. L., Angeloff, H., Partain, J., Papineau, J., … Gens, R. (2012). Climate Divisions for Alaska Based on Objective Methods. *Journal of Applied Meteorology and Climatology*, *51*(7), 1276–1289. https://doi.org/10.1175/JAMC-D-11-0168.1

Brabets, T. P. (1993). Glacier runoff and sediment transport and deposition eklutna lake basin , Alaska. Retrieved from https://pubs.usgs.gov/wri/1992/4132/report.pdf

Dethlefs, A. (2012). *Snow Algae on the Harding Icefield: Influence on surface melt and limitation by nutrients and water*. Alaska Pacific University.

Dial, R. C., Dial, R. J., Saunders, R., Lang, S. A., Lee, B., Wimberger, P., … Shain, D. H. (2012). Historical biogeography of the North American glacier ice worm, Mesenchytraeus solifugus (Annelida: Oligochaeta: Enchytraeidae). *Molecular Phylogenetics and Evolution*, *63*(3), 577–584. https://doi.org/10.1016/j.ympev.2012.01.008

Dial, R. J. (2017). *Variable lapse rates and the mass balance of a well-studied glacier in south-central Alaska*. Anchorage, Alaska.

Ganey, G. Q., Loso, M. G., Burgess, A. B., & Dial, R. J. (2017). The role of microbes in snowmelt and radiative forcing on an Alaskan icefield. *Nature Geoscience*, *10*(10), 754–759. https://doi.org/10.1038/ngeo3027

Gardner, A. S., & Sharp, M. (2009). Sensitivity of net mass-balance estimates to near-surface temperature lapse rates when employing the degree-day method to estimate glacier melt. *Annals of Glaciology*, *50*(50), 80–86. https://doi.org/10.3189/172756409787769663

Gardner, A. S., Sharp, M. J., Koerner, R. M., Labine, C., Boon, S., Marshall, S. J., … Lewis, D. (2009). Near-surface temperature lapse rates over arctic glaciers and their implications for temperature downscaling. *Journal of Climate*, *22*(16), 4281–4298. https://doi.org/10.1175/2009JCLI2845.1

Ground Water in the Anchorage Area, Alaska. (2006). Retrieved from https://pubs.usgs.gov/fs/2006/3148/pdf/fs20063148.pdf

Hock, R. (2003). Temperature index melt modelling in mountain areas. *Journal of Hydrology*, *282*(1–4), 104–115. https://doi.org/10.1016/S0022-1694(03)00257-9

Hock, R., Jansson, P., & Braun, L. N. (2005). Modelling the Response of Mountain Glacier Discharge to Climate Warming, (Ipcc 2001), 243–252. https://doi.org/10.1007/1-4020-3508-X_25

Hodgkins, R., Carr, S., Pálsson, F., Guodmundsson, S., & Björnsson, H. (2012). Sensitivity analysis of temperature-index melt simulations to near-surface lapse rates and degree-day factors at vestari-hagafellsjökull, langjökull, iceland. *Hydrological Processes*, *26*(24), 3736–3748. https://doi.org/10.1002/hyp.8458

Lesins, G., Duck, T. J., & Drummond, J. R. (2010). Climate Trends at Eureka in the Canadian High Arctic. *ATMOSPHERE-OCEAN*, *48*(2), 59–80. https://doi.org/10.3137/AO1103.2010

Machguth, H., Purves, R. S., Oerlemans, J., Hoelzle, M., & Paul, F. (2008). Exploring uncertainty in glacier mass balance modelling with Monte Carlo simulation. *Cryosphere*, *2*(2), 191–204. https://doi.org/10.5194/tc-2-191-2008

Marshall, S. J., Sharp, M. J., Burgess, D. O., & Anslow, F. S. (2006). Near-surface-temperature lapse rates on the Prince of Wales Icefield, Ellesmere Island, Canada: Implications for regional downscaling of temperature. *International Journal of Climatology*. https://doi.org/10.1002/joc.1396

Martins, C.-F. (1842). *Remarques et expériences sur les glaciers sans névé de la chaine du Faulhorn.* Paris: M. Rivière. Retrieved from https://books.google.com/books?id=HwIUAAAAQAAJ&printsec=frontcover&vq=firn&source=gbs_atb#v=onepage&q&f=false

Minder, J. R., Mote, P. W., & Lundquist, J. D. (2010). Surface temperature lapse rates over complex terrain: Lessons from the Cascade Mountains. *Journal of Geophysical Research Atmospheres*, *115*(14). https://doi.org/10.1029/2009JD013493

Pellicciotti, F., Brock, B., Strasser, U., Burlando, P., Funk, M., & Corripio, J. (2005). An enhanced temperature - index glacier melt model including the shortwave radiation balance : development and testing for Haut Glacier d â€™ Arolla , Switzerland. *Journal of Glaciology*, *51*(175), 573–587. https://doi.org/10.3189/172756505781829124

Petersen, L., & Pellicciotti, F. (2011). Spatial and temporal variability of air temperature on a melting glacier: Atmospheric controls, extrapolation methods and their effect on melt modeling, Juncal Norte Glacier, Chile. *Journal of Geophysical Research Atmospheres*, *116*(23), n/a-n/a. https://doi.org/10.1029/2011JD015842

Petersen, L., Pellicciotti, F., Juszak, I., Carenzo, M., & Brock, B. (2013). Suitability of a constant air temperature lapse rate over an Alpine glacier: Testing the Greuell and Böhm model as an alternative. *Annals of Glaciology*, *54*(63), 120–130. https://doi.org/10.3189/2013AoG63A477

Pike, G., Pepin, N. C., Schaefer, M. (2013). High latitude local scale temperature complexity: The example of Kevo Valley, Finnish Lapland. *International Journal of Climatology*, *33*(8), 2050–2067. https://doi.org/10.1002/joc.3573

Rolland, C. (2003). Spatial and seasonal variations of air temperature lapse rates in alpine regions. *Journal of Climate*, *16*(7), 1032–1046. https://doi.org/10.1175/1520-0442(2003)016<1032:SASVOA>2.0.CO;2

Rolph, G., Stein, A., Stunder, B. (2017). Real-time Environmental Applications and Display sYstem: READY. *Environmental Modelling & Software*, *95*, 210–228. https://doi.org/10.1016/J.ENVSOFT.2017.06.025

Sass, L. C., Loso, M. G., Geck, J., Thoms, E. E., & Mcgrath, D. (2017). Geometry, mass balance and thinning at Eklutna Glacier, Alaska: An altitude-mass-balance feedback with implications for water resources. *Journal of Glaciology*, *63*(238), 343–354. https://doi.org/10.1017/jog.2016.146

Sass, L. C., O'Neel, S., Loso, M. G., MacGregor, J. A., Catania, G. A., & Larsen, C. F. (2009). Contributions of climate and dynamics to mass wastage and accumulation zone thinning of Eklutna Glacier, Alaska. *American Geophysical Union, Fall Meeting 2009, Abstract Id. C32A-04*. Retrieved from http://adsabs.harvard.edu/abs/2009AGUFM.C32A..04S

Stein, A. F., Draxler, R. R., Rolph, G. D., Stunder, B. J. B., Cohen, M. D., Ngan, F., … Ngan, F. (2015). NOAA's HYSPLIT Atmospheric Transport and Dispersion Modeling System. *Bulletin of the American Meteorological Society*, *96*(12), 2059–2077. https://doi.org/10.1175/BAMS-D-14-00110.1

VanLooy, J., Forster, R., & Ford, A. (2006). Accelerating thinning of Kenai Peninsula glaciers, Alaska. *Geophysical Research Letters*, *33*(21), L21307. https://doi.org/10.1029/2006GL028060

Velicogna, I., & Wahr, J. (2013). Time-variable gravity observations of ice sheet mass balance: Precision and limitations of the GRACE satellite data. *Geophysical Research Letters*, *40*(12), 3055–3063. https://doi.org/10.1002/grl.50527

Figures

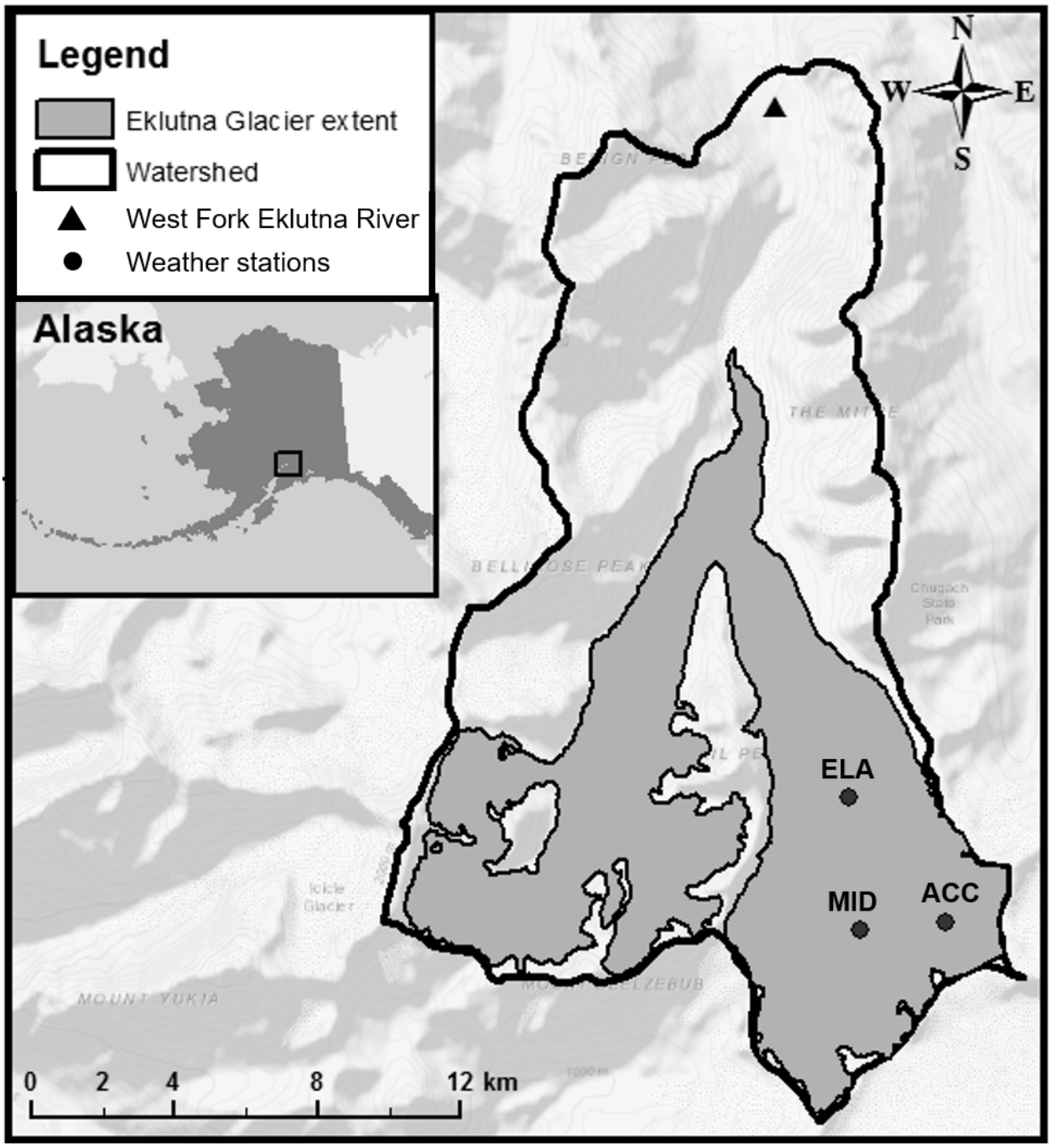

Figure 1: Map of Eklutna Glacier and weather station sites. The glacier extent (2010) is shown in dark gray, outlined in black. The thick black boundary depicts the glacier's watershed. Black dots depict study sites, three weather stations of increasing elevation in order ELA, MID, and ACC. Black triangle depicts nearby West Fork Eklutna River where barometer was present. Upper left inset shows glacier location in Alaska.

(a) (b)

Figure 2: (a) An example of a weather station atop a tripod, with temperature sensors 2 m above ground, windspeed and direction facing North, and camera facing ablation stake. (b) A photo from weather station ACC, elevation 1505 m asl, collected on 9 July 2017 at 7:15 am. Ablation stake is visible on the right side atop the glacial surface, with surrounding mountains in the background. Camera was facing North.

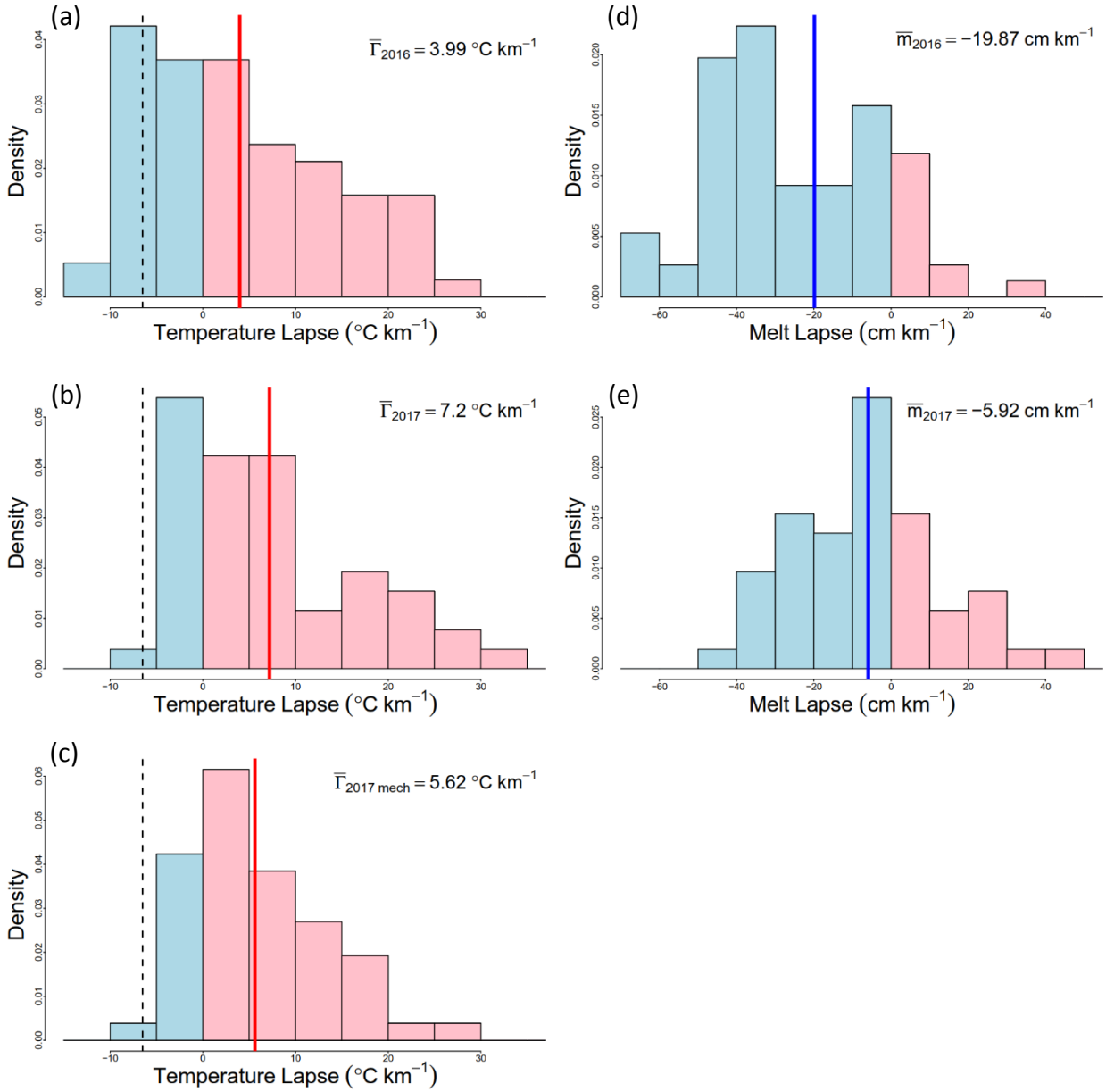

Figure 3: Density plots of temperature and melt lapses for 2016 and 2017. The blue bar color represents negative lapses (considered 'non-inverted') and pink bar color represents positive lapses ('inverted'). The red vertical, solid line and upper right gamma value represent the temperature lapse mean value if inverted, while the line is blue if non-inverted. 2017 mechanically-aspirated mean is specified with 'mech' subscript. The black, dotted vertical line represents the often-used value of -6.5 °C km^{-1} in the case of temperature lapse. Upper right m value represents melt lapse mean. In (a) and (b) temperatures are naturally-aspirated; in (c), temperatures are mechanically-aspirated; (d) refers to melt lapse in 2016; and (e) refers to melt lapse in 2017.

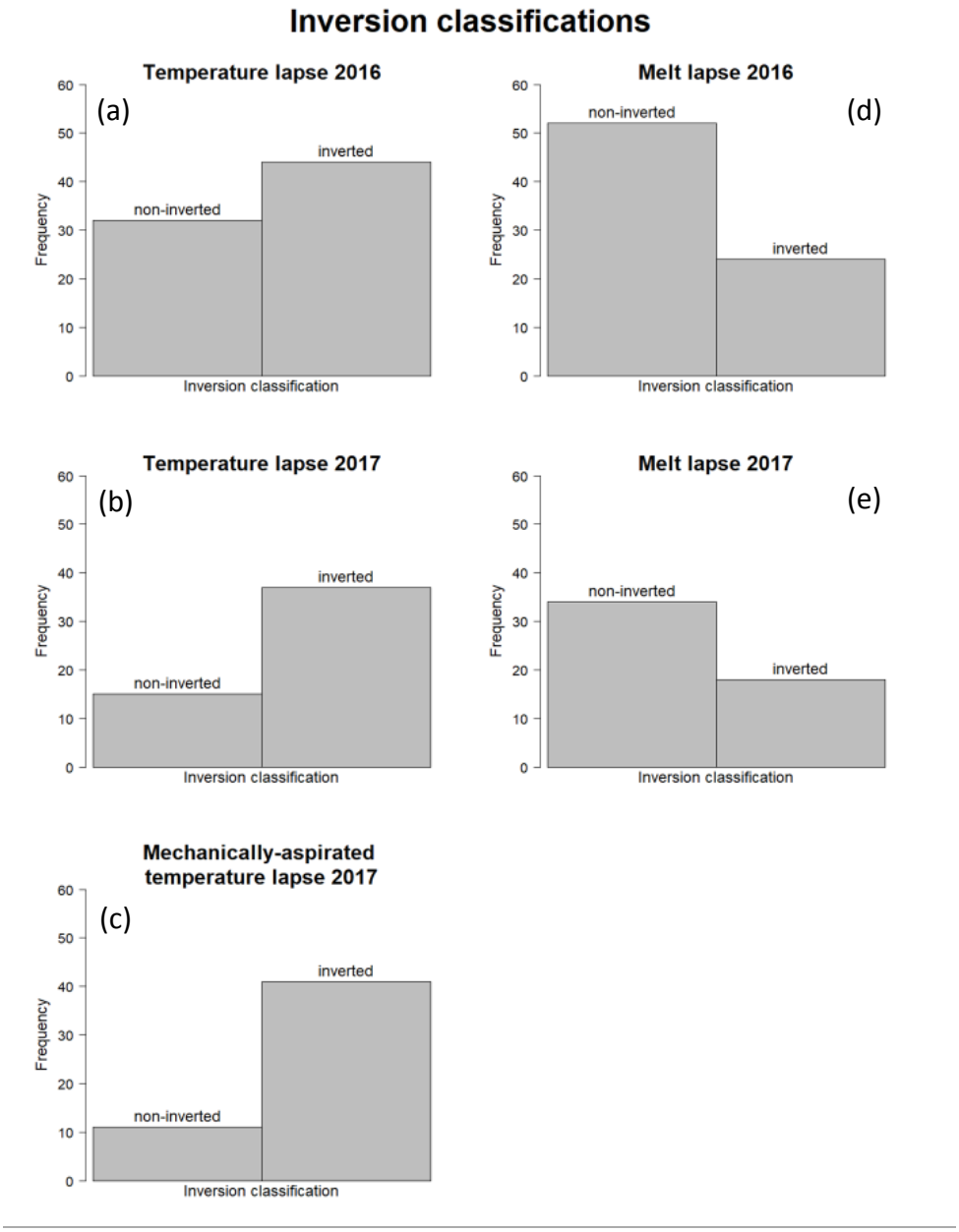

Figure 4: Inversion days for both temperature and melt DOY 136 - 211 (15 May - 29 July), a total of 76 days in year 2016 and DOY 188 - 239 (7 July - 27 August), a total of 52 days in year 2017. Temperature lapse classifications represented by plots on left, with melt on right. In (a) and (b), temperatures are naturally-aspirated. In (c), temperatures are mechanically-aspirated, as indicated. (d) refers to melt lapse in 2016 and (e) to melt lapse in 2017. All classifications based on daily lapse.

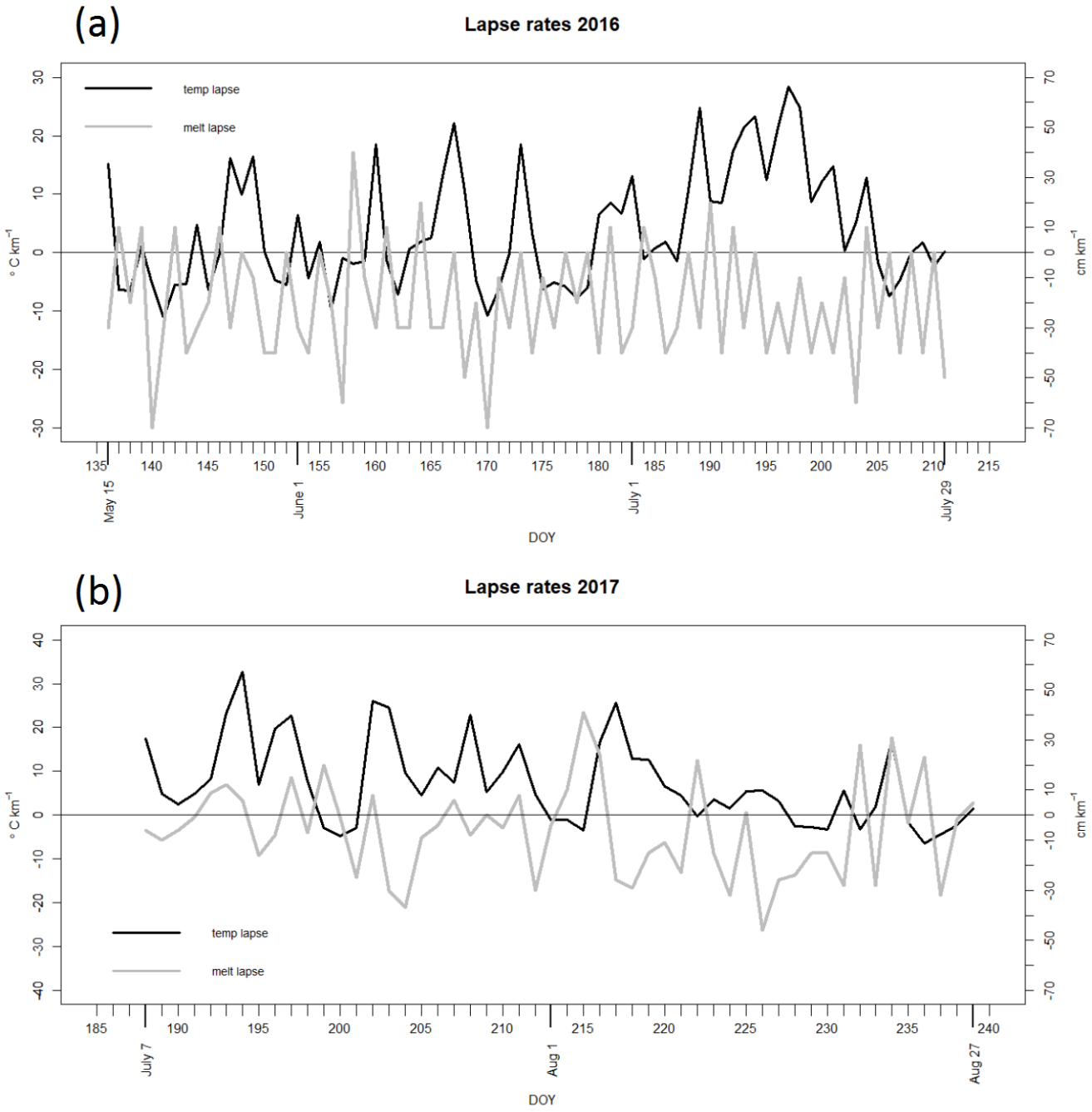

Figure 5: TOP: (a) Temperature and melt lapse on Eklutna Glacier over DOY 136 - 211 (15 May - 29 July), a total of 76 days in year 2016. The black line represents temperature lapse (C° km-1) while the gray line represents melt lapse (cm km-1). Anything above 0 line represents an inversion. Temperatures are naturally-aspirated. BOTTOM: (b) Temperature and melt lapse on Eklutna Glacier over DOY 188 - 239 (7 July - 27 August), a total of 52 days in year 2017. Black line represents temperature lapse (C° km-1) and gray line represents melt lapse (cm km-1). Anything above 0 line represents an inversion. In (a), temperatures are naturally-aspirated. In (b), temperatures are mechanically-aspirated, as indicated.

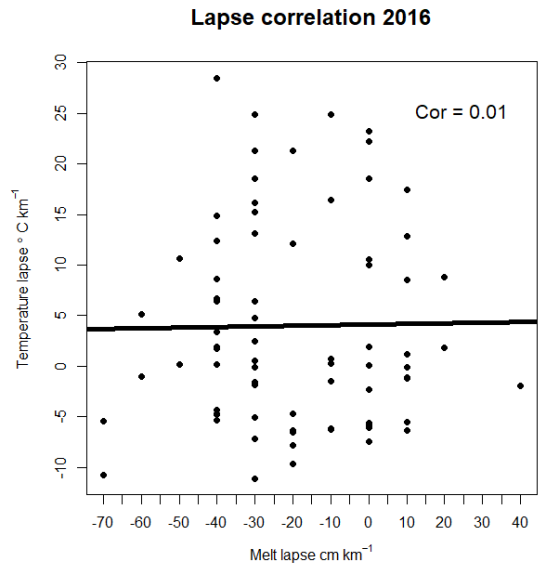

(a)

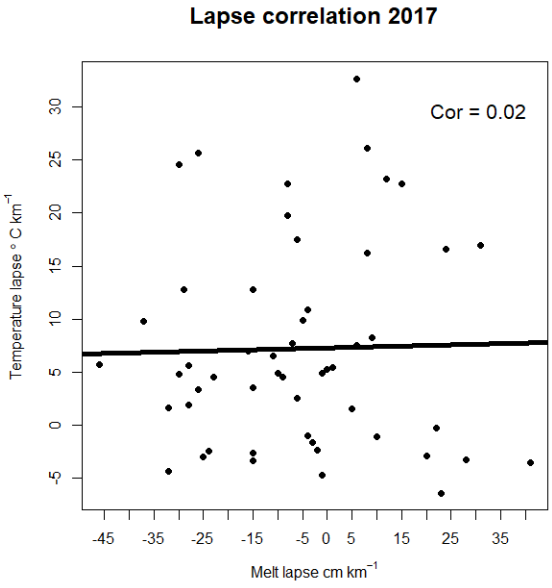

(b)

Figure 6: Temperature lapse (C° km-1) against melt lapse (cm km-1) on (a) 15 May - 29 July, a total of 76 days in year 2016 and (b) 7 July - 27 August, a total of 52 days in year 2017. Both lapses are daily. Black dots represent instances of naturally-aspirated temperature lapse and melt lapse on the same day. The thick black lines represent linear relationship between lapses. The estimated measure of association is represented on upper right, calculated using Pearson's product-moment correlation.

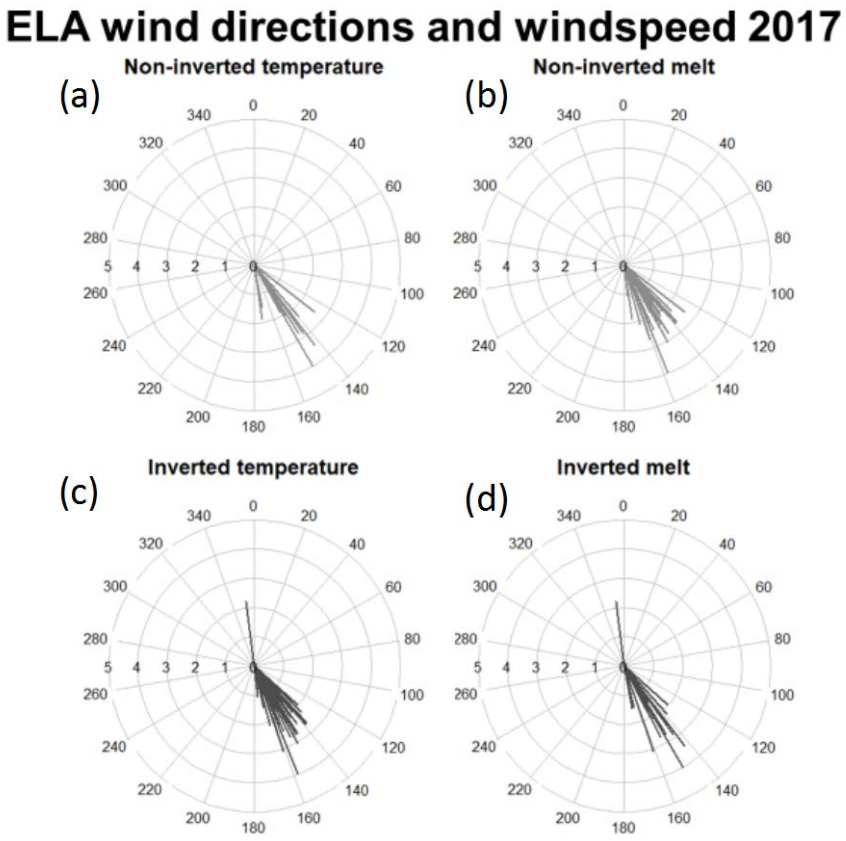

Figure 7: Mean daily windspeed and wind direction from ELA anemometer data for DOY 188-239 (7 July - 27 August), a total of 52 days in year 2017. The light gray lines indicate non-inverted days while dark gray lines indicate inverted days for both melt on the left and temperature on the right. Gray radial grid represents mean windspeed ranging from 0 to 5 m sec-1. (a) refers to non-inverted naturally-aspirated temperature lapse days, (b) refers to non-inverted melt lapse days, (c) refers to inverted naturally-aspirated temperature lapse days, and (d) refers to inverted melt lapse days.

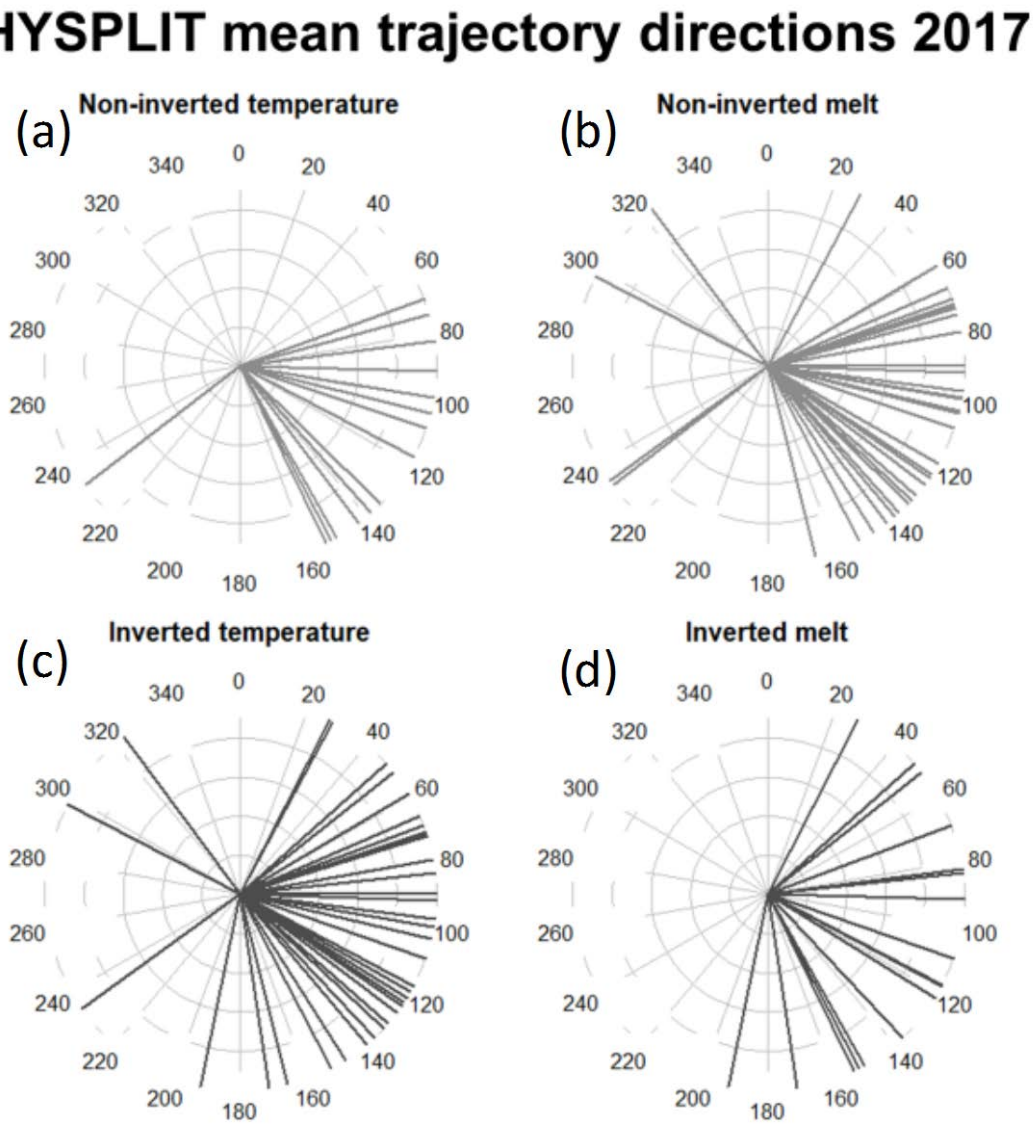

Figure 8: Mean daily trajectory results from the HYSPLIT model run at 48 hours for DOY 188-239 (7 July - 27 August), a total of 52 days in year 2017. The light gray lines indicate non-inverted days while dark gray lines indicate inverted days for both melt on the left and temperature on the right. Gray radial grid does not correspond to windspeed, so all line limits are equal. (a) refers to non-inverted naturally-aspirated temperature lapse days, (b) refers to non-inverted melt lapse days, (c) refers to inverted naturally-aspirated temperature lapse days, and (d) refers to inverted melt lapse days.

TABLES

Table 1: Weather stations on Eklutna Glacier, with latitude and longitude coordinates and heights in meters above mean sea level (m asl).

Weather Station	Location	GPS Height (m asl)
ELA	61.21156360, -148.9575564	1376
MID	61.19563419, -148.9548241	1449
ACC	61.19638706, -148.9333888	1505

Table 2: Cloud cover classification scale, 0-100% with cloud cover (cc) value assigned based on weather station pictures.

Cloud cover (cc)	% of sky covered by clouds	cc value assigned
few	<0-10	5
isolated	10-25	17.5
scattered	25-50	37.5
broken	50-90	70
overcast	90-100	95
fog	fog at stake, blocking sky	100
dark	evening/night time	NA

Table 3: Inverted temperature lapse probability results as a function of all available weather variables and year using logistic regression. Both additive and interactive relationship of weather variables and year are present. Significant variables under Bonferroni correction of 0.004 are represented in bold.

	probability of inverted temperature lapse (additive)		do *year* and weather covariate work together? (additive)		probability of inverted temperature lapse (interactive)		do *year* and weather covariate interact? (interactive)		weather covariate interaction with year		number of observations
	Odds Ratio	*p*	*Odds Ratio*	*p*	*Odds Ratio*	*p*	*Odds Ratio*	*p*	*Odds Ratio*	*p*	
Mean total temperature (°C)	+	**<.001**	+	0.047	+	0.156	+	0.047	-	0.157	128
ELA max temperature (°C)	+	**<.001**	+	**0.001**	+	0.164	+	0.022	-	0.165	128
ELA mean temperature (°C)	+	**0.002**	+	0.039	+	0.191	+	0.054	-	0.191	128
MID max temperature (°C)	+	**<.001**	+	**<.001**	-	0.678	+	0.6	+	0.677	128
MID mean temperature (°C)	+	**<.001**	+	0.13	+	0.197	+	0.088	-	0.197	128
ACC max temperature (°C)	+	**<.001**	+	**<.001**	_	0.592	+	0.464	+	0.591	128
ACC mean temperature (°C)	+	**<.001**	+	0.038	+	0.19	+	0.053	-	0.191	128
Mean total cloud cover (0 - 100)	-	0.024	NA	NA	-	0.024					52
ELA relative humidity (%)	0	0.528	+	0.166	+	0.818	+	0.743	0	0.818	128
ELA total rain (mm)	0	0.939	+	0.132	-	0.719	+	0.159	+	0.719	128
ELA max windspeed (m sec^{-1})	-	**0.002**	NA	NA	-	**0.002**					52
ELA mean windspeed (m sec^{-1})	-	0.074	NA	NA	-	0.074					52
HYSPLIT mean trajectories (degrees °)	0	0.361	NA	NA	0	0.361					52
Absolute pressure (kPa)	+	0.032	+	0.027	-	0.463	-	0.47	+	0.462	93
ELA incoming radiation	0	0.029	NA	NA	0	0.029					76
ELA outgoing radiation	0	0.144	NA	NA	0	0.144					76
ELA albedo	-	0.021	NA	NA	-	0.021					76

Bonferroni correction = 0.004

Odds Ratio = 0 if within 0.98-1.02

Table 4: 2016 inverted (naturally-aspirated) temperature lapse probability results as a function of all available weather variables using logistic regression. Data covers DOY 136-211 (15 May - 29 July), a total of 76 days in year 2016. All variables as daily means unless stated otherwise (e.g., ELA total rain, which is a daily total). P-value defined as Wald-test p-value. Significant variables under Bonferroni correction of 0.004 are represented in bold.

	probability of inverted temperature lapse 2016	
	B	*p*
Mean total temperature (°C)	+	**<.001**
ELA max temperature (°C)	+	**<.001**
ELA mean temperature (°C)	+	**0.003**
MID max temperature (°C)	+	**<.001**
MID mean temperature (°C)	+	**<.001**
ACC max temperature (°C)	+	**<.001**
ACC mean temperature (°C)	+	**<.001**
ELA relative humidity (%)	0	0.505
ELA total rain (mm)	-	0.713
Absolute pressure (kPa)	+	0.605
ELA albedo (0 - 1)	-	0.021
ELA incoming radiation (W m^{-2})	+	0.029
ELA outgoing radiation (W m^{-2})	0	0.144

Table 5: 2017 inverted (naturally-aspirated) and mechanically-aspirated temperature lapse probability results as a function of all available weather variables using logistic regression. Data covers DOY 188-239 (7 July - 27 August), a total of 52 days. All variables as daily means unless stated otherwise (e.g., ELA total rain, which is a daily total). P-value defined as Wald-test p-value. Significant variables under Bonferroni correction of 0.004 are represented in bold.

	probability of inverted temperature lapse 2017		**probability of inverted mechanically-aspirated temperature lapse 2017**	
	B	*p*	B_{mech}	p_{mech}
Mean total temperature (°C)	+	0.014	+	0.014
ELA max temperature (°C)	+	0.05	+	0.058
ELA mean temperature (°C)	+	0.274	+	0.135
MID max temperature (°C)	+	**0.002**	+	0.006
MID mean temperature (°C)	+	0.01	+	0.013
ACC max temperature (°C)	+	**0.002**	+	**0.002**
ACC mean temperature (°C)	+	**0.003**	+	**0.004**
Mean total cloud cover (0 - 100)	-	0.024	-	0.061
ELA relative humidity (%)	0	0.933	+	0.568
ELA total rain (mm)	0	0.996	-	0.704
ELA max windspeed (m sec-1)	-	**0.002**	-	**0.003**
ELA mean windspeed (m sec-1)	-	0.074	-	0.136
HYSPLIT mean trajectories (degrees °)	0	0.361	0	0.206
Absolute pressure (kPa)	+	0.031	+	0.004

Table 6: 2017 inverted melt lapse probability results as a function of all available weather variables using logistic regression. Data covers DOY 136-211 (15 May - 29 July), a total of 76 days in 2016 and DOY 188-239 (7 July - 27 August), a total of 52 days in 2017. All variables as daily means unless stated otherwise (e.g., ELA total rain, which is a daily total). P-value defined as Wald-test p-value. Significant variables under Bonferroni correction of 0.004 are represented in bold.

	probability of inverted melt lapse 2016		**probability of inverted melt lapse 2017**	
	B_{2016}	P_{2016}	B_{2017}	P_{2017}
Mean total temperature (°C)	0	0.984	+	0.704
ELA max temperature (°C)	0	0.915	0	0.889
ELA mean temperature (°C)	0	0.959	+	0.844
MID max temperature (°C)	+	0.557	+	0.802
MID mean temperature (°C)	0	0.953	+	0.731
ACC max temperature (°C)	0	0.921	+	0.833
ACC mean temperature (°C)	0	0.944	0	0.739
ELA relative humidity (%)	0	0.853	+	0.06
ELA total rain (mm)	-	0.287	0	0.838
Absolute pressure (kPa)	+	0.777	+	0.673
ELA albedo (0 - 1)	+	0.153	NA	NA
ELA incoming radiation (W m^{-2})	0	0.975	NA	NA
ELA outgoing radiation (W m^{-2})	0	0.99	NA	NA
Mean total cloud cover (0 - 100)	NA	NA	0	0.739
ELA max windspeed (m sec-1)	NA	NA	+	0.628
ELA mean windspeed (m sec-1)	NA	NA	+	0.562
HYSPLIT mean trajectories (degrees °)	NA	NA	0	0.769

Table 7: Pairwise correlation among all available weather variables, data from combined years 2016 and 2017. All variables are daily means. Variables against each other are represented by 'variable 1' and 'variable 2,' with correlation value to their right. Only correlation values of 0.50 or above are included. Italics highlight lapse correlations.

Pairwise correlation among all weather variables

Variable 1	Variable 2	Correlation value (r)
Mean total temperature (°C)	MID mean temperature (°C)	0.99
Mean total temperature (°C)	ACC mean temperature (°C)	0.98
ACC mean temperature (°C)	MID mean temperature (°C)	0.96
Mean total temperature (°C)	ELA mean temperature (°C)	0.93
MID mean temperature (°C)	ELA mean temperature (°C)	0.89
ELA mean temperature (°C)	ELA max temperature (°C)	0.85
ACC mean temperature (°C)	ELA mean temperature (°C)	0.84
Mean total temperature (°C)	ELA max temperature (°C)	0.80
ACC melt (cm day^{-1})	*Melt lapse (cm km^{-1})*	0.79
ACC mean temperature (°C)	*Temperature lapse (°C km^{-1})*	0.79
MID max temperature (°C)	ELA max temperature (°C)	0.77
ACC mean temperature (°C)	ELA max temperature (°C)	0.76
MID mean temperature (°C)	ELA max temperature (°C)	0.75
ACC mean temperature (°C)	ACC max temperature (°C)	0.73
ACC max temperature (°C)	MID max temperature (°C)	0.72
ACC mean temperature (°C)	MID max temperature (°C)	0.72
Mean total temperature (°C)	MID max temperature (°C)	0.71
ACC max temperature (°C)	*Temperature lapse (°C km^{-1})*	0.70
ACC max temperature (°C)	ELA max temperature (°C)	0.70
MID mean temperature (°C)	MID max temperature (°C)	0.69
MID mean temperature (°C)	*Temperature lapse (°C km^{-1})*	0.66
MID max temperature (°C)	ELA mean temperature (°C)	0.65
Mean total temperature (°C)	*Temperature lapse (°C km^{-1})*	0.64
Mean total temperature (°C)	ACC max temperature (°C)	0.64
ACC max temperature (°C)	MID mean temperature (°C)	0.60
ELA melt (cm day^{-1})	ELA mean temperature (°C)	0.52
ELA melt (cm day^{-1})	Mean total temperature (°C)	0.51
MID max temperature (°C)	*Temperature lapse (°C km^{-1})*	0.51
ELA melt (cm day^{-1})	MID mean temperature (°C)	0.50

APPENDIX – Supplemental Figures and Tables

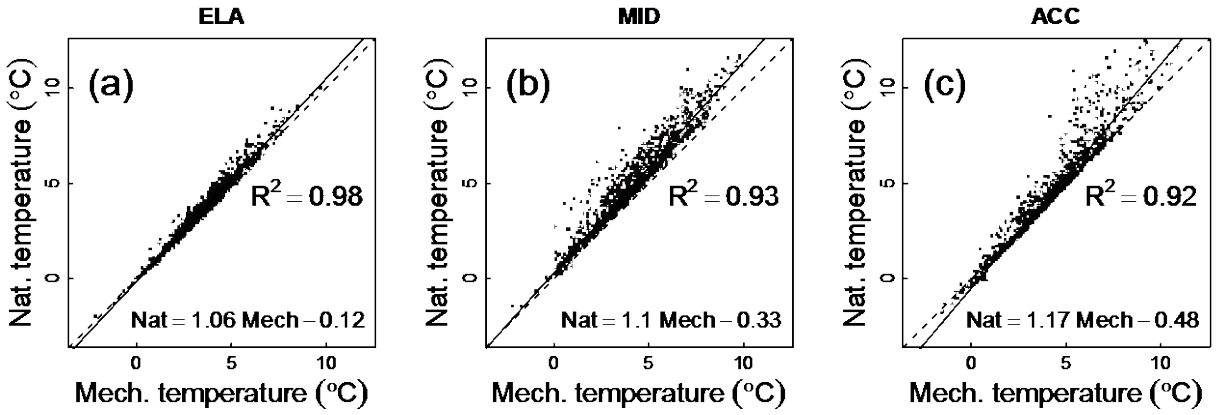

Supplemental Figure 1: 2017 hourly naturally-aspirated (Nat.) against mechanically-aspirated (Mech.) temperatures. Hourly data covers 7 July - 27 August, a total of 52 days. (a) represents these temperatures at site ELA, (b) at site MID, and (c) at site ACC. The estimated measure of association is represented within box on lower right of each plot, calculated using Pearson's product-moment correlation. Dashed line represents a slope of 1, and gray line represents linear fit line between naturally and mechanically-aspirated temperatures. Linear fit equations are presented in lower right of each panel with R^2 value above.

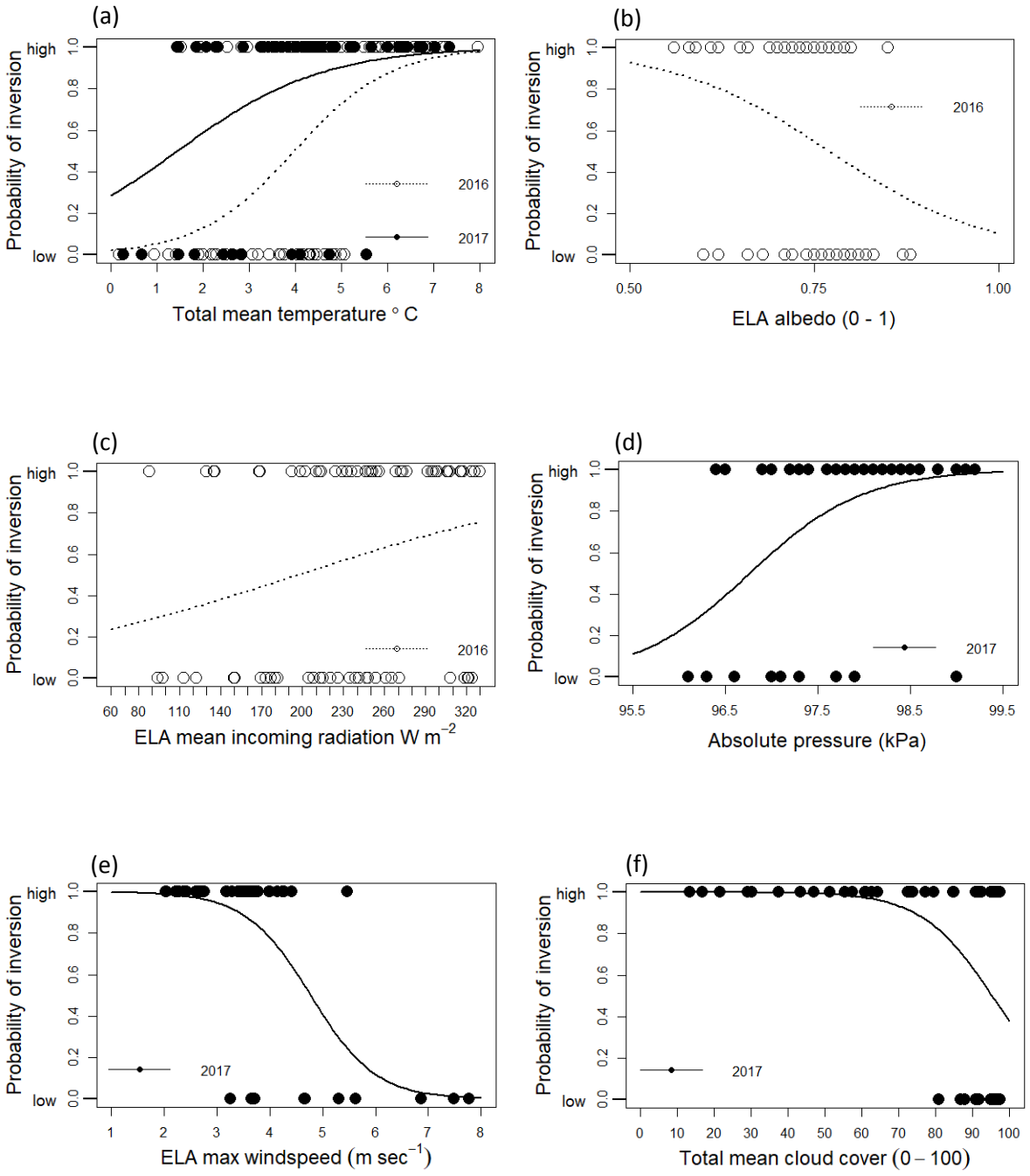

Supplemental Figure 2: Probability plots of significant weather variables from inverted (non-aspirated) temperature lapse probability results as a function of all available weather variables using logistic regression. Year 2016 is represented by open dots and dotted regression line, year 2017 is represented by closed dots and solid regression line.

Supplemental Table 1: 2016 inverted (non-aspirated) temperature lapse probability results as a function of all available weather variables using logistic regression. Data covers DOY 136-211 (15 May - 29 July), a total of 76 days in year 2016. All variables as daily means unless stated otherwise (e.g., ELA total rain, which is a daily total). P-value defined as Wald-test p-value. Significant variables under Bonferroni correction of 0.004 are represented in bold.

	probability of inverted temperature lapse 2016				**intercept**		
	B	*CI*	*p*	*R2 / adj. R2*	*B*	*CI*	*p*
Mean total temperature (°C)	0.97	0.56, 1.48	**<.001**	.325 / .438	-3.83	-6.11, -2.03	<.001
ELA max temperature (°C)	0.76	0.39, 1.22	**<.001**	.235 / .316	-4.71	-7.70, -2.26	<.001
MID max temperature (°C)	0.59	0.31, 0.93	**<.001**	.251 / .338	-4.44	-7.15, -2.18	<.001
MID mean temperature (°C)	0.9	0.52, 1.38	**<.001**	.323 / .434	-3.7	-5.93, -1.95	<.001
ACC max temperature (°C)	0.73	0.46, 1.09	**<.001**	.466 / .626	-5.69	-8.56, -3.47	<.001
ACC mean temperature (°C)	1.12	0.68, 1.72	**<.001**	.437 / .588	-4.46	-7.02, -2.56	<.001
ELA mean temperature (°C)	0.63	0.25, 1.08	**0.003**	.135 / .182	-2.22	-4.07, -0.60	0.011
ELA albedo (0 - 1)	-9.39	-18.04, -1.90	0.021	.078 / .105	7.23	1.69, 13.68	0.017
ELA incoming radiation (Wm^{-2})	0.01	0.00, 0.02	0.029	.065 / .087	-1.68	-3.62, 0.12	0.075
ELA outgoing radiation (Wm^{-2})	0.01	-0.00, 0.02	0.144	.029 / .038	-0.99	-2.87, 0.80	0.283
ELA relative humidity (%)	0.02	-0.04, 0.08	0.505	.006 / .008	-1.31	-6.21, 3.53	0.594
Absolute pressure (kPa)	0.36	-0.99, 1.79	0.605	.686 / .746	-35.34	-174.93, 96.42	0.602
ELA total rain (mm)	-0.21	-1.49, 1.01	0.713	.002 / .002	0.34	-0.13, 0.82	0.156

Supplemental Table 2: 2016 inverted (non-aspirated) temperature lapse probability results as a function of all available weather variables using logistic regression. Data covers DOY 136-211 (15 May - 29 July), a total of 76 days in year 2016. All variables as daily means unless stated otherwise (e.g., ELA total rain, which is a daily total). P-value defined as Wald-test p-value.

	probability of inverted melt lapse 2016				**Intercept**		
	B	*CI*	*p*	*R2 / adj. R2*	*B*	*CI*	*P*
ELA albedo (0 - 1)	5.73	-1.80, 14.12	0.153	.028 / .040	-4.99	-11.29, 0.56	0.094
ELA total rain (mm)	-1.8	-7.37, 0.29	0.287	.032 / .045	-0.67	-1.18, -0.18	0.008
MID max temperature (°C)	0.06	-0.14, 0.25	0.557	.005 / .006	-1.26	-3.04, 0.44	0.149
Absolute pressure (kPa)	0.21	-1.25, 1.79	0.777	.669 / .742	-21.77	-175.29, 120.89	0.768
ELA relative humidity (%)	-0.01	-0.06, 0.05	0.853	.000 / .001	-0.3	-5.57, 4.73	0.909
ELA max temperature (°C)	0.01	-0.26, 0.29	0.915	.000 / .000	-0.87	-2.83, 1.03	0.37
ACC max temperature (°C)	0.01	-0.14, 0.15	0.921	.000 / .000	-0.84	-2.23, 0.48	0.222
ACC mean temperature (°C)	-0.01	-0.23, 0.22	0.944	.000 / .000	-0.74	-1.91, 0.36	0.198
MID mean temperature (°C)	0.01	-0.25, 0.27	0.953	.000 / .000	-0.81	-2.16, 0.45	0.218
ELA mean temperature (°C)	-0.01	-0.37, 0.35	0.959	.000 / .000	-0.74	-2.33, 0.76	0.344
ELA incoming radiation (Wm^{-2})	0	-0.01, 0.01	0.975	.000 / .000	-0.8	-2.76, 1.03	0.4
Mean total temperature (°C)	0	-0.28, 0.28	0.984	.000 / .000	-0.76	-2.13, 0.52	0.256
ELA outgoing radiation (Wm^{-2})	0	-0.01, 0.01	0.990	.000 / .000	-0.78	-2.77, 1.07	0.418

Supplemental Table 3: 2017 inverted (non-aspirated) temperature lapse probability results as a function of all available weather variables using logistic regression. Data covers DOY 188-239 (7 July - 27 August), a total of 52 days. All variables as daily means unless stated otherwise (e.g., ELA total rain, which is a daily total). P-value defined as Wald-test p-value. Significant variables under Bonferroni correction of 0.004 are represented in bold.

	probability of inverted temperature lapse 2017				**intercept**		
	B	*CI*	*p*	*R2 / adj. R2*	*B*	*CI*	*p*
ELA max windspeed (m sec-1)	-1.94	-3.48, -0.92	**0.002**	.365 / .522	8.28	4.33, 14.27	<.001
ACC max non-aspirated temperature (°C)	0.91	0.44, 1.61	**0.002**	.386 / .553	-4.22	-7.88, -1.69	0.006
MID max non-aspirated temperature (°C)	0.71	0.31, 1.24	**0.002**	.257 / .368	-3.46	-6.61, -1.03	0.013
ACC mean non-aspirated temperature (°C)	0.67	0.29, 1.18	**0.003**	.234 / .335	-1.74	-3.62, -0.16	0.045
MID mean non-aspirated temperature (°C)	0.52	0.16, 0.96	0.01	.150 / .214	-1.4	-3.32, 0.28	0.12
mean total non-aspirated temperature (°C)	0.64	0.17, 1.20	0.014	.137 / .212	-0.91	-2.77, 0.80	0.306
mean total cloud cover (0 - 100)	-0.1	-0.22, -0.04	0.024	.245 / .351	9.98	3.87, 21.11	0.019
Absolute pressure (kPa)	0.97	0.13, 1.92	0.031	.094 / .135	-93.72	-186.49, -11.56	0.033
ELA max non-aspirated temperature (°C)	0.37	0.03, 0.78	0.05	.083 / .118	-0.9	-2.84, 0.88	0.332
ELA mean windspeed (m sec-1)	-0.89	-1.96, 0.04	0.074	.065 / .093	2.94	0.72, 5.57	0.015
ELA mean non-aspirated temperature (°C)	0.24	-0.18, 0.68	0.274	.024 / .034	0.07	-1.52, 1.68	0.93
HYSPLIT mean trajectories (degrees °)	0	-0.02, 0.00	0.361	.018 / .026	2.18	-0.28, 5.69	0.136
ELA relative humidity (%)	0	-0.11, 0.11	0.933	.000 / .000	0.49	-8.97, 10.86	0.92
ELA total rain (mm)	0	-0.22, 0.31	0.996	.000 / .000	0.9	0.30, 1.56	0.004

Supplemental Table 4: 2017 inverted mechanically-aspirated temperature lapse probability results as a function of all available weather variables using logistic regression. Data covers DOY 188-239 (7 July - 27 August), a total of 52 days. All variables as daily means unless stated otherwise (e.g., ELA total rain, which is a daily total). P-value defined as Wald-test p-value. Significant variables under Bonferroni correction of 0.004 are represented in bold.

	probability of inverted temperature lapse 2017 (mechanically-aspirated)				**intercept**		
	B	*CI*	*p*	*R2 / adj. R2*	*B*	*CI*	*p*
ACC max temperature (°C)	0.98	0.46, 1.74	**0.002**	.298 / .463	-3.35	-6.58, -0.91	0.017
ELA max windspeed (m sec^{-1})	-1.63	-2.98, -0.75	**0.003**	.320 / .497	7.79	4.17, 13.31	<.001
Absolute pressure (kPa)	1.65	0.62, 2.92	0.004	.186 / .289	-159.72	-283.15, -59.54	0.004
ACC mean temperature (°C)	0.8	0.32, 1.41	0.004	.215 / .334	-1.52	-3.52, 0.21	0.105
MID max temperature (°C)	0.68	0.25, 1.24	0.006	.192 / .298	-1.93	-4.36, 0.14	0.085
MID mean temperature (°C)	0.6	0.17, 1.14	0.013	.142 / .221	-0.86	-2.64, 0.79	0.317
mean total temperature (°C)	0.64	0.17, 1.20	0.014	.137 / .212	-0.91	-2.77, 0.80	0.306
ELA max temperature (°C)	0.44	0.02, 0.94	0.058	.077 / .120	-0.69	-2.84, 1.35	0.512
mean total cloud cover (0 - 100)	-0.08	-0.19, -0.02	0.061	.149 / .232	7.98	2.71, 18.31	0.035
ELA mean temperature (°C)	0.4	-0.10, 0.96	0.135	.045 / .070	0	-1.79, 1.81	1
ELA mean windspeed (m sec^{-1})	-0.78	-1.89, 0.23	0.136	.043 / .067	3.12	0.72, 5.93	0.016
HYSPLIT mean trajectories (degrees °)	-0.01	-0.03, 0.00	0.206	.043 / .066	3.99	0.62, 9.33	0.071
ELA relative humidity (%)	0.03	-0.09, 0.15	0.568	.006 / .009	-1.65	-11.81, 9.33	0.751
ELA total rain (mm)	-0.04	-0.26, 0.26	0.704	.003 / .004	1.35	0.69, 2.10	<.001

Supplemental Table 5: 2017 inverted melt temperature lapse probability results as a function of all available weather variables using logistic regression. Data covers DOY 188-239 (7 July - 27 August), a total of 52 days. All variables as daily means unless stated otherwise (e.g., ELA total rain, which is a daily total).

	probability of inverted melt lapse 2017				**intercept**		
	B	*CI*	*p*	R^2 / *adj. R2*	*B*	*CI*	*p*
ELA relative humidity (%)	0.13	0.01, 0.28	0.060	.081 / .112	-12.32	-26.07, -1.30	0.049
ELA mean windspeed (m sec^{-1})	0.26	-0.62, 1.16	0.562	.006 / .009	-1.21	-3.35, 0.80	0.245
ACC mean temperature (°C)	0.08	-0.22, 0.39	0.601	.005 / .007	-0.98	-2.50, 0.41	0.178
ELA max windspeed (m sec^{-1})	0.11	-0.36, 0.57	0.628	.004 / .006	-1.04	-2.86, 0.73	0.245
Absolute pressure (kPa)	0.17	-0.60, 0.98	0.673	.003 / .005	-16.97	-96.06, 58.39	0.661
Mean total temperature (°C)	0.07	-0.28, 0.42	0.704	.003 / .004	-0.9	-2.49, 0.56	0.238
MID mean temperature (°C)	0.05	-0.26, 0.37	0.731	.002 / .003	-0.86	-2.36, 0.53	0.234
Mean total cloud cover (0 - 100)	0	-0.02, 0.03	0.739	.002 / .003	-0.96	-3.14, 0.93	0.343
HYSPLIT mean trajectories (degrees °)	0	-0.01, 0.01	0.769	.002 / .002	-0.96	-3.56, 1.19	0.404
MID max temperature (°C)	0.04	-0.24, 0.32	0.802	.001 / .002	-0.83	-2.52, 0.76	0.316
ACC max temperature (°C)	0.03	-0.23, 0.29	0.833	.001 / .001	-0.79	-2.45, 0.77	0.325
ELA total rain (mm)	0.02	-0.23, 0.24	0.838	.001 / .001	-0.65	-1.27, -0.07	0.031
ELA mean temperature (°C)	0.04	-0.38, 0.47	0.844	.001 / .001	-0.78	-2.46, 0.78	0.334
ELA max temperature (°C)	-0.02	-0.36, 0.31	0.889	.000 / .001	-0.52	-2.28, 1.19	0.55

Information Transfer Program Introduction

None.

USGS Summer Intern Program

None.

Student Support					
Category	**Section 104 Base Grant**	**Section 104 NCGP Award**	**NIWR-USGS Internship**	**Supplemental Awards**	**Total**
Undergraduate	3	0	0	0	3
Masters	5	0	0	0	5
Ph.D.	0	0	0	0	0
Post-Doc.	1	0	0	0	1
Total	9	0	0	0	9

Notable Awards and Achievements

The student involved in the project entitled Characterization of Groundwater Hydrology in Two Thermokarst Lake Systems was awarded the Farvolden Award for Outstanding Student Presentation at the National Ground Water Association Summit in Nashville, TN, December 4, 2017.